Nonlocal Willis Dynamic Homogenization Theory for Active Metabeams

Shaoyun Wang

Department of Mechanical and Aerospace Engineering, University of Missouri, Columbia, Missouri 65211, USA

Guoliang Huang*

Department of Mechanics and Engineering Science, College of Engineering, Peking University, Beijing 100871, PR China

Abstract

Unlike classical elasticity, Willis media exhibit coupling between stress–velocity and momentum–strain, capturing additional dynamic interactions in heterogeneous systems. While previous studies have predominantly focused on the homogenization of passive Willis media, extending these concepts to active systems remains largely unexplored. In this work, we employ an nonlocal Willis dynamic homogenization for active metabeams that integrates sensor–actuator pairs into a background beam to induce nonreciprocal coupling. By employing a source-driven homogenization approach, our EMT accurately captures the full dispersion curves over the entire Brillouin zone—overcoming the limitations of static or long-wavelength theories—and enables the definition of a winding number for the frequency spectrum under periodic boundary conditions (PBC). imaginary part, continuum media Notably, our framework predicts the emergence of low-frequency shear waves, absent in traditional beam theory, and facilitates direction-dependent wave amplification and attenuation. Through asymptotic analysis, we determine the frequency spectrum under open boundary conditions (OBC) and reveal its relationship to the periodic spectrum, with the resulting eigenmodes (skin modes) exhibiting pronounced edge localization that can be characterized by the generalized Brillouin zone (GBZ). Furthermore, we establish a bulk–boundary correspondence (BBC) that links the winding number to the localization direction of skin modes, providing a practical alternative to directly computing the GBZ. Finally, we demonstrate applications in nonreciprocal filtering, amplification, and interface-localized energy harvesting, paving the way for next-generation active mechanical metamaterials with tailored wave functionalities.

Keywords: Willis medium, dynamic homogenization, non-Hermiticity, nonlocality, nonreciprocity, topology

1. Introduction

Momentum, a conserved quantity proportional to the product of density and velocity, arises as a consequence of spatial homogeneity according to Noether's theorem (Landau et al., 1976; Goldstein et al., 2002). In contrast, the stress-strain relation—stating that stress is proportional to an elastic constant times strain—is an empirical law characterizing specific material behavior (Landau et al., 1986). Despite their differing physical origins, momentum–velocity and stress-strain pairs share a fundamental similarity: they both act as conjugate variables in the Lagrangian formalism. Classical elasticity treats them independently, but Willis media introduce cross-

*Corresponding author
Email address: guohuang@pku.edu.cn (Guoliang Huang)

couplings—termed Willis couplings—between momentum and strain, as well as stress and velocity, modifying conventional elastic behavior (Willis, 1981, 1997). These couplings necessitate new homogenization methods including Green's function methods and field averaging (Willis, 2009, 2011, 2012; Milton and Willis, 2010; Nemat-Nasser and Srivastava, 2011; Shuvalov et al., 2011; Norris et al., 2012; Srivastava, 2015; Nassar et al., 2015), asymptotic homogenization (Nassar et al., 2016), perturbative expansions combined with field averaging (Qu et al., 2022; Milton, 2007), and mode expansion with subspace projection (Ponge et al., 2017; Pernas-Salomón and Shmuel, 2018). Such approaches have extended Willis couplings to acoustics (Muhlestein et al., 2017; Li et al., 2022, 2024) and piezoelectricity (Pernas-Salomón and Shmuel, 2020b; Pernas-Salomón et al., 2021; Pernas-Salomón and Shmuel, 2020a; Lee et al., 2023; Baz, 2024; Muhafra et al., 2023). However, homogenization in active systems, where artificial couplings arise, remains challenging. Source-driven homogenization (Sieck et al., 2017) offers a systematic framework for incorporating background media and scatterers, making it a promising approach for studying active systems. This study extends source-driven homogenization to a non-Hermitian Willis metabeam with sensor-actuator elements, breaking major symmetry (Fig. 1). We develop an effective medium model that captures high-frequency and short-wavelength wave behavior, advancing both theoretical and practical understanding of active Willis materials.

Willis media, derived from homogenization theory, exhibit unique properties that drive advanced metamaterial design. In cloaking, transformed media extend beyond classical elasticity and align with the Milton–Briane–Willis gauge (Milton et al., 2006; Chen and Haberman, 2023). Willis coupling enables asymmetric reflection (Liu et al., 2019; Muhlestein et al., 2017) and precise control over polarization, mode conversion, wavefront shaping, and independent reflection/transmission tuning (Qu et al., 2022; Chen et al., 2020; Li et al., 2018). While most studies focus on passive Willis systems, integrating active elements, particularly sensor–actuator pairs, leads to novel effects like direction-dependent wave amplification (Cheng and Hu, 2022) and nonreciprocal wave propagation (Zhai et al., 2019). Despite these advances, key aspects such as non-Hermiticity, topology (bulk–boundary correspondence), symmetry properties, and space–time duality remain largely unexplored (Christensen et al., 2024; Yves et al., 2024; Ashida et al., 2020; Galiffi et al., 2022).

In classical elasticity, material properties remain constant (Landau et al., 1986), whereas metamaterials exhibit frequency-dependent properties, enabling effects like bandgaps (Huang et al., 2009) and negative refraction (Zhu et al., 2014). Willis media extend this by introducing both temporal nonlocality (frequency dispersion) and spatial nonlocality (spatial dispersion). While spatial dispersion is well-established in optics—leading to anisotropic propagation, gyrotropy, and directed energy flow (Agranovich and Ginzburg, 2013; Shokri and Rukhadze, 2019)—it is uncommon in elasticity. In structured elastic media, it couples material properties to both frequency and wavenumber, altering wave interactions. For free waves, effective properties follow dispersion relations, but external loads that depend on both parameters can excite waves with arbitrary frequencies and wavenumbers. This nonlocality is crucial for capturing high-frequency and short-wavelength behavior, essential for understanding spectral topology under PBCs and skin modes under OBCs. However, it also complicates boundary value problems by requiring nonlocal boundary conditions.

Non-Hermitian systems have advanced significantly since Carl Bender's discovery that PT-symmetric non-Hermitian operators can have entirely real eigenvalues (Bender and Boettcher, 1998), challenging the notion that Hermiticity is necessary for real spectra (Sakurai and Napolitano, 2017) and expanding research in non-Hermitian physics (Bender and Hook, 2024). Varying non-Hermitian couplings induces PT-symmetry breaking, leading to a phase transition from real to complex eigenvalues (Ashida et al., 2020). At the transition point (exceptional point), eigenvalues and eigenvectors coalesce, enabling novel effects such as enhanced sensor sensitivity and unconventional laser modes (Miri and Alu, 2019). Simultaneously, the study of topological insulators, rooted in bulk-boundary correspondence, faces challenges in non-Hermitian systems due to the breakdown of Bloch band theory. This leads to non-Bloch band theory and the discovery of the non-Hermitian skin effect (Yao and Wang, 2018), which establishes a new form of bulk-boundary correspondence linking the winding number of the complex frequency spectrum under PBC to skin modes under OBC (Okuma et al., 2020; Zhang et al., 2020). Many quantum non-Hermitian findings extend naturally to classical wave systems, including electromagnetic and acoustic waves, due to their shared mathematical framework—eigenvalue problems in the Hilbert space. Non-Hermitian skin modes appear in elastic systems (Chen et al., 2021), interface modes in metaplates (Wang et al., 2024), and bulk-boundary correspondence in discrete systems (Wu et al., 2024). However, a systematic exploration of the frequency spectrum under both PBC and OBC, particularly the role of the GBZ in governing skin modes and extending bulk-boundary correspondence to nonlocal non-Hermitian Willis systems, remains an open question.

Elastic beams with piezoelectric patches and integrated circuitry serve as a versatile platform for studying unconventional elastic waves. They enable observations of the non-Hermitian skin effect (Chen et al., 2021), odd mass density (Wu et al., 2023), temporal reflection (Wang et al., 2025), frequency conversion (Wu et al., 2022), and topological pumping (Xia et al., 2021). Beam models also advance Willis media research, from dynamic homogenization of inhomogeneous Euler–Bernoulli beams (Pernas-Salomón and Shmuel, 2018) to parameter retrieval in Timoshenko beams with multiple scatterers (Liu et al., 2019; Chen et al., 2020). However, developing a complete EMT for active Timoshenko beams with multiple scatterers remains an open challenge.

Motivated by the microstructure design in Chen et al. (2020), we introduce non-Hermiticity into a background beam by embedding sensor–actuator pairs that generate nonreciprocal coupling. Employing a source-driven homogenization method, we develop an effective medium theory for nonlocal non-Hermitian Willis metabeams. This theory accurately reproduces the full dispersion curves over the entire Brillouin zone—overcoming the limitations of static or long-wavelength homogenization approaches—and enables the definition of a winding number for the spectrum under PBC. Moreover, our framework predicts the emergence of a low-frequency shear wave, absent in traditional beam theory, and facilitates nonreciprocal wave amplification and attenuation. Through asymptotic analysis, we calculate the frequency spectrum under OBC and reveal its relationship to the spectrum under PBC. The resulting eigenmodes, or skin modes, under OBC exhibit pronounced edge localization, whose extent can be characterized by the GBZ derived from the asymptotic analysis. Furthermore, we establish a rigorous bulk–boundary correspondence for nonlocal non-Hermitian Willis media, elucidating the interplay between the winding number and skin modes; this correspondence allows one to determine the localization direction of the skin modes using the winding number rather than the computationally challenging GBZ. Finally, we demonstrate practical applications—including nonreciprocal filters and amplifiers and interface-localized energy harvesting—paving the way for the next generation of active mechanical metamaterials with tailored wave functionalities.

This paper is organized as follows. Section 2 presents the source-driven homogenization approach for nonlocal non-Hermitian Willis metabeams with embedded sensor-actuator elements. Section 3 validates the proposed EMT

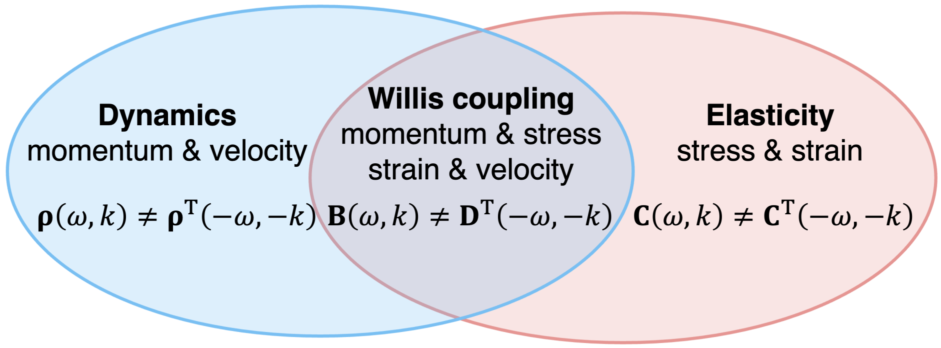

Figure 1: Possible constitutive operators in elastodynamics with broken major symmetry. The broken major symmetry of the elastic tensor $\mathbf{C}(\omega, k) \neq \mathbf{C}^T(-\omega, -k)$, density tensor $\boldsymbol{\rho}(\omega, k) \neq \boldsymbol{\rho}^T(-\omega, -k)$, and Willis coupling tensor $\mathbf{B}(\omega, k) \neq \mathbf{D}^T(-\omega, -k)$ leads to the non-Hermitian media.

by comparing theoretical dispersion predictions with COMSOL simulations across various parameter regimes. Section 4 analyzes key wave phenomena, including low-frequency shear waves, nonreciprocal wave amplification and attenuation, asymptotic analysis of the open-boundary spectrum, and bulk–boundary correspondence. Section 5 explores practical applications such as nonreciprocal filtering, amplification, and interface-localized energy harvesting. Finally, Section 6 summarizes the main findings and outlines future research directions. Additional derivations and supporting materials are provided in the Appendices.

2. Effective medium theory of nonlocal non-Hermitian Willis metabeam

In this section, we apply EMT to derive the effective constitutive relations for a metabeam embedded with sensor-actuators (Fig. 2(a)). The homogenization process is illustrated in Fig. 2(b), where sensors and actuators are modeled as embedded scatterers. We first introduce the Timoshenko beam equations (Section 2.1), forming the theoretical foundation. The background beam response under external sources (Fig. 2(b), top panel) is analyzed in Section 2.2, followed by the effective medium response (Fig. 2(b), bottom panel) in Section 2.3. The total response (Fig. 2(b), middle panel), comprising the microscale local response (Section 2.4) and mesoscale multiple scattering effects (Section 2.5), leads to the derivation of the effective constitutive relations (Section 2.6). Finally, we formulate the nonlocal governing equations and boundary value problem (BVP) in Section 2.7.

2.1. Fundamental Equations of the Timoshenko Beam

Consider a Timoshenko beam characterized by mass density ρ, Young's modulus E, and shear modulus G. The material's response is governed by the balance of linear momentum μ and angular momentum J (Yao et al., 2009; Chen et al., 2020)

$$\begin{aligned} \partial_t \mu &= \partial_x F + f, \\ \partial_t J &= \partial_x M + F + q, \end{aligned} \tag{1}$$

where F denotes the shear force, M represents the bending moment, and f and q correspond to the external body torque and transverse body force, respectively. The bending curvature κ, shear strain γ, rotational angle ψ, and

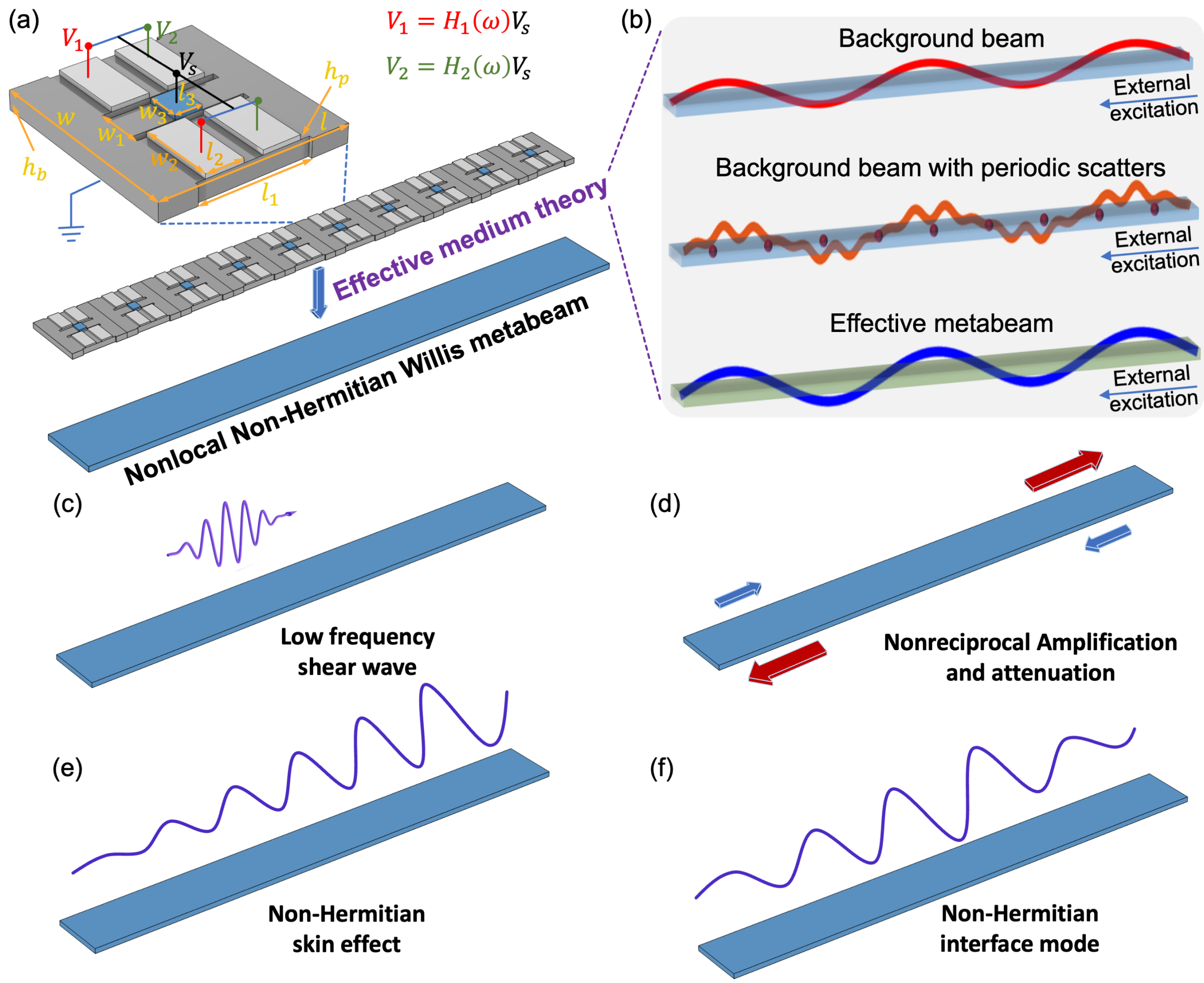

Figure 2: Schematic illustration of the EMT for a metabeam and its associated wave phenomena. (a) The unit cell of the metabeam, featuring a sensor (blue) and four actuators (light gray) in the top panel. The middle panel depicts a finite metabeam consisting of 10 unit cells, while the bottom panel presents its effective medium representation as a nonlocal non-Hermitian Willis metabeam. (b) A schematic diagram illustrating the wave responses in different configurations: the top panel shows the response of the background beam, the middle panel includes periodic scatterers embedded in the background beam, and the bottom panel represents the response of the homogenized effective beam, all under external excitation (blue arrow). (c–f) Demonstrations of various phenomena of the nonlocal non-Hermitian Willis metabeam: (c) low-frequency shear wave propagation, (d) nonreciprocal wave amplification and attenuation, (e) the non-Hermitian skin effect, and (f) the non-Hermitian interface mode.

transverse displacement w satisfy the following geometric relations (Yao et al., 2009; Chen et al., 2020)

$$\begin{aligned} \kappa &= \partial_x \psi + p \\ \gamma &= \partial_x w - \psi + s, \end{aligned} \tag{2}$$

where p and s represent the external curvature load and shear load, respectively. The general constitutive relation of the Timoshenko beam is given by (Yao et al., 2009; Chen et al., 2020)

$$\begin{bmatrix} \kappa \\ \gamma \\ \mu \\ J \end{bmatrix} = \begin{bmatrix} 1/D_0 & 0 & 0 & 0 \\ 0 & 1/G_0 & 0 & 0 \\ 0 & 0 & \rho_0 & 0 \\ 0 & 0 & 0 & I_0 \end{bmatrix} \begin{bmatrix} M \\ F \\ \partial_t w \\ \partial_t \psi \end{bmatrix}, \tag{3}$$

where D_0 is the bending stiffness, G_0 is the shear stiffness, I_0 is the moment of inertia, and ρ_0 is the line mass density. These parameters are defined as $D_0 = EI$, $G_0 = k_s AG$, $I_0 = \rho I$, and $\rho_0 = \rho A$, where A is the cross-sectional area, k_s is the Timoshenko shear coefficient (taken as 5/6), I is the second moment of area, and ρ is the material density.

Using Eqs. (1), (2), and (3), the governing equations can be written in matrix form for the state vector

$$\boldsymbol{\zeta}_1 \mathbf{u} = \mathbf{Q}, \tag{4}$$

where

$$\boldsymbol{\zeta}_1 = \begin{bmatrix} 1/D_0 & 0 & 0 & -\partial_x \\ 0 & 1/G_0 & -\partial_x & 1 \\ 0 & \partial_x & -\rho_0 \partial_t^2 & 0 \\ \partial_x & 1 & 0 & -I_0 \partial_t^2 \end{bmatrix}, \quad \mathbf{u} = \begin{bmatrix} M \\ F \\ w \\ \psi \end{bmatrix}, \quad \mathbf{Q} = \begin{bmatrix} p \\ s \\ f \\ q \end{bmatrix}. \tag{5}$$

Meanwhile, Eq. (4) in the frequency domain $e^{-i\omega t}$ is

$$\boldsymbol{\zeta}_2 \mathbf{u} = \mathbf{Q}, \tag{6}$$

and in frequency-wavenumber domain $e^{i(kx-\omega t)}$ is

$$\boldsymbol{\zeta} \mathbf{u} = \mathbf{Q}, \tag{7}$$

where

$$\boldsymbol{\zeta}_2 = \begin{bmatrix} 1/D_0 & 0 & 0 & -\partial_x \\ 0 & 1/G_0 & -\partial_x & 1 \\ 0 & \partial_x & \omega^2 \rho_0 & 0 \\ \partial_x & 1 & 0 & \omega^2 I_0 \end{bmatrix}, \quad \boldsymbol{\zeta} = \begin{bmatrix} 1/D_0 & 0 & 0 & -ik \\ 0 & 1/G_0 & -ik & 1 \\ 0 & ik & \omega^2 \rho_0 & 0 \\ ik & 1 & 0 & \omega^2 I_0 \end{bmatrix} \tag{8}$$

2.2. Response of the background beam under external sources

Under the external excitation $e^{i(kx-\omega t)}$ shown in the top panel of Fig. 2(b), the governing equations for the state vector of a homogeneous background beam with external sources in the frequency-wavenumber domain are given by (Chen et al., 2020)

$$\boldsymbol{\zeta} \mathbf{u}_{\text{ext}} = \mathbf{Q}_{\text{ext}}, \tag{9}$$

where the subscript ext denotes the fields in Eq. (7) under external excitation.

2.3. Response of the effective metabeam under external sources

For the background beam with periodic scatterers under external excitation, as shown in the middle panel of Fig. 2(b), the response consists of the intrinsic behavior of the background beam and multiple scattering effects induced by the periodic scatterers. In this setup, actuators generate a source vector, making the scatterers function similarly to external sources.

In the homogenization process, the source vector applied by the actuators is represented as an effective source vector $\mathbf{Q}_{\text{eff}}$. The governing equations for the state vector of the effective metabeam are then given by (Chen et al., 2020)

$$\boldsymbol{\zeta}\mathbf{u}_{\text{eff}} + \mathbf{Q}_{\text{eff}} = \mathbf{Q}_{\text{ext}}. \tag{10}$$

Here, $\mathbf{Q}_{\text{eff}}$ is an unknown vector dependent on the local response at the microscopic scale and the multiple scattering effects at the mesoscale, both of which are discussed in the following sections.

2.4. Local response at microscopic scale

The sensor-actuator elements detect the local state vector $\mathbf{u}_{\text{loc}}$ and apply the source vector $\mathbf{Q}_0$ to the beam. The geometry and material parameters are presented in Appendix A. In our design (Fig. 2(a)), the sensor detects only the bending curvature, while four actuators apply the bending moment and shear strain. However, this framework can be extended to systems capable of detecting the complete local state vector and applying the full source vector. In the frequency domain, the local source vector is related to the local state vector through the polarizability tensor, modulated by the transfer functions $H_1(\omega)$ and $H_2(\omega)$, as shown in Fig. 2(a) (Chen et al., 2020),

$$\mathbf{Q}_0 = \boldsymbol{\beta}(\omega)\mathbf{u}_{\text{loc}}. \tag{11}$$

The tensor $\boldsymbol{\beta}(\omega)$ is a frequency-dependent local polarizability tensor, with only β_{11} and β_{21} being nonzero in our design, as shown in Fig. 2(a). It is directly linked to the transfer functions implemented via analog or digital circuits but cannot be determined analytically. Instead, we obtain it using the retrieval method described in the Appendix E.

As shown in Fig. 2(a), the transfer function defines the relationship between the sensed voltage V_s from the sensing piezoelectric patch and the actuator voltages V_1 and V_2, given by

$$\begin{aligned} V_1 &= H_1(\omega)V_s, \\ V_2 &= H_2(\omega)V_s. \end{aligned} \tag{12}$$

Here, $V_s = \int_A D_z \, dA/C_0$, where A is the top surface area of the sensing piezoelectric patch, D_z is the z-component of the electric displacement vector, and C_0 is the capacitance, provided in Appendix A. An example of transfer function implementation is detailed in Chen et al. (2021).

In general, a transfer function is expressed as the ratio of two complex polynomials. For instance, the transfer functions $H_1(\omega)$ and $H_2(\omega)$ in this study can be written as

$$H_i(\omega) = \frac{\sum_{m=0}^{M} a_{m,i}\omega^m}{\sum_{n=0}^{N} b_{n,i}\omega^n}, \quad i = 1, 2, \tag{13}$$

where M and N are the highest-order indices, and $a_{m,i}$ and $b_{n,i}$ are the complex coefficients of the mth and nth order terms in the numerator and denominator polynomials of $H_i(\omega)$, respectively. The local polarizability tensor is not directly proportional to the transfer functions; however, its elements remain rational functions, as indicated by our observations and supported by the strong agreement between EMT predictions and COMSOL simulations. Consequently, the element in the ith row and jth column can be expressed as

$$\beta_{ij}(\omega) = \frac{\sum_{m=0}^{M} \tilde{a}_{m,ij}\omega^m}{\sum_{n=0}^{N} \tilde{b}_{n,ij}\omega^n}, \quad i, j = 1, 2, 3, 4, \tag{14}$$

where M and N denote the highest-order indices, and $\tilde{a}_{m,ij}$ and $\tilde{b}_{n,ij}$ are the complex coefficients of the mth and nth order terms in the numerator and denominator polynomials of $\beta_{ij}(\omega)$, respectively. By leveraging circuit-based control, each element can be modulated independently, allowing for the realization of an arbitrary local constitutive matrix that encompasses frequency-dependent responses, positive and negative values, real and imaginary components, and non-Hermitian configurations.

2.5. Multiple scattering at mesoscropic scale

Next, we analyze the multiple scattering effect in the middle panel of Fig. 2(b). Using Eq. (B.18), the state vector response at position x due to a point source $\mathbf{Q}(x') = \delta(x' - nL)\mathbf{Q}_n$ located at $x' = nL$ is given by

$$\mathbf{u}(x) = \mathbf{G}(\omega, x - nL)\mathbf{Q}_n. \tag{15}$$

where the Green's function in the frequency domain is defined in Eq. (B.16).

The system in this study is periodic, allowing Bloch's theorem to be applied to all fields, including the source vector $\mathbf{Q}_n$ (Sieck et al., 2017). Therefore, the source vector $\mathbf{Q}_n$ satisfies

$$\mathbf{Q}_n = e^{iknL}\mathbf{Q}_0. \tag{16}$$

Therefore, the total local field $\mathbf{u}_{\text{loc}}$ at $x = 0$, excited by all sources, is the superposition of the local fields generated by each individual internal source and the external field $\mathbf{u}_{\text{ext}}$

$$\mathbf{u}_{\text{loc}} = \mathbf{u}_{\text{ext}} + \sum_{n\in\mathbb{Z}} \mathbf{G}(\omega, 0 - nL)\mathbf{Q}_n = \mathbf{u}_{\text{ext}} + \mathbf{S}(\omega, k)\mathbf{Q}_0, \tag{17}$$

where the scattering matrix is defined as

$$\mathbf{S}(\omega, k) = \sum_{n\in\mathbb{Z}} \mathbf{G}(\omega, 0 - nL)e^{iknL}. \tag{18}$$

Here, the summation includes the current scatter at $n = 0$, unlike previous studies that exclude it to prevent divergence (Li et al., 2024). In our case, the Green's function remains finite at $n = 0$. Moreover, removing the effect of the current scatter violates the symmetry constraints in Eqs. (33–37) derived from macroscopic theory. By applying the symmetry condition of the Green's function in Eq. (C.6), we find that the scattering matrix $\mathbf{S}$ satisfies the following symmetry properties:

$$\begin{aligned}\mathbf{S}(\omega,k)&=\mathbf{S}^{\dagger}(\omega,k),\\ \mathbf{S}(\omega,k)&=\mathbf{S}^{T}(\omega,-k),\\ \mathbf{S}(\omega,k)&=\mathbf{S}^{*}(-\omega,-k).\end{aligned}\tag{19}$$

Applying Bloch's theorem to the source vector $\mathbf{Q}_n$ in Eq. (16), the scattering matrix becomes

$$\begin{aligned}\mathbf{S}(\omega,k)=&\sum_{n\in\mathbb{Z}}\left[\mathbf{R}_1(-nL)\mathbf{B}_1(-nL)^Te^{-i|nL|k_1}e^{iknL}+\mathbf{R}_2(-nL)\mathbf{B}_2(-nL)^Te^{-|nL|k_2}e^{iknL}\right]\\ =&\mathbf{R}_1(1)\mathbf{B}_1(1)^T\left(\sum_{n=-\infty}^{-1}e^{i(k_1+k)nL}+\frac{1}{2}\right)+\mathbf{R}_1(-1)\mathbf{B}_1(-1)^T\left(\sum_{n=1}^{\infty}e^{i(k-k_1)nL}+\frac{1}{2}\right)\\ &+\mathbf{R}_2(1)\mathbf{B}_2(1)^T\left(\sum_{n=-\infty}^{-1}e^{(k_2+ik)nL}+\frac{1}{2}\right)+\mathbf{R}_2(-1)\mathbf{B}_2(-1)^T\left(\sum_{n=1}^{\infty}e^{(ik-k_2)nL}+\frac{1}{2}\right)\\ =&\mathbf{R}_1(1)\mathbf{B}_1(1)^T\left(\frac{e^{-iL(k_1+k)}}{1-e^{-iL(k_1+k)}}+\frac{1}{2}\right)+\mathbf{R}_1(-1)\mathbf{B}_1(-1)^T\left(\frac{e^{iL(k-k_1)}}{1-e^{iL(k-k_1)}}+\frac{1}{2}\right)\\ &+\mathbf{R}_2(1)\mathbf{B}_2(1)^T\left(\frac{e^{-L(k_2+ik)}}{1-e^{-L(k_2+ik)}}+\frac{1}{2}\right)+\mathbf{R}_2(-1)\mathbf{B}_2(-1)^T\left(\frac{e^{L(ik-k_2)}}{1-e^{L(ik-k_2)}}+\frac{1}{2}\right).\end{aligned}\tag{20}$$

Here, $\mathbf{R}_1(x)$, $\mathbf{R}_2(x)$, $\mathbf{B}_1(x)$, and $\mathbf{B}_2(x)$ only depend on the sign of the spatial coordinate x. Therefore, their values at $x=1$ are used to represent them for positive x, while their values at $x=-1$ are used to represent them for negative x. In the final step, the geometric series is used

$$\sum_{n=1}^{\infty}y^n=\lim_{N\to\infty}\sum_{n=1}^{N}y^n=\lim_{N\to\infty}\frac{y-y^{N+1}}{1-y}.\tag{21}$$

The series converges only if the common ratio satisfies $|y|<1$. Strictly speaking, the magnitude of the common ratio is equal to 1, causing the series to diverge. In this study, we directly neglect the divergent term y^{N+1}. This approach can be justified by introducing small damping, allowing the wavenumber to have a small imaginary part such that the common ratio satisfies $|y|<1$ (Sieck et al., 2017; Shore and Yaghjian, 2007). Subsequently, the limit is taken as the damping approaches zero. This procedure is also validated a posteriori, as the dispersion relations obtained from the effective media closely match those from COMSOL simulation.

2.6. Effective constitutive relations

Next, we derive the effective constitutive relations. Eliminating the external excitation from Eqs. (9) and (10) gives

$$\boldsymbol{\zeta}\left(\mathbf{u}_{\text{eff}}-\mathbf{u}_{\text{ext}}\right)=-\mathbf{Q}_{\text{eff}}.\tag{22}$$

Additionally, eliminating the local state vector $\mathbf{u}_{\text{loc}}$ from Eq. (11) and (17) yields

$$\left(\mathbf{I}-\boldsymbol{\beta}\mathbf{S}\right)\mathbf{Q}_0=\boldsymbol{\beta}\mathbf{u}_{\text{ext}},\tag{23}$$

where $\mathbf{I}$ is the 4×4 identity matrix. Additionally, applying spatial averaging, the effective source vector $\mathbf{Q}_{\text{eff}}$ relates to the microscopic point source vector $\mathbf{Q}_0$ at $x = 0$ as (Sieck et al., 2017; Chen et al., 2020; Alù, 2011)

$$\mathbf{Q}_{\text{eff}} = \frac{1}{l}\int_{-l/2}^{l/2} \delta(x)\mathbf{Q}_0\, dx = \frac{\mathbf{Q}_0}{l}, \tag{24}$$

where l is the unit cell length. Using Eqs. (22)–(24), we derive the constitutive relation (detailed derivation in the Appendix D)

$$\mathbf{Q}_{\text{eff}} = \mathbf{K}\mathbf{u}_{\text{eff}}, \tag{25}$$

where

$$\mathbf{K} = \left[l\mathbf{I} - l\boldsymbol{\beta}\mathbf{S} - \boldsymbol{\beta}\boldsymbol{\zeta}^{-1}\right]^{-1}\boldsymbol{\beta}. \tag{26}$$

If $\boldsymbol{\beta}$ is nonsingular, Eq. (26) simplifies to

$$\mathbf{K} = \left[l\boldsymbol{\beta}^{-1} - L\mathbf{S} - \boldsymbol{\zeta}^{-1}\right]^{-1}. \tag{27}$$

when BD are nonzero In Section 2.4, we establish that the local polarizability matrix $\boldsymbol{\beta}$ can be an arbitrary frequency-dependent but wavenumber-independent matrix. Here, we constrain it to be a real symmetric matrix and an even function with respect to ω. Given $\boldsymbol{\zeta}$ in Eq. (8), $\mathbf{S}$ in Eq. (18), and $\boldsymbol{\beta}$ as a real even symmetric matrix, they satisfy the following symmetry conditions

$$\begin{aligned}
&\boldsymbol{\zeta}(\omega,k) = \boldsymbol{\zeta}^*(-\omega,-k), && \mathbf{S}(\omega,k) = \mathbf{S}^*(-\omega,-k), && \boldsymbol{\beta}(\omega,k) = \boldsymbol{\beta}^*(-\omega,-k),\\
&\boldsymbol{\zeta}(\omega,k) = \boldsymbol{\zeta}^\dagger(\omega,k), && \mathbf{S}(\omega,k) = \mathbf{S}^\dagger(\omega,k), && \boldsymbol{\beta}(\omega,k) = \boldsymbol{\beta}^\dagger(\omega,k),\\
&\boldsymbol{\zeta}(\omega,k) = \boldsymbol{\zeta}^T(\omega,-k), && \mathbf{S}(\omega,k) = \mathbf{S}^T(\omega,-k), && \boldsymbol{\beta}(\omega,k) = \boldsymbol{\beta}^T(\omega,-k).
\end{aligned} \tag{28}$$

Since matrix addition, subtraction, and inversion in Eq. (26) preserve these symmetries, the resulting matrix $\mathbf{K}$ also satisfies them.

Substituting Eq. (25) into Eq. (10) in the absence of an external source and comparing it with Eq. (3), we propose a general constitutive relation for Willis metabeams in matrix form

$$\begin{bmatrix} \kappa_{\text{eff}} \\ \gamma_{\text{eff}} \\ \mu_{\text{eff}} \\ J_{\text{eff}} \end{bmatrix} = \begin{bmatrix} 1/D_0 + K_{11} & K_{12} & K_{13}/(-i\omega) & K_{14}/(-i\omega) \\ K_{21} & 1/G_0 + K_{22} & K_{23}/(-i\omega) & K_{24}/(-i\omega) \\ K_{31}/(-i\omega) & K_{32}/(-i\omega) & \rho_0 + K_{33}/(-\omega^2) & K_{34}/(-\omega^2) \\ K_{41}/(-i\omega) & K_{42}/(-i\omega) & K_{43}/(-\omega^2) & I_0 + K_{44}/(-\omega^2) \end{bmatrix} \begin{bmatrix} M_{\text{eff}} \\ F_{\text{eff}} \\ v_{\text{eff}} \\ \varphi_{\text{eff}} \end{bmatrix}, \tag{29}$$

Here, v_{eff} and φ_{eff} represent the velocity and angular velocity, respectively, satisfying $v_{\text{eff}} = \dot{w}_{\text{eff}}$ and $\varphi_{\text{eff}} = \dot{\psi}_{\text{eff}}$ in the time domain, and $v_{\text{eff}} = -i\omega w_{\text{eff}}$ and $\varphi_{\text{eff}} = -i\omega\psi_{\text{eff}}$ in the frequency domain. Using these relations, we rewrite Eq. (29) as

$$\begin{bmatrix} \boldsymbol{\varepsilon} \\ \mathbf{p} \end{bmatrix} = \begin{bmatrix} \mathbf{C} & \mathbf{B} \\ \mathbf{D} & \boldsymbol{\rho} \end{bmatrix} \begin{bmatrix} \boldsymbol{\sigma} \\ \mathbf{v} \end{bmatrix} \tag{30}$$

where

$$\boldsymbol{\varepsilon}=\begin{bmatrix}\kappa_{\text{eff}}\\ \gamma_{\text{eff}}\end{bmatrix},\ \mathbf{p}=\begin{bmatrix}\mu_{\text{eff}}\\ J_{\text{eff}}\end{bmatrix},\ \boldsymbol{\sigma}=\begin{bmatrix}M_{\text{eff}}\\ F_{\text{eff}}\end{bmatrix},\ \mathbf{v}=\begin{bmatrix}v_{\text{eff}}\\ \varphi_{\text{eff}}\end{bmatrix}, \tag{31}$$

and

$$\begin{aligned}\mathbf{C}&=\begin{bmatrix}-1/D_0+K_{11} & K_{12}\\ K_{21} & 1/G_0+K_{22}\end{bmatrix}, &\quad \mathbf{B}&=\begin{bmatrix}K_{13}/(-i\omega) & K_{14}/(-i\omega)\\ K_{23}/(-i\omega) & K_{24}/(-i\omega)\end{bmatrix},\\ \mathbf{D}&=\begin{bmatrix}K_{31}/(-i\omega) & K_{32}/(-i\omega)\\ K_{33}/(-i\omega) & K_{34}/(-i\omega)\end{bmatrix}, &\quad \boldsymbol{\rho}&=\begin{bmatrix}\rho_0+K_{33}/(-\omega^2) & K_{34}/(-\omega^2)\\ K_{43}/(-\omega^2) & I_0+K_{44}/(-\omega^2)\end{bmatrix}.\end{aligned} \tag{32}$$

Equation (30) represents the effective constitutive relation in compliance form, where $\mathbf{B}$ and $\mathbf{D}$ are the Willis coupling matrices. The constitutive matrices satisfy the following conditions

$$\mathbf{C}(\omega,k)=\mathbf{C}^*(-\omega,-k),\qquad \begin{matrix}\mathbf{B}(\omega,k)=\mathbf{B}^*(-\omega,-k),\\ \mathbf{D}(\omega,k)=\mathbf{D}^*(-\omega,-k),\end{matrix}\qquad \boldsymbol{\rho}(\omega,k)=\boldsymbol{\rho}^*(-\omega,-k), \tag{33}$$

$$\mathbf{C}(\omega,k)=\mathbf{C}^\dagger(\omega,k),\quad \mathbf{B}(\omega,k)=-\mathbf{D}^\dagger(\omega,k),\quad \boldsymbol{\rho}(\omega,k)=\boldsymbol{\rho}^\dagger(\omega,k), \tag{34}$$

$$\mathbf{C}(\omega,k)=\mathbf{C}^T(\omega,-k),\quad \mathbf{B}(\omega,k)=\mathbf{D}^T(\omega,-k),\quad \boldsymbol{\rho}(\omega,k)=\boldsymbol{\rho}^T(\omega,-k), \tag{35}$$

Using Eq. (33) and Eq. (34), we obtain the following symmetry conditions

$$\mathbf{C}(\omega,k)=\mathbf{C}^T(-\omega,-k),\quad \mathbf{B}(\omega,k)=\mathbf{D}^T(-\omega,-k),\quad \boldsymbol{\rho}(\omega,k)=\boldsymbol{\rho}^T(-\omega,-k), \tag{36}$$

Furthermore, using Eq. (35) and Eq. (36), we obtain the following symmetry conditions

$$\mathbf{C}(\omega,k)=\mathbf{C}(-\omega,k),\quad \mathbf{B}(\omega,k)=\mathbf{B}(-\omega,k),\quad \mathbf{D}(\omega,k)=\mathbf{D}(-\omega,k),\quad \boldsymbol{\rho}(\omega,k)=\boldsymbol{\rho}(-\omega,k), \tag{37}$$

These five symmetry conditions are not independent; rather, Eq. (33), Eq. (36), and Eq. (37) serve as the fundamental ones in the macroscopic framework, while the remaining two follow from them. Eq. (33) arises from the requirement that all physical fields in classical physics be real-valued (Agranovich and Ginzburg, 2013; Shokri and Rukhadze, 2019). Eq. (36) represents the major symmetry of Willis materials, while Eq. (37) corresponds to time-reversal symmetry (Agranovich and Ginzburg, 2013; Shokri and Rukhadze, 2019; Altman and Suchy, 2011). Eq. (35) follows from the Maxwell-Betti reciprocity theorem, which itself derives from major symmetry and time-reversal symmetry (Agranovich and Ginzburg, 2013; Shokri and Rukhadze, 2019; Pernas-Salomón and Shmuel, 2020b).

Our sensor-actuator system can break these symmetry conditions, enabling the realization of unconventional symmetry-broken nonlocal Willis media. For instance, breaking time-reversal symmetry requires violating the corresponding symmetry of the polarizability tensor, i.e., $\boldsymbol{\beta}(\omega)\neq\boldsymbol{\beta}(-\omega)$, which can be achieved by implementing odd-frequency-dependent transfer functions. Breaking major symmetry or Maxwell-Betti reciprocity requires a non-Hermitian or asymmetric polarizability tensor. By tailoring the polarizability tensor at the microscopic level, EMT allows for the engineering of macroscopic media with arbitrary symmetry-breaking properties.

Here, material properties depend on both frequency and wavenumber, indicating that the Willis metabeam exhibits both frequency and spatial dispersion (Agranovich and Ginzburg, 2013). Frequency and wavenumber are treated as independent variables, as discussed in Appendix F. In the spacetime domain, these dependencies translate into nonlocal constitutive relations, which are expressed in convolution form (Agranovich and Ginzburg, 2013; Jackson, 2012; Pernas-Salomón and Shmuel, 2020a).

$$\begin{bmatrix} \boldsymbol{\varepsilon}(t,x) \\ \mathbf{p}(t,x) \end{bmatrix} = \int_{-\infty}^{t}\int_{-\infty}^{\infty} \begin{bmatrix} \mathbf{C}(t,t';x,x') & \mathbf{B}(t,t';x,x') \\ \mathbf{D}(t,t';x,x') & \boldsymbol{\rho}(t,t';x,x') \end{bmatrix} \begin{bmatrix} \boldsymbol{\sigma}(t',x') \\ \mathbf{v}(t',x') \end{bmatrix} dt'dx' \tag{38}$$

If the medium's properties remain constant over time (time-independent), translational symmetry in the time domain is preserved, making the constitutive matrix dependent only on the time difference $t-t'$ (Agranovich and Ginzburg, 2013). Similarly, if the medium is spatially uniform, all points are equivalent, and the constitutive matrix depends only on the spatial difference $x-x'$ (Agranovich and Ginzburg, 2013). Under these conditions, we obtain

$$\begin{bmatrix} \boldsymbol{\varepsilon}(t,x) \\ \mathbf{p}(t,x) \end{bmatrix} = \int_{-\infty}^{t}\int_{-\infty}^{\infty} \begin{bmatrix} \mathbf{C}(t-t',x-x') & \mathbf{B}(t-t',x-x') \\ \mathbf{D}(t-t',x-x') & \boldsymbol{\rho}(t-t',x-x') \end{bmatrix} \begin{bmatrix} \boldsymbol{\sigma}(t',x') \\ \mathbf{v}(t',x') \end{bmatrix} dt'dx' \tag{39}$$

The quantity $\boldsymbol{\Psi}$, representing $\boldsymbol{\varepsilon}$, $\mathbf{p}$, $\mathbf{C}$, $\mathbf{B}$, $\mathbf{D}$, $\boldsymbol{\rho}$, $\boldsymbol{\sigma}$, and $\mathbf{v}$, is related in real space and reciprocal space through the Fourier transform

$$\boldsymbol{\Psi}(t,x) = \frac{1}{2\pi}\int_{-\infty}^{\infty}\int_{-\infty}^{\infty} \boldsymbol{\Psi}(\omega,k)e^{i(kx-\omega t)}\,dxdt \tag{40}$$

and its inverse transform,

$$\boldsymbol{\Psi}(\omega,k) = \frac{1}{2\pi}\int_{-\infty}^{\infty}\int_{-\infty}^{\infty} \boldsymbol{\Psi}(t,x)e^{-i(kx-\omega t)}\,dkd\omega. \tag{41}$$

Since all wave fields in classical physics are real-valued in real space, the Fourier transform satisfies

$$\boldsymbol{\Psi}(\omega,k) = \boldsymbol{\Psi}^{*}(-\omega,-k). \tag{42}$$

This symmetry condition, imposed by physical constraints at the macroscopic scale, aligns with the microscopic symmetries of the constitutive matrix in Eq. (33).

2.7. Governing equations and boundary value problem

In this section, we discuss the governing equations and the BVP. For the effective nonlocal non-Hermitian Willis metabeam, the effective state vector remains governed by Eq. (1) and Eq. (2). Utilizing the constitutive relation in Eq. (39), the governing equation for the state vector in the space-time domain is expressed as

$$\begin{bmatrix} 0 & -\partial_x \\ -\partial_x & 1 \end{bmatrix} \boldsymbol{\sigma}(t,x) + \int_{-\infty}^{t}\int_{\infty}^{\infty} \mathbf{C}(t-t',x-x')\boldsymbol{\sigma}(t',x') + \mathbf{B}(t-t',x-x')\partial_t \mathbf{w}(t',x')dt'dx' = \mathbf{q_1} \tag{43}$$

$$\begin{bmatrix} 0 & \partial_x \\ \partial_x & 1 \end{bmatrix} \mathbf{w}(t,x) + \partial_t\int_{-\infty}^{t}\int_{\infty}^{\infty} \mathbf{D}(t-t',x-x')\boldsymbol{\sigma}(t',x') + \boldsymbol{\rho}(t-t',x-x')\partial_t \mathbf{w}(t',x')dt'dx' = \mathbf{q_2} \tag{44}$$

where $\mathbf{w} = [w, \psi]^T$, $\mathbf{q}_1 = [p_{\text{ext}}, s_{\text{ext}}]^T$, and $\mathbf{q}_2 = [f_{\text{ext}}, q_{\text{ext}}]^T$. In the frequency-wavenumber domain, the governing equations take the form

$$\mathbf{H}\mathbf{u}_{\text{eff}} = \mathbf{Q}_{\text{ext}}, \tag{45}$$

where

$$\mathbf{H} = \begin{bmatrix} 0 & 0 & 0 & -ik \\ 0 & 0 & -ik & 1 \\ 0 & ik & 0 & 0 \\ ik & 1 & 0 & 0 \end{bmatrix} + \begin{bmatrix} \mathbf{C} & -i\omega\mathbf{B} \\ -i\omega\mathbf{D} & -\omega^2\boldsymbol{\rho} \end{bmatrix}. \tag{46}$$

In the absence of an external source, the dispersion relations are obtained by setting the determinant of the coefficient matrix to zero

$$\det(\mathbf{H}) = 0. \tag{47}$$

For each ω and k satisfying the dispersion relations, the corresponding solution $\mathbf{u}_{\text{eff}}$ in Eq. (45) represents the eigenvector.

For the vibration problem, boundary conditions are required to determine the eigenfrequencies and eigenmodes of the metabeam. Based on the boundary conditions of the conventional Timoshenko beam, the most relevant boundary conditions for the nonlocal non-Hermitian Willis metabeam are listed below

$$\begin{aligned} &\text{Fixed :} && w_{\text{eff}} = 0, \quad \psi_{\text{eff}} = 0 \\ &\text{Simply supported :} && w_{\text{eff}} = 0, \quad M_{\text{eff}} = 0 \\ &\text{Free :} && M_{\text{eff}} = 0, \quad F_{\text{eff}} = 0 \end{aligned} \tag{48}$$

In our formalism of Willis media, the bending moment, shear force, displacement, and rotational angle are integrated into a state vector, allowing them to be directly prescribed as boundary conditions. This approach eliminates the challenges of the conventional Willis media framework, which involves second-order derivatives. In the traditional formulation, the nonlocal constitutive relations in Eq. (25) express the bending moment and shear force in terms of displacement and rotational angle, making their boundary conditions nonlocal. As a result, solving nonlocal boundary conditions analytically becomes intractable, requiring advanced numerical methods (Rabczuk et al., 2023).

3. Validation of the effective medium theory

In this section, we validate the EMT by comparing its predicted dispersion relations with those from unit cell analysis using COMSOL simulations across various transfer functions, including symmetric real, antisymmetric real, asymmetric real, frequency-dependent real, and antisymmetric imaginary cases. By accounting for spatial dispersion effects, the nonlocal EMT accurately captures wave behavior, including nonreciprocal propagation, attenuation, and amplification, even in high-frequency and short-wavelength regimes—where conventional homogenization theories often fail.

In our study, the sensing piezoelectric patch detects only the bending curvature, while the actuating piezoelectric patch applies only the bending moment and shear strain. Consequently, only β_{11} and β_{21} are nonzero in the local

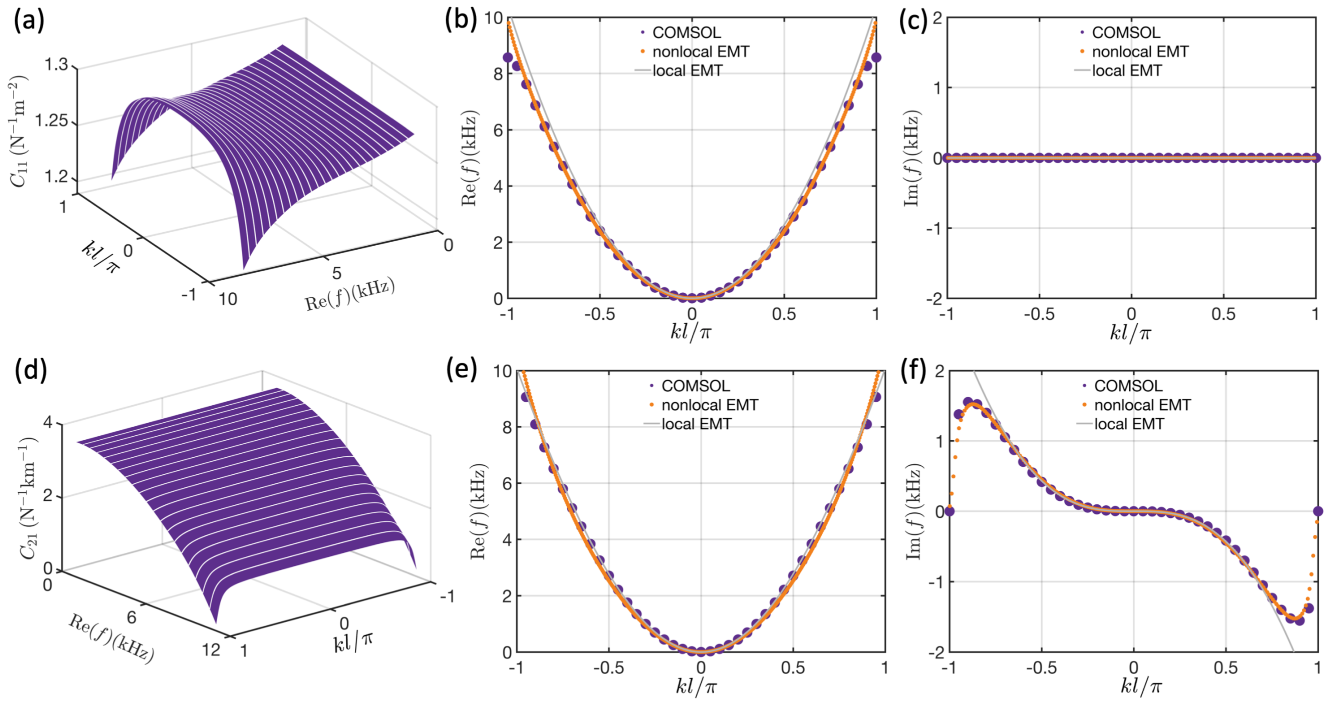

Figure 3: Effective material properties and dispersion relations for symmetric and antisymmetric real transfer functions. (a–c) Symmetric transfer functions: (a) Real part of C_{11} as a function of frequency and wavenumber. (b) Real part of the dispersion curves from unit cell analysis in COMSOL simulations (purple dots), nonlocal EMT (orange dots), and local EMT (gray solid line). (c) Imaginary part of the dispersion curves from COMSOL unit cell analysis (purple dots), nonlocal EMT (orange dots), and local EMT (gray solid line). (d–f) Antisymmetric transfer functions: (d) Real part of C_{21} as a function of frequency and wavenumber. (e) Real part of the dispersion curves from COMSOL unit cell analysis (purple dots), nonlocal EMT (orange dots), and local EMT (gray solid line). (f) Imaginary part of the dispersion curves from COMSOL unit cell analysis (purple dots), nonlocal EMT (orange dots), and local EMT (gray solid line).

polarizability tensor. Under this condition, Eq. (26) simplifies to

$$\begin{aligned} C_{11} &= \frac{1}{D_0} + K_{11} \\ C_{21} &= K_{21}, \end{aligned} \tag{49}$$

where

$$\begin{aligned} K_{11} &= \frac{\beta_{11}\left(b_4 k^4 + b_2 k^2 + b_0\right)}{a_4 k^4 + a_2 k^2 + a_1 k + a_0} \\ K_{21} &= \frac{\beta_{21}\left(b_4 k^4 + b_2 k^2 + b_0\right)}{a_4 k^4 + a_2 k^2 + a_1 k + a_0}, \end{aligned} \tag{50}$$

and

$$\begin{aligned} b_4 &= -D_0 \beta_{11} g_0 \\ b_2 &= \omega^2 \left(D_0 \rho_0 + I_0 g_0\right) \\ b_0 &= \rho_0 \omega^2 \left(-I_0 \omega^2 + g_0\right) \\ a_4 &= D_0 l g_0 \left(-1 + S_{12}\beta_{21} + S_{11}\beta_{11}\right) \\ a_2 &= -\omega^2 \left(-D_0 l \rho_0 - I_0 l g_0 + D_0 l S_{12}\beta_{21}\rho_0 + I_0 l S_{12}\beta_{21} g_0 + D_0 l S_{11}\beta_{11}\rho_0 + D_0 I_0 \beta_{11} g_0 + I_0 l S_{11}\beta_{11} g_0\right) \\ a_1 &= -D_0 \beta_{21} g_0 \omega^2 \rho_0 i \\ a_0 &= -\omega^2 \rho_0 \left(-I_0 \omega^2 + g_0\right)\left(-l + l S_{12}\beta_{21} + D_0 \beta_{11} + l S_{11}\beta_{11}\right). \end{aligned} \tag{51}$$

As $\omega \to 0$, we also have $k \to 0$, reducing Eq. (50) to

$$\begin{aligned} C_{11} &= \frac{1}{D_0} + \frac{\beta_{11}}{l - D_0\beta_{11}} \\ C_{21} &= \frac{\beta_{21}}{l - D_0\beta_{11}}, \end{aligned} \tag{52}$$

Here, the material properties become wavenumber-independent, reducing the medium to a local EMT, accurately matching the dispersion relations in the low-frequency and long-wavelength regime. Additionally, β_{11} influences both C_{11} and C_{21} simultaneously. For small β_{11}, the leading-order term is given by

$$\begin{aligned} C_{11} &= \frac{1}{D_0} + \frac{\beta_{11}}{l} \\ C_{21} &= \frac{\beta_{21}}{l}. \end{aligned} \tag{53}$$

In this case, β_{11} and β_{21} independently contribute to C_{11} and C_{21}, respectively.

In Eq. (50), K_{11} and K_{21} are proportional to β_{11} and β_{21}, respectively, each scaled by a rational function. For a symmetric transfer function where $H_1(\omega) = H_2(\omega)$, the actuators generate only bending moments, making β_{11} the only nonzero component. Consequently, K_{11} is nonzero, modifying the effective bending stiffness in Eq. (30). For an antisymmetric transfer function where $H_1(\omega) = -H_2(\omega)$, the actuators generate only shear strain, resulting in β_{21} as the only nonzero component. In this case, K_{21} becomes nonzero, leading to the formation of effective shear stiffness in Eq. (30). For an asymmetric transfer function, where $H_1(\omega) \neq H_2(\omega)$ and $H_1(\omega) \neq -H_2(\omega)$, both K_{11} and K_{21} are generated simultaneously. Additionally, in our study, the imaginary part of the rational function is significantly smaller than the real part. As a result, when the transfer functions $H_1(\omega)$ and $H_2(\omega)$ are purely real, K_{11} and K_{21}

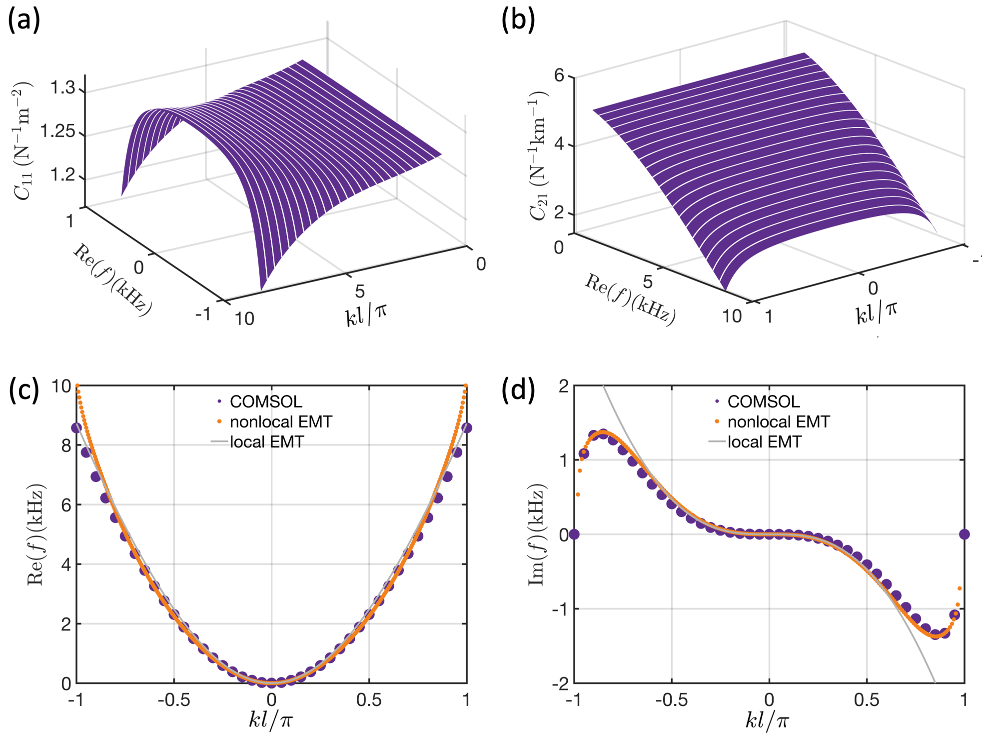

Figure 4: Effective material properties and dispersion relations for asymmetric real transfer functions. (a) Real part of C_{11} as a function of frequency and wavenumber. (b) Real part of C_{21} as a function of frequency and wavenumber. (c) Real part of the dispersion curves from unit cell analysis in COMSOL simulations (purple dots), nonlocal EMT (orange dots), and local EMT (gray solid line). (d) Imaginary part of the dispersion curves from COMSOL unit cell analysis (purple dots), nonlocal EMT (orange dots), and local EMT (gray solid line).

are nearly real. Similarly, when the transfer functions are purely imaginary, K_{11} and K_{21} are nearly imaginary. For complex transfer functions, K_{11} and K_{21} are generally complex-valued.

Next, we examine the effective properties and dispersion relations for different transfer functions. For symmetric transfer functions with $H_1(\omega) = H_2(\omega) = 0.05$, Fig. 3(a) presents the real part of C_{11}, while the imaginary part is omitted as it is negligibly small. The dispersion curves from COMSOL simulations, the nonlocal effective C_{11} from Eq. (49), and the local effective C_{11} from Eq. (52) are shown in Fig. 3(b,c). The dispersion curves from the local EMT align well with COMSOL simulations in the low-frequency and long-wavelength regimes but deviate at high frequencies and short wavelengths. In contrast, the nonlocal EMT provides a close match to the COMSOL results across both low- and high-frequency ranges, demonstrating its superior accuracy in capturing wave dynamics over a broader frequency and wavelength spectrum compared to the local EMT.

For antisymmetric transfer functions with $H_1(\omega) = -H_2(\omega) = 0.3$, the effective properties and dispersion curves are shown in Fig. 3(d–f). Only the real part of C_{21} is displayed, as the imaginary part remains small and is therefore omitted. The presence of a nonzero real C_{21} introduces an imaginary component in the dispersion curves. The local EMT accurately captures both the real and imaginary parts of the dispersion relations in the low-frequency and long-wavelength regimes, while the nonlocal EMT extends this accuracy to high frequencies and short wavelengths. The emergence of C_{21} breaks the major symmetry, rendering the medium non-Hermitian and introducing a nonzero imaginary component in the dispersion relation. Furthermore, the imaginary part of the dispersion relation is antisymmetric with respect to the wavenumber, leading to wave attenuation for left-propagating waves (nega-

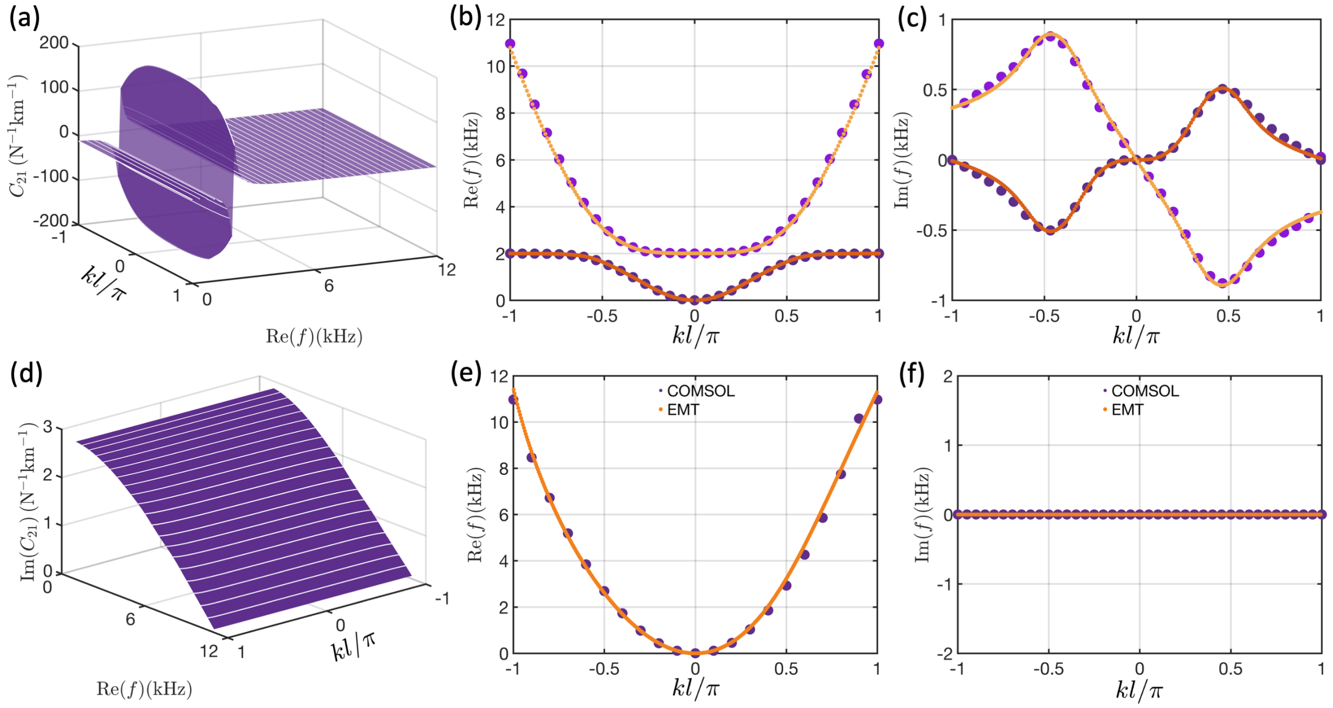

Figure 5: Effective material properties and dispersion relations for local resonant and antisymmetric imaginary transfer functions. (a–c) Local resonant transfer functions: (a) Real part of C_{11} as a function of frequency and wavenumber. (b) Real part of the dispersion curves from COMSOL unit cell analysis (dark purple dots for the lower band, light purple dots for the upper band) and from EMT (dark orange dots for the lower band, light orange dots for the upper band). (c) Imaginary part of the dispersion curves from COMSOL unit cell analysis (dark purple dots for the lower band, light purple dots for the upper band) and EMT (dark orange dots for the lower band, light orange dots for the upper band). (d–f) Antisymmetric imaginary transfer functions: (d) Real part of C_{21} as a function of frequency and wavenumber. (e) Real part of the dispersion curves from COMSOL unit cell analysis (purple dots) and EMT (orange dots). (f) Imaginary part of the dispersion curves from COMSOL unit cell analysis (purple dots) and EMT (orange dots).

tive wavenumber) and amplification for right-propagating waves (positive wavenumber). This asymmetry induces nonreciprocal wave propagation due to non-Hermiticity.

For asymmetric transfer functions with $H_1(\omega) = 0.35$ and $H_2(\omega) = -0.25$, which incorporate the effects of both symmetric and antisymmetric transfer functions, the effective properties and dispersion curves are shown in Fig. 4. In this case, both C_{11} and C_{21} are nonzero, resulting in a downward shift in the real part of the dispersion curve and the appearance of an imaginary component in the dispersion relation. The local EMT accurately captures the dispersion curves in the low-frequency and long-wavelength regimes but shows deviations at high frequencies and short wavelengths. In contrast, the nonlocal EMT closely matches the COMSOL simulation results across both regimes, demonstrating its effectiveness in capturing wave dynamics over a broader frequency and wavelength range.

Our EMT extends beyond constant transfer functions and applies to frequency-dependent transfer functions, including the local resonant transfer function discussed here. We consider antisymmetric transfer functions given by

$$H_1(\omega) = -H_2(\omega) = \frac{0.3\omega_0^2}{\omega^2 - \omega_0^2} \tag{54}$$

where $\omega_0 = 4000\pi$ Hz. In this case, $H_1(\omega)$ is negative for $\omega < \omega_0$, positive for $\omega > \omega_0$, and singular at $\omega = \omega_0$. The antisymmetric transfer function induces a nonzero C_{21}, breaking Hermiticity and resulting in nonzero imaginary dispersion curves. The presence of local resonance splits the dispersion curve into two branches, with the imaginary dispersion curves exhibiting frequency sign reversal due to the sign change of C_{21} at ω_0. The nonlocal EMT closely matches the COMSOL simulation results for both real and imaginary dispersion curves across high-frequency and short-wavelength regimes, as shown in Fig. 5(a-c), demonstrating its effectiveness in capturing wave dynamics for frequency-dependent transfer functions over a broad frequency and wavelength range.

Non-Hermiticity alone does not necessarily lead to a complex spectrum. For instance, eigenvalues remain real in the PT-unbroken phase and can also be real in a more general pseudo-Hermitian system (Ashida et al., 2020). In our system, verifying the pseudo-Hermitian condition is challenging, yet we observe a real spectrum for antisymmetric imaginary transfer functions. For transfer functions $H_1(\omega) = -H_2(\omega) = 0.3i$, Fig. 5(d) presents the imaginary part of C_{21}, while the real part is omitted as it is negligibly small. The nonzero C_{21} breaks the Hermitian condition, yet the spectra in Fig. 5(e,f) remain purely real. However, the real part of the dispersion curve is asymmetric with respect to the vertical axis, as the nonzero C_{21} breaks parity symmetry. The agreement between the dispersion curves from COMSOL simulations and EMT in Fig. 5(e) confirms this asymmetry, demonstrating the validity of EMT for purely imaginary transfer functions.

4. Wave phenomena in non-Hermitian Willis beam

4.1. Dispersion curves and mode characterization of flexural waves

Flexural wave characterization+Physical mechanism In our study, only K_{21} and K_{11} are nonzero. Thus, the dispersion equations in Eq. (45) simplify to

$$\begin{pmatrix} C_{11} & 0 & 0 & -k\,i \\ C_{21} & 1/G_0 & -k\,i & 1 \\ 0 & k\,i & \omega^2\rho_0 & 0 \\ k\,i & 0 & 0 & J_0\,\omega^2 \end{pmatrix} \begin{pmatrix} M_{\text{eff}} \\ F_{\text{eff}} \\ w_{\text{eff}} \\ \psi_{\text{eff}} \end{pmatrix} = \begin{pmatrix} 0 \\ 0 \\ 0 \\ 0 \end{pmatrix} \tag{55}$$

where C_{11} and C_{21} are defined in Eq. (49). Eliminate M_{eff} and F_{eff} gives

$$\begin{bmatrix} -C_{11}\left(-\omega^2\rho_0 + G_0k^2\right) & -G_0k(C_{11}i - C_{21}k) \\ C_{11}G_0ki & -C_{11}G_0 + C_{11}J_0\omega^2 - C_{21}G_0ki - k^2 \end{bmatrix} \begin{bmatrix} w_{\text{eff}} \\ \psi_{\text{eff}} \end{bmatrix} = \begin{bmatrix} 0 \\ 0 \end{bmatrix} \tag{56}$$

Assuming w_{eff} as 1, we have

$$\psi_{\text{eff}} = -\frac{C_{11}G_0ki}{C_{11}G_0 - C_{11}J_0\omega^2 + C_{21}G_0ki + k^2} \tag{57}$$

The ratio of shear strain and rotation angle is defined as

$$\frac{\gamma_{\text{eff}}}{\psi_{\text{eff}}} = \frac{ikw_{\text{eff}} - \psi_{\text{eff}}}{\psi_{\text{eff}}} = -\frac{(C_{11}i - C_{21}k)(-C_{11}\omega^2\rho_0 + 2C_{11}G_0k^2 + C_{21}G_0k^3i)}{C_{11}(-\omega^2\rho_0 + G_0k^2)(C_{11} + C_{21}ki)i} \tag{58}$$

As shown in Fig. 6, the magnitude of the ratio of shear strain to rotation angle increases significantly compared to the traditional Timoshenko beam model, making the shear effect observable when C_{21} is nonzero for the antisymmetric transfer functions $H_1 = -H_2 = -1$. This indicates that the Willis metabeam in our study can support shear waves at low frequencies, a feature absent in classical beam models.

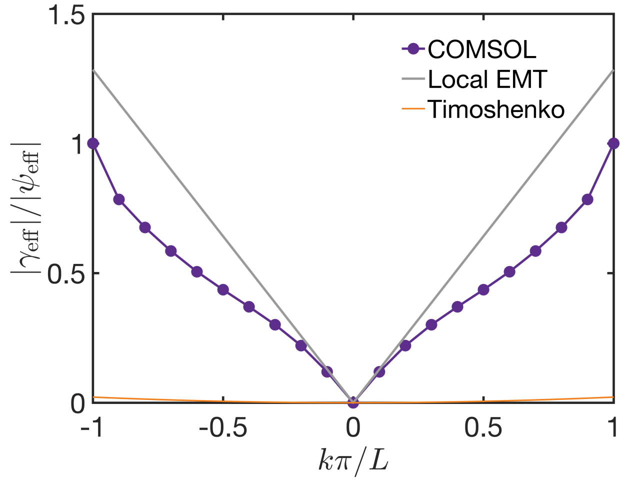

Figure 6: The magnitude of the ratio of shear strain to rotation angle from COMSOL simulations (purple solid line with circles), local EMT (gray solid line), and the traditional Timoshenko beam model (orange solid line). Here, antisymmetric transfer functions $H_1 = -H_2 = 1$ are used.

4.2. The broken reciprocity theorem

In local media, the reciprocity theorem is equivalent to major symmetry (Nassar et al., 2020). However, in nonlocal media, major symmetry alone does not ensure reciprocity. Instead, reciprocity arises from the combined presence of major symmetry and time-reversal symmetry (Shokri and Rukhadze, 2019). In our system, the presence of C_{21} breaks major symmetry, leading to reciprocity violation. Next, we examine reciprocity and its breaking, starting with the Green's function. The Green's function of Willis metabeam in the frequency-wavenumber domain satisfies

$$\mathbf{H}\mathbf{G}_{\mathrm{eff}}(\omega, k) = \mathbf{I}. \tag{59}$$

The presence of C_{21} breaks the symmetry condition of $\mathbf{H}$.

$$\mathbf{H}(\omega, k) \neq \mathbf{H}^T(\omega, -k), \tag{60}$$

Therefore, the Green's function $\mathbf{G}_{\mathrm{eff}} = \mathbf{H}^{-1}$ no longer satisfies the symmetry condition

$$\mathbf{G}_{\mathrm{eff}}(\omega, k) \neq \mathbf{G}_{\mathrm{eff}}^T(\omega, -k), \tag{61}$$

which translates to

$$\mathbf{G}_{\mathrm{eff}}(\omega, x - x') \neq \mathbf{G}_{\mathrm{eff}}^T(\omega, x' - x) \tag{62}$$

in the spatial domain. For an external load $\mathbf{Q}_{\mathrm{ext}}$, the corresponding response is given by

$$\mathbf{u}_{\mathrm{eff}}(\omega, x) = \int_L \mathbf{G}_{\mathrm{eff}}(\omega, x - x')\mathbf{Q}_{\mathrm{ext}}(x')dx' \tag{63}$$

in the spatial domain. To evaluate the reciprocity condition, we conduct two load-response tests. In the first case, the applied load is $\mathbf{Q}^1_{\mathrm{ext}}(\omega, x)$ with the corresponding response $\mathbf{u}^1_{\mathrm{eff}}(\omega, x)$, while in the second case, the load is $\mathbf{Q}^2_{\mathrm{ext}}(\omega, x)$

with the response $\mathbf{u}_{\text{eff}}^2(\omega, x)$. The reciprocity condition is given by (Nassar et al., 2020)

$$\int_L (\mathbf{u}_{\text{eff}}^2)^T(\omega, x)\mathbf{Q}_{\text{ext}}^1(\omega, x)dx = \int_L (\mathbf{u}_{\text{eff}}^1)^T(\omega, x)\mathbf{Q}_{\text{ext}}^2(\omega, x)dx. \tag{64}$$

Using Eq. (62), the reciprocity condition can be rewritten as

$$\int_L \int_L (\mathbf{Q}_{\text{ext}}^2)^T(\omega, x')\mathbf{G}_{\text{eff}}^T(\omega, x - x')\mathbf{Q}_{\text{ext}}^1(\omega, x)\, dxdx' = \int_L \int_L (\mathbf{Q}_{\text{ext}}^1)^T(\omega, x')\mathbf{G}_{\text{eff}}^T(\omega, x - x')\mathbf{Q}_{\text{ext}}^2(\omega, x)\, dxdx'. \tag{65}$$

Taking the transpose and interchanging x and x' on the right-hand side, we obtain

$$\int_L \int_L (\mathbf{Q}_{\text{ext}}^2)^T(\omega, x')\mathbf{G}_{\text{eff}}^T(\omega, x - x')\mathbf{Q}_{\text{ext}}^1(\omega, x)\, dxdx' = \int_L \int_L (\mathbf{Q}_{\text{ext}}^2)^T(\omega, x')\mathbf{G}_{\text{eff}}(\omega, x' - x)\mathbf{Q}_{\text{ext}}^1(\omega, x)\, dxdx'. \tag{66}$$

Therefore, Eq. (66) shows that the reciprocity condition in Eq. (64) is equivalent to the symmetry condition of the Green's function,

$$\mathbf{G}_{\text{eff}}(\omega, x - x') = \mathbf{G}_{\text{eff}}^T(\omega, x' - x). \tag{67}$$

In our study, the presence of C_{21} breaks this symmetry condition, leading to the inequality in Eq. (62). As a result, the equality in Eq. (66) is violated, thereby breaking the reciprocity theorem in Eq. (64).

We now numerically verify the breaking of the reciprocity theorem using COMSOL simulations with constant antisymmetric transfer functions $H_1(\omega) = -H_2(\omega) = 0.3$. Two numerical tests are performed: in the first case, a unit shear force $\mathbf{Q}_{\text{ext}}^1(x) = [0, 0, 0, 1]^T\delta(x + 6l)$ is applied at $x = -6l$, and the resulting displacement w_1 is measured at $x = 6l$, as shown in Fig. 7(a). In the second case, a unit shear force $\mathbf{Q}_{\text{ext}}^2(x) = [0, 0, 0, 1]^T\delta(x - 6l)$ is applied at $x = 6l$, and the displacement w_2 is measured at $x = -6l$, as illustrated in Fig. 7(a). The difference between the left-hand side and right-hand side of Eq. (64) is given by

$$\Delta = (\mathbf{u}_{\text{eff}}^2)^T\mathbf{Q}_{\text{ext}}^1 - (\mathbf{u}_{\text{eff}}^1)^T\mathbf{Q}_{\text{ext}}^2 = w_2 - w_1. \tag{68}$$

The measured magnitude of Δ, normalized by $|w_2|$, as a function of frequency is shown in Fig. 7(b). Since $|\Delta|/|w_1|$ is nonzero, Δ does not vanish, confirming the violation of the reciprocity theorem.

For a shear load applied on the left, the wave in the metabeam undergoes attenuation. This attenuation can be characterized using the k-ω dispersion relations. By sweeping ω from 1 kHz to 10 kHz, the corresponding k values are obtained by solving Eq. (47). The resulting dispersion curves are shown in Fig. 7(c) (3D view), Fig. 7(d) (front view), and Fig. 7(e) (top view). As an example, at an excitation frequency of 4 kHz, the imaginary parts of both wavenumbers are positive, indicating wave attenuation in the metabeam, as shown in the top panel of Fig. 7(a). Furthermore, in Fig. 7(f), the imaginary wavenumber matches the decay factor observed in the logarithmic plot of the transverse displacement magnitude, confirming the attenuation behavior.

4.3. Bulk-boundary correspondence

In Hermitian systems, the governing operator is Hermitian, ensuring real eigenvalues. In classical elasticity, for example, the governing equation can be expressed as an eigenvalue problem in Hilbert space, where the Hermitian

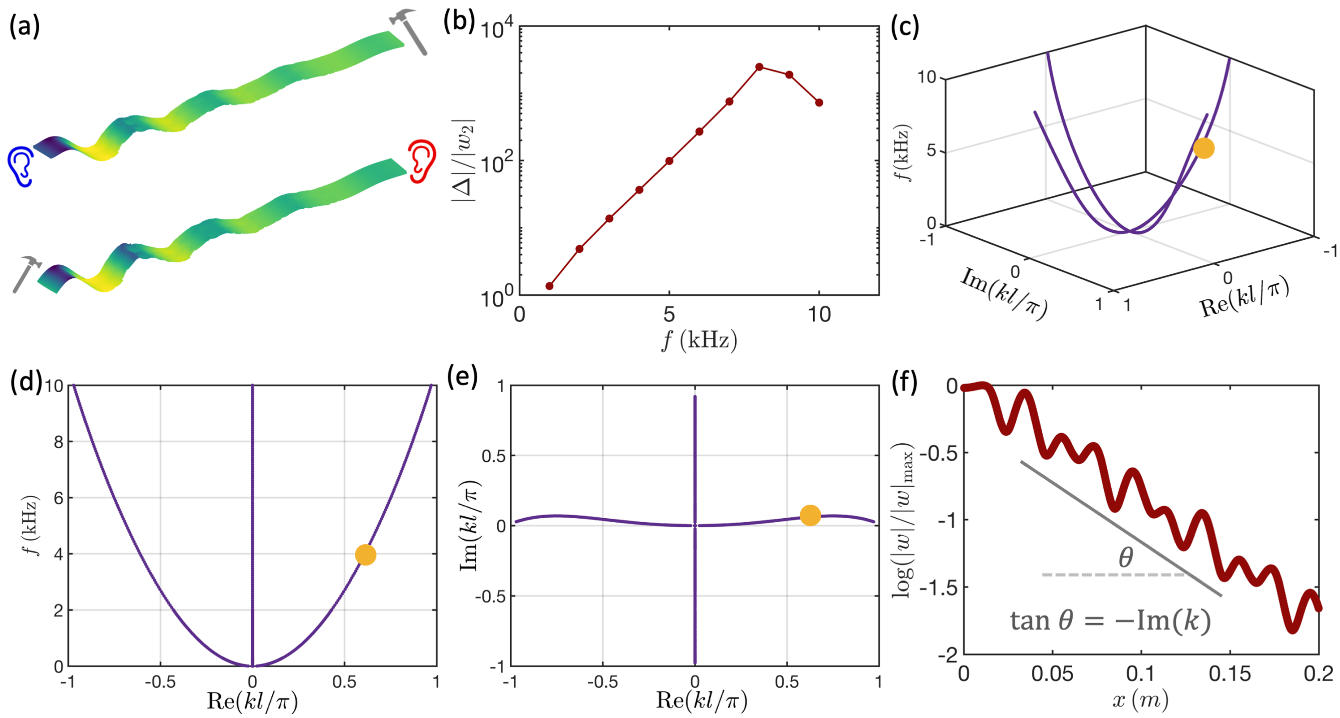

Figure 7: Nonreciprocal wave propagation in Willis media. (a) Displacement response under two shear force loads applied at the right (top panel) and left (bottom panel) with an excitation frequency of 4 kHz. The corresponding displacements are measured at the opposite ends. (b) Normalized displacement difference as a function of excitation frequency. (c) 3D view of the k-ω dispersion curves, where the orange point corresponds to the excitation frequency of 4 kHz in the bottom panel of (a). (d) Front view of the k-ω dispersion curves. (e) Top view of the k-ω dispersion curves. (f) Displacement field extracted along the middle line of the bottom panel in (a), with the slope of the gray solid line corresponding to the imaginary part of the orange point in (e).

nature of the operator guarantees real frequency spectrum. However, in non-Hermitian systems, this condition no longer holds, allowing complex frequency spectrum to emerge.

Despite the presence of non-Hermiticity, Bloch's theorem remains valid for systems that maintain linearity and periodicity. Consequently, the dispersion relation is still well-defined, and non-Hermitian systems exhibit frequency periodicity in both the real and imaginary axis within the first Brillouin zone. As a result, the frequency spectrum under PBC forms closed loops in the complex plane, each characterized by a topological invariant known as the winding number, which arises from differential geometry.

Under OBC, non-Hermitian systems exhibit the "skin effect", where most eigenmodes localize near the boundaries, forming "skin modes" (Yao and Wang, 2018). Studies (Okuma et al., 2020; Yang et al., 2020) show that the existence and localization direction of these modes are governed by the winding number: a nonzero winding number indicates the presence of skin modes, while its sign determines their localization direction. This relationship establishes a new form of bulk-boundary correspondence unique to non-Hermitian physics.

In the following section, we outline the method for calculating the winding number of the frequency spectrum under PBC, conduct an asymptotic analysis to derive the frequency spectrum under OBC, and extend the non-Hermitian bulk-boundary correspondence to Willis media.

4.3.1. Winding number of the frequency spectrum under PBC

In our system, multiple eigenfrequencies, denoted as $\omega_\alpha(k)$, may exist for a given wavenumber under PBC. In non-Hermitian systems, the frequency spectrum is generally complex and can form a loop enclosing a base point ω_b.

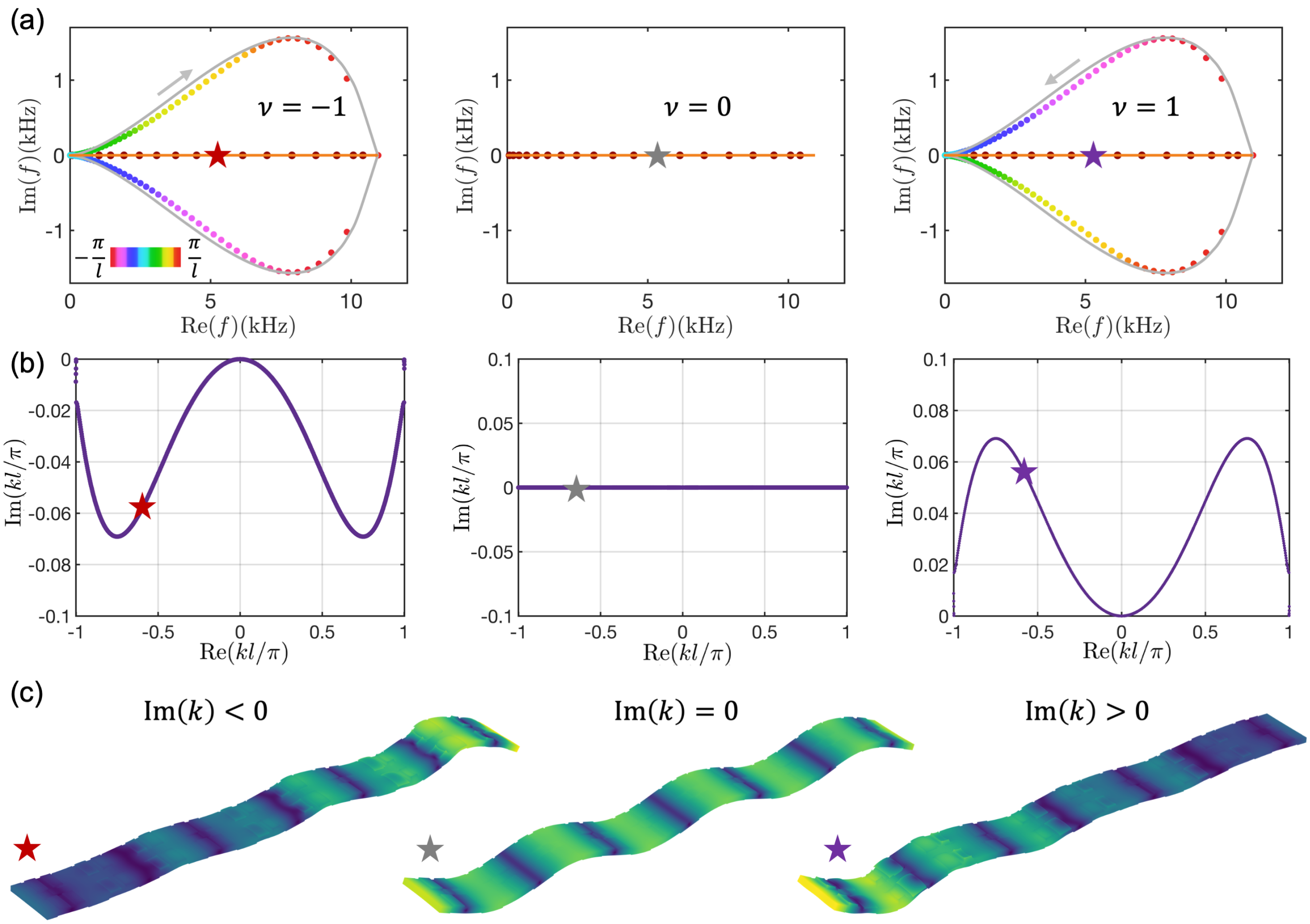

Figure 8: Bulk-boundary correspondence of the winding number and skin mode. (a) Frequency spectrum for the flexural mode of a metabeam under PBC (gradient-colored dots) and fixed boundary conditions (red dots) from COMSOL simulations. The gray solid loop, obtained from the dispersion relation in Eq. (47), and the orange solid line, derived from the BVP in Eq. (78), represent the effective non-Hermitian Willis medium. (b) GBZ associated with the frequency spectrum under fixed boundary conditions, represented by the orange solid line in (a). (c) Eigenmodes from COMSOL simulations corresponding to the starred locations in the frequency spectrum and their associated GBZs. In (a–c), the transfer functions are $H_1 = -H_2 = 0.3$ in the left panel, $H_1 = -H_2 = 0$ in the middle panel, and $H_1 = -H_2 = -0.3$ in the right panel.

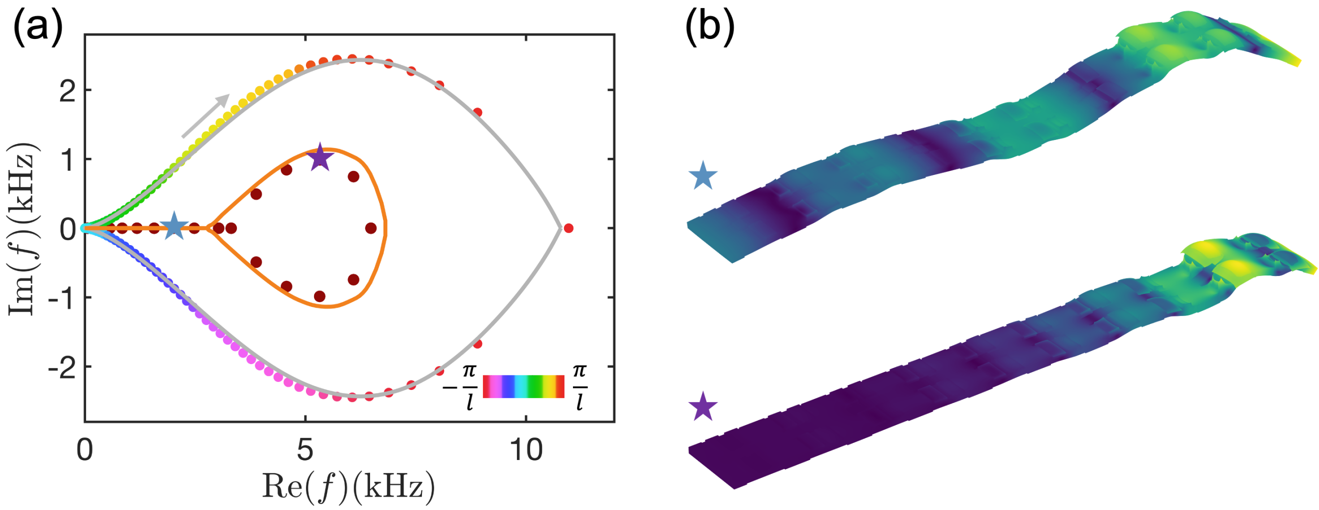

Figure 9: Bulk-boundary correspondence of the winding number and skin mode for transfer functions $H_1(\omega) = -H_2(\omega) = 1$. (a) Frequency spectrum for the flexural mode of a metabeam under PBC (gradient-colored dots) and fixed boundary conditions (red dots) from COMSOL simulations. The gray solid loop, obtained from the dispersion relation in Eq. (47), and the orange solid line, derived from the BVP in Eq. (78), represent the effective non-Hermitian Willis medium. (b) Eigenmodes from COMSOL simulations corresponding to the starred locations in the frequency spectrum (a).

This loop remains topologically protected as long as ω_b remains inside it. In one-dimensional systems, such loops are quantitatively characterized by the winding number of the spectrum (Ashida et al., 2020), given by

$$\nu(\omega_b) = \sum_{\alpha} \int_{-\pi/l}^{\pi/l} \frac{\mathrm{d}k}{2\pi} \frac{d}{dk} \arg\left[\omega_\alpha(k) - \omega_b\right]. \tag{69}$$

For antisymmetric transfer functions $H_1(\omega) = -H_2(\omega)$, the complex frequency spectrum under PBC is shown in Fig. 8(a) for $H_1(\omega) = 0.3$ (left panel), $H_1(\omega) = 0$ (middle panel), and $H_1(\omega) = -0.3$ (right panel). In the left panel, the spectral loop rotates clockwise as k varies from $-\pi/l$ to π/l, yielding a winding number $\nu(\omega_b) = -1$ for any base frequency ω_b enclosed by the loop. In the middle panel, the frequency spectrum collapses to a line, indicating a winding number of zero for any ω_b. In the right panel, the spectral loop rotates counterclockwise as k varies from $-\pi/l$ to π/l, resulting in a winding number $\nu(\omega_b) = 1$ for any base frequency ω_b inside the loop.

For antisymmetric transfer functions $H_1(\omega) = -H_2(\omega) = 1$, the complex frequency spectrum under PBC is shown in Fig. 9(a). The spectrum forms a clockwise loop, indicating a winding number $\nu(\omega_b) = -1$ for any base frequency ω_b enclosed by the loop. When the antisymmetric transfer function follows Eq. (54), the complex frequency spectrum under PBC is shown in Fig. 10(a). In this case, the spectrum consists of a counterclockwise loop on the left and a clockwise loop on the right. Consequently, the winding number $\nu(\omega_b)$ is 1 for any base frequency ω_b inside the left loop and -1 for any base frequency inside the right loop.

4.3.2. Asymptotic analysis of the frequency spectrum under OBC

Next, we address the BVP for a finite beam with specified boundary conditions. While non-Hermiticity often introduces significant complexity, an intriguing simplification emerges when the beam becomes very long: in this limit, the BVP effectively becomes independent of the specific boundary conditions. That is, for $L \to \infty$, certain non-Hermitian complexities are mitigated compared to the Hermitian case. In this section, we apply asymptotic analysis to determine the frequency spectrum under OBC by taking the beam's length L to infinity. This approach

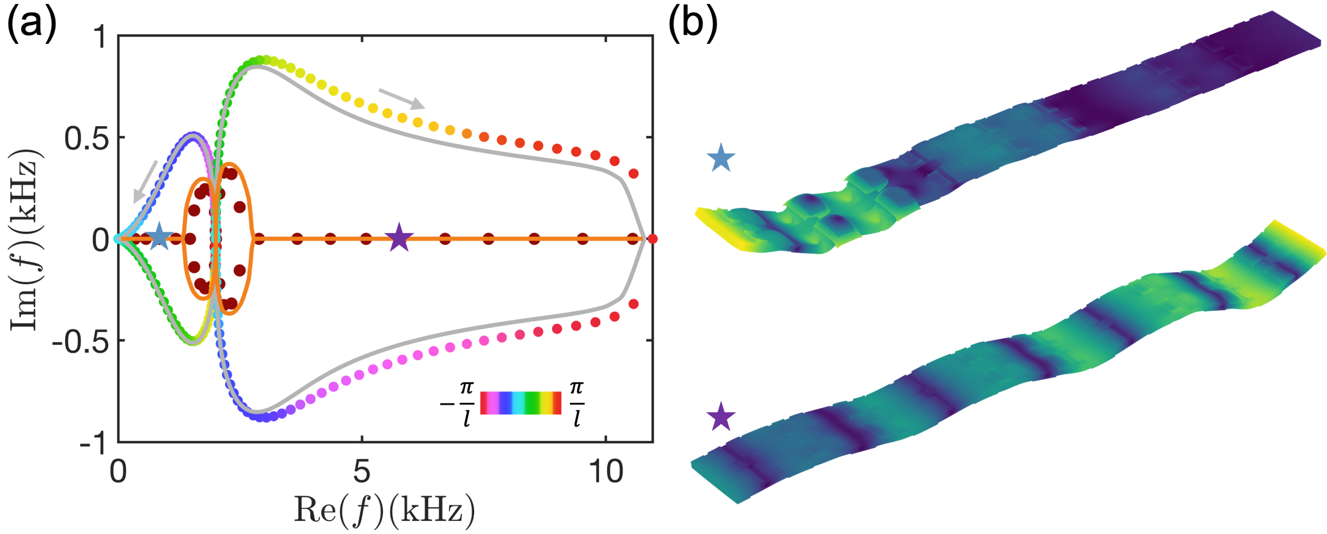

Figure 10: Frequency-dependent skin mode and its bulk-boundary correspondence for transfer functions in Eq. (54). (a) Frequency spectrum for the flexural mode of a metabeam under PBC (gradient-colored dots) and fixed boundary conditions (red dots) from COMSOL simulations. The gray solid loop, obtained from the dispersion relation in Eq. (47), and the orange solid line, derived from the BVP in Eq. (78), represent the effective non-Hermitian Willis medium. (b) Eigenmodes from COMSOL simulations corresponding to the starred locations in the frequency spectrum in (a).

yields two algebraic equations whose solutions not only provide the OBC frequency spectrum but also identify the GBZ—a concept unique to non-Hermitian systems. All derivations in this section are based on EMT, so the subscript eff is omitted for clarity.

For the non-Hermitian medium, the dispersion relation in Eq. (47) yields four wavenumber roots for a given frequency, denoted as k_n for $n = 1, 2, 3, 4$. The general solution for the transverse displacement of the non-Hermitian Willis metabeam is given by

$$w(x) = \sum_{n=1}^{4} A_n e^{ik_n x} \tag{70}$$

where A_n are the corresponding coefficients. The rotational angle is expressed as

$$\psi(x) = \sum_{n=1}^{4} A_n R_\psi^n e^{ik_n x} \tag{71}$$

where R_ψ^n is defined in Eq. (B.13). Now, we consider the BVP using fixed boundary conditions as an example:

$$w(0) = 0, \quad \psi(0) = 0, \quad w(L) = 0, \quad \psi(L) = 0. \tag{72}$$

where L is the length of the finite metabeam. Substituting the wave solutions into these boundary conditions, we obtain the following equations

$$\begin{pmatrix} 1 & 1 & 1 & 1 \\ R_\psi^1 & R_\psi^2 & R_\psi^3 & R_\psi^4 \\ e^{ik_1 L} & e^{ik_2 L} & e^{ik_3 L} & e^{ik_4 L} \\ R_\psi^1 e^{ik_1 L} & R_\psi^2 e^{ik_2 L} & R_\psi^3 e^{ik_3 L} & R_\psi^4 e^{ik_4 L} \end{pmatrix} \begin{pmatrix} A_1 \\ A_2 \\ A_3 \\ A_4 \end{pmatrix} = \begin{pmatrix} 0 \\ 0 \\ 0 \\ 0 \end{pmatrix} \tag{73}$$

Setting the determinant of the coefficient matrix to zero yields the frequency spectrum under fixed boundary conditions

$$\begin{vmatrix} 1 & 1 & 1 & 1 \\ R_\psi^1 & R_\psi^2 & R_\psi^3 & R_\psi^4 \\ e^{ik_1L} & e^{ik_2L} & e^{ik_3L} & e^{ik_4L} \\ R_\psi^1 e^{ik_1L} & R_\psi^2 e^{ik_2L} & R_\psi^3 e^{ik_3L} & R_\psi^4 e^{ik_4L} \end{vmatrix} = 0 \tag{74}$$

Next, we derive the GBZ by extending the method developed for lattice systems (Yokomizo and Murakami, 2019). The solution of Eq. (74) simplifies for large L, forming the corresponding continuum spectrum. Expanding the determinant in Eq. (74), we obtain

$$\begin{aligned} &F_1\left(\vec{k},\omega\right)e^{i(k_1+k_2)L} + F_2\left(\vec{k},\omega\right)e^{i(k_1+k_3)L} + F_3\left(\vec{k},\omega\right)e^{i(k_1+k_4)L} \\ &+ F_4\left(\vec{k},\omega\right)e^{i(k_2+k_3)L} + F_5\left(\vec{k},\omega\right)e^{i(k_2+k_4)L} + F_6\left(\vec{k},\omega\right)e^{i(k_3+k_4)L} = 0 \end{aligned} \tag{75}$$

Here, $\vec{k} = [k_1, k_2, k_3, k_4]$, and $F_i(\vec{k},\omega)$ $(i = 1, 2, \ldots, 6)$ are coefficients that depend on both frequency and wavenumbers, obtained by expanding the determinant in Eq. (74). We now analyze the asymptotic behavior of the solutions of Eq. (75) for large L, where the wavenumbers are ordered as $\text{Im}(k_1) < \text{Im}(k_2) < \text{Im}(k_3) < \text{Im}(k_4)$ for convenience.

If $\text{Im}(k_2) \neq \text{Im}(k_3)$, only one leading term proportional to $F_6(\vec{k},\omega)e^{i(k_3+k_4)L}$ remains in Eq. (75) in the limit of large L. This leads to

$$F_6\left(\vec{k},\omega\right) = 0 \tag{76}$$

which does not depend on L and does not allow for a continuous frequency spectrum.

On the other hand, when $\text{Im}(k_2) = \text{Im}(k_3)$, two leading terms proportional to $e^{i(k_2+k_4)L}$ and $e^{i(k_3+k_4)L}$ remain, allowing Eq. (75) to be rewritten as

$$e^{i(k_2-k_3)L} = -\frac{F_6\left(\vec{k},\omega\right)}{F_5\left(\vec{k},\omega\right)} \tag{77}$$

In such a case, we can expect that the difference between $\text{Re}\,(k_2)$ and $\text{Re}\,(k_3)$ can be changed almost continuously for a large L, producing continuum frequency spectrum.

Finally, in the asymptotic limit $L \to \infty$, the boundary value problem of the nonlocal non-Hermitian metabeam reduces to two algebraic equations:

$$\begin{aligned} |\mathbf{H}(\omega,k)| &= 0, \\ \text{Im}\,(k_2(\omega)) &= \text{Im}\,(k_3(\omega))\,. \end{aligned} \tag{78}$$

For a given complex frequency ω, the first equation in Eq. (78) yields four frequency-dependent wavenumbers $k_1(\omega)$, $k_2(\omega)$, $k_3(\omega)$, and $k_4(\omega)$, ordered as $\text{Im}(k_1) < \text{Im}(k_2) < \text{Im}(k_3) < \text{Im}(k_4)$. Among these, the second and third wavenumbers satisfy the second equation in Eq. (78). The first equation is complex and can be decomposed into two real equations, yielding a total of three real equations involving four independent real variables: $\text{Re}(\omega)$, $\text{Im}(\omega)$, $\text{Re}(k)$, and $\text{Im}(k)$. As a result, the solutions $(\text{Re}(\omega), \text{Im}(\omega), \text{Re}(k), \text{Im}(k))$ form continuous curves in the four-dimensional space. When projected onto the complex ω-plane, these solutions appear as continuous curves, ensuring that the frequency spectrum remains continuous. Similarly, their projection onto the complex k-plane forms continuous curves, known as the GBZ. The GBZ extends the Brillouin zone concept from Hermitian physics and plays a fundamental role in non-Hermitian physics. It is crucial for reconstructing the bulk-boundary correspondence of the Chern number and topological edge modes, as well as for computing the Green's function to determine system responses, such as stress or strain, under external excitations in engineering applications.

As mentioned earlier, Eq. (78) includes a complex equation. Unlike in non-Hermitian local media, where dispersion relations can be transformed into polynomial equations and efficiently solved using resultant-based methods from algebraic geometry, the dispersion relations here are transcendental. Consequently, the resultant-based method fails, necessitating direct numerical solutions. However, solving complex equations numerically is challenging since many numerical methods are designed for real-valued equations. To address this, for a given variable such as $\mathrm{Re}(\omega)$, Eq. (78) can be reformulated as three real equations involving three real independent unknowns. Numerical techniques such as Newton's method, iterative solvers, or gradient-based optimization can then be applied. Here, we use "fsolve" function in MATLAB. By sweeping $\mathrm{Re}(\omega)$ over the desired range, continuous frequency spectra and generalized Brillouin zones can be obtained.

In deriving Eq. (78), fixed boundary conditions were used. However, in the asymptotic limit, the frequency spectrum equation in Eq. (78) remains independent of the specific boundary conditions. For other boundary conditions, such as free, simply supported, or mixed conditions, the coefficients $F_i(\vec{k}, \omega)$ $(i = 1, 2, \ldots, 6)$ will change, but the spectrum condition $\mathrm{Im}\,(k_2(\omega)) = \mathrm{Im}\,(k_3(\omega))$ remains unaffected. Therefore, the frequency spectrum can be determined by solving Eq. (75) regardless of the boundary conditions. In other words, the frequency spectrum under OBC is independent of the specific type of boundary conditions.

The frequency spectra under OBC for various transfer functions are shown as orange solid lines in Fig. 8(a), Fig. 9(a), and Fig. 10(a), closely matching the eigenfrequencies obtained from COMSOL simulations (red dots). Minor discrepancies arise due to the finite beam length in the COMSOL model and diminish as the beam length increases. The corresponding eigenmodes, shown in Fig. 8(c), Fig. 9(b), and Fig. 10(b), exhibit localization at the edges and are therefore identified as skin modes. These skin modes display exponential localization, with exponential factors determined by the GBZ. For instance, the GBZ corresponding to the frequency spectrum in Fig. 8(a) is shown in Fig. 8(b). In the left panel of Fig. 8(b), the GBZ is below the horizontal axis, indicating positive exponential factors, leading to eigenmodes that grow from left to right, as seen in the left panel of Fig. 8(c). In the middle panel of Fig. 8(b), the GBZ lies on the horizontal axis, signifying zero exponential factors, corresponding to extended eigenmodes, as shown in the middle panel of Fig. 8(c). In the right panel of Fig. 8(b), the GBZ is above the horizontal axis, indicating negative exponential factors, resulting in eigenmodes that grow from right to left, as depicted in the right panel of Fig. 8(c).

4.3.3. Bulk-boundary correspondence

In the previous sections, we introduced the methods for calculating the winding number and the frequency spectrum under OBC, along with the concept of skin modes. In this section, we unify these concepts through bulk-boundary correspondence.

Bulk-boundary correspondence has two key aspects. The first concerns the relationship between the frequency spectra under PBC and OBC, which holds for both EMT and COMSOL simulations. In non-Hermitian systems, the OBC spectrum is always enclosed by the PBC spectrum. As shown in Fig. 8(a), for small transfer functions, the OBC spectrum remains real and is encircled by the PBC spectrum. As the transfer function magnitude increases, the OBC spectrum becomes complex while still remaining enclosed by the PBC spectrum, as seen in Fig. 9(a). For resonant transfer functions in Fig. 10(a), the PBC spectrum splits into two separate loops, each enclosing the OBC spectrum. These cases illustrate the fundamental relationship between the PBC and OBC spectra, reinforcing the principles of bulk-boundary correspondence in non-Hermitian systems.

The second aspect of bulk-boundary correspondence describes the relationship between the sign of the winding number at a base frequency (the eigenfrequency of an eigenmode under OBC) and the localization direction of skin modes. If the winding number at a base frequency is negative, the corresponding skin mode localizes at the right edge, as shown in the left panels of Fig. 8(a,c). If the winding number is zero, the eigenmode remains extended, as depicted in the middle panels of Fig. 8(a,c). Conversely, if the winding number is positive, the skin mode localizes at the left edge, as shown in the right panels of Fig. 8(a,c). These relationships hold for different transfer functions, as further demonstrated in Fig. 9 and Fig. 10. Instead of computing the GBZ, which is complex and computationally demanding, bulk-boundary correspondence provides a more efficient way to determine the localization of skin modes. By simply checking the sign of the winding number from the PBC spectrum, the localization behavior of skin modes can be directly inferred.

5. Application

5.1. Nonreciprocal filtering and amplification

In conventional designs, filters and amplifiers are treated as separate components that cannot be directly integrated. However, as shown in the previous section, our system exhibits direction-dependent gain: waves traveling from left to right are amplified, while those traveling from right to left are attenuated. This nonreciprocal property, enabled by Willis media, allows filtering and amplification to be seamlessly integrated into a single metabeam.

Specifically, for constant antisymmetric transfer functions $H_1(\omega) = -H_2(\omega) = 0.3$, the dispersion curves in Fig. 11(c–e) show that waves always decay from left to right but are amplified from right to left. As a result, when a signal enters from the left, the measured output on the right is attenuated, whereas a signal entering from the right is amplified on the left. By simply switching the input and detection positions, the metabeam can function either as a filter or an amplifier. The frequency responses for these two cases are compared in Fig. 11(a), clearly showing that the right output is attenuated for a left-side input, while the left output is amplified for a right-side input.

While conventional frequency-selective filters attenuate signals within a specific passband while leaving out-of-band signals largely unchanged, many applications require the additional capability to amplify out-of-band signals. Our Willis metabeam achieves this dual functionality by utilizing antisymmetric local resonant transfer functions (see Eq. (54)). Specifically, a left-to-right traveling wave is amplified for frequencies below 2 kHz but attenuated above 2 kHz, functioning as a low-stop high-amplifying filter (LSHAF). By reversing the input and output positions, the system instead operates as a low-amplifying high-stop filter (LAHSF), amplifying low-frequency components while attenuating higher frequencies. Numerical results for these two modes, shown in Fig. 11(b) and Fig. 11(c), confirm the expected behaviors of LSHAF and LAHSF. Together, these designs offer a novel approach to frequency-selective filtering and amplification, surpassing the capabilities of conventional high-pass or bandpass filters.

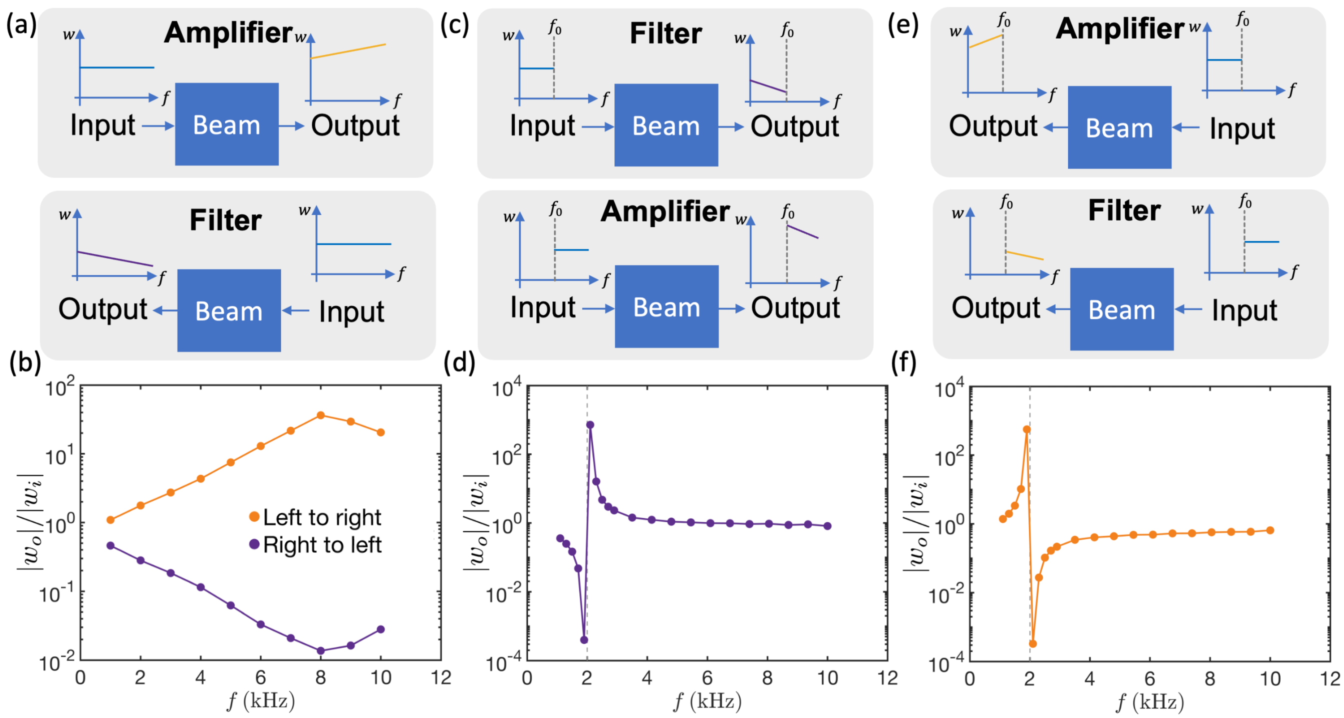

Figure 11: Utilizing nonreciprocal wave behavior for filtering and amplification. (a) For constant antisymmetric transfer functions, the Willis beam amplifies signals propagating from left to right while acting as a filter for signals traveling from right to left. (b) The ratio of output w_0 to input w_i signal as a function of excitation frequency for (a). (c) For resonant antisymmetric transfer functions, the Willis beam filters out low-frequency signals (below f_0) and amplifies high-frequency signals (above f_0) when the signal is input from the left and output at the right. (d) The ratio of output w_0 to input w_i signal as a function of excitation frequency for (c), with the dashed gray line indicating the resonant frequency $f_0 = 2$kHz. (e) For resonant antisymmetric transfer functions, the Willis beam filters out high-frequency signals (above f_0) and amplifies low-frequency signals (below f_0) when the signal is input from the right and output at the left. (f) The ratio of output w_0 to input w_i signal as a function of excitation frequency for (e), with the dashed gray line marking the resonant frequency $f_0 = 2$kHz.

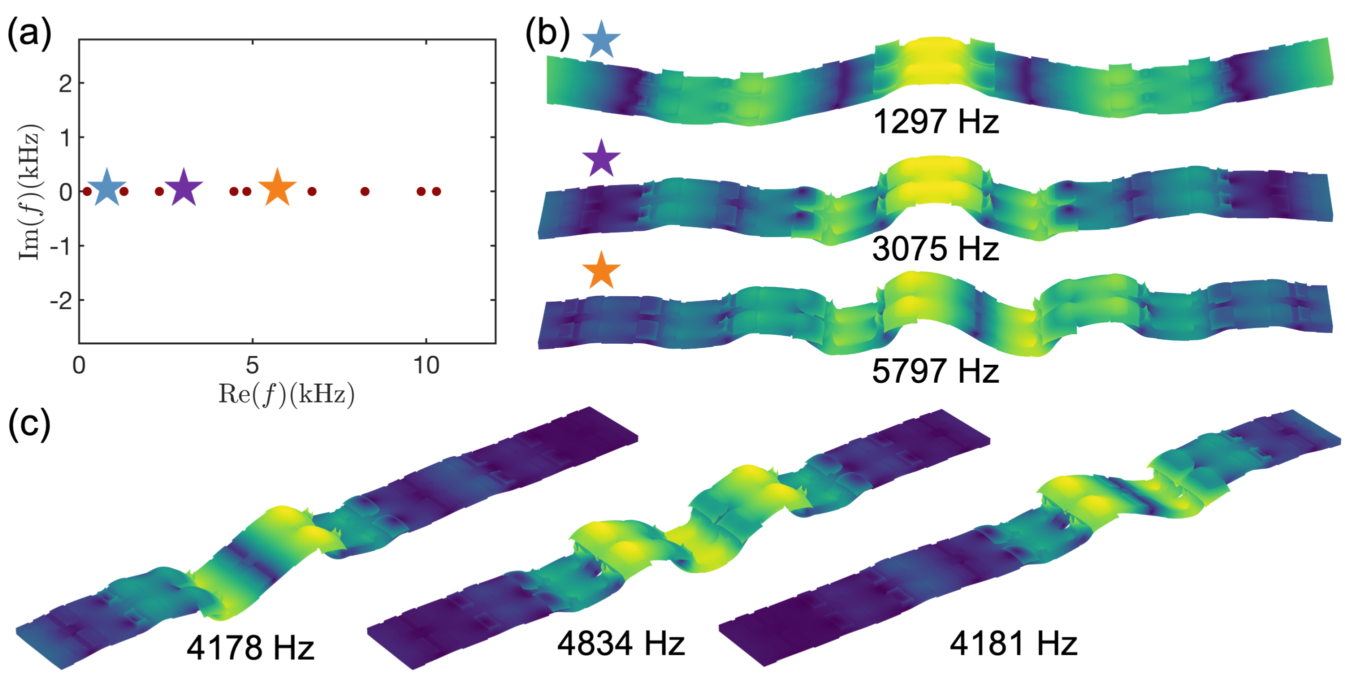

Figure 12: Non-Hermitian interface modes. (a) The frequency spectrum of a finite beam with 10 unit cells, where the interface is located at the 5th and 6th unit cells. The transfer functions for the left five unit cells are $H_1 = -H_2 = -0.3$, while for the right five unit cells, they are $H_1 = -H_2 = 0.3$. (b) Eigenmodes and their corresponding eigenfrequencies at the starred locations in the frequency spectrum of (a). (c) Eigenmodes and their eigenfrequencies for interfaces located between the 3rd and 4th unit cells (left panel), between the 5th and 6th unit cells (middle panel), and between the 7th and 8th unit cells (right panel).

5.1.1. Non-Hermitian interface modes and its potential application in energy harvest

In energy harvesting, external energy sources are often distributed across a broad area, while the harvester itself is confined to a single location. Efficiently channeling energy from multiple source points to the harvester presents a significant challenge. One approach to address this is through skin modes with a real-valued spectrum, where the real spectrum ensures system stability and prevents unwanted energy feedback from the sensor-actuator circuit into the beam. These modes naturally concentrate energy along a boundary, regardless of the source location, allowing the harvester to be placed there for effective energy collection. However, boundary localization inherently limits the flexibility of harvester placement. To overcome this constraint, we utilize non-Hermitian interface modes with a real spectrum to enable energy localization at user-defined interfaces. This approach maintains efficient energy concentration while significantly expanding the possible locations for harvester installation.

In the left and right panels of Fig. 8(c), the localization directions of the two eigenmodes are reversed. By directly connecting these configurations, each consisting of five unit cells, a beam with ten unit cells is formed, creating an interface at the center. As a result, the mode shape becomes a localized mode at the interface, as shown in Fig. 12(b). The OBC frequency spectrum remains real and is presented in Fig. 12(a), where all eigenmodes correspond to interface modes localized at the interface. For instance, three eigenmodes corresponding to the starred points in Fig. 12(a) are shown in Fig. 12(b), demonstrating that interface modes span a broad frequency range. This is particularly significant because external energy sources typically operate over a wide range of frequencies. By adjusting the interface position, energy localization can be achieved at user-defined locations. For example, the interface mode is localized at the prescribed interface between the 3rd and 4th unit cells in the left panel of Fig. 12(c), between the 5th and 6th unit cells in the middle panel, and between the 7th and 8th unit cells in the right panel. In conclusion, our design potentially enables efficient energy concentration, allows for a user-defined harvester position, and supports energy harvesting over a broad frequency range.

6. Conclusion

We developed an EMT for nonlocal non-Hermitian Willis metabeams, incorporating sensor-actuator interactions to enable active wave control. Using source-driven homogenization, we derived a dynamic effective medium model that accurately captures high-frequency and short-wavelength wave behavior, overcoming the limitations of classical homogenization approaches. This framework integrates non-Hermitian physics and Willis couplings, allowing precise control over wave amplification, attenuation, and nonreciprocal propagation.

Numerical validation through COMSOL simulations confirms the accuracy of our EMT in predicting wave dispersion and effective material properties. Additionally, we establish a bulk-boundary correspondence for nonlocal non-Hermitian Willis media, linking winding numbers to skin modes and extending topological wave mechanics to elastodynamic systems.

Beyond theoretical advancements, we demonstrate applications in nonreciprocal wave control, interface-localized energy harvesting, and low-frequency shear wave manipulation. These findings lay the foundation for active metamaterials with tunable wave properties, opening new possibilities in wave-based computing, vibration control, and energy harvesting.

CRediT authorship contribution statement

Shaoyun Wang: Writing – review & editing, Writing – original draft, Validation, Methodology, Investigation, Formal analysis, Conceptualization. Guoliang Huang: Writing – review & editing, Validation, Supervision, Funding acquisition, Formal analysis, Conceptualization, Methodology.

Declaration of Competing Interest

The authors declare no known competing financial interests or personal relationships that could have influenced the work reported in this paper.

Acknowledgments

The authors thank Dr. Zhanyu Li and Dr. Wen Cheng for their valuable discussions. Guoliang Huang acknowledges support from the Air Force Office of Scientific Research under Grant Nos. AF 9550-18-1-0342 and AF 9550-20-1-0279, with Dr. Byung-Lip (Les) Lee as the Program Manager.

Appendix A. Geometric and material parameters

The geometric parameters of the model in Fig. 2(a) are listed in Table A.1. The background beam is made of aluminum with a Young's modulus of 70 GPa, a Poisson ratio of 0.33, and a density of 2700 kg/m^3. The piezoelectric patches are composed of PZT-5H, with material properties available in the COMSOL material library. The capacitor C_0 in Eq. (12) has a value of -0.611 pF.

Table A.1: Geometry parameters of 3D model

Parameter	Value (Unit)	Parameter	Value (Unit)
w	21.9 mm	l	20 mm
w_1	16.1 mm	l_1	12 mm
w_2	8 mm	l_2	4 mm
w_3	3.5 mm	l_3	2.9 mm
h_b	2 mm	h_p	0.5 mm

Appendix B. Green's function

Appendix B.1. Displacement response in Timoshenko beam

Eliminating M, F, and ψ in the governing equations Eq. (6), we obtain

$$\begin{aligned} & D_0 \frac{\partial^4 w}{\partial x^4} + J_0 \omega^2 \left(1 + \frac{D_0 P_0}{G_0 J_0}\right) \frac{\partial^2 w}{\partial x^2} + \left(\frac{J_0 \rho_0 \omega^4}{G_0} - \rho_0 \omega^2\right) w \\ & = -\frac{\partial q}{\partial x} + \left(1 - \frac{J_0}{G_0}\omega^2\right) f - \frac{D_0}{G_0}\frac{\partial^2 f}{\partial x^2} + D_0 \frac{\partial^2 p}{\partial x^2} + D_0 \frac{\partial^3 s}{\partial x^3} + J_0 \omega^2 \frac{\partial s}{\partial x} \end{aligned} \tag{B.1}$$

If only shear force is applied as $f = \delta(x)$, the equations can be reduced as

$$D_0 \frac{\partial^4 w}{\partial x^4} + J_0 \omega^2 \left(1 + \frac{D_0 P_0}{G_0 J_0}\right) \frac{\partial^2 w}{\partial x^2} + \left(\frac{J_0 \rho_0 \omega^4}{G_0} - \rho_0 \omega^2\right) w = \left(1 - \frac{J_0}{G_0}\omega^2\right) \delta(x) - \frac{D_0}{G_0}\frac{\partial^2 \delta(x)}{\partial x^2} \tag{B.2}$$

The Fourier transform of this equation is

$$w(\omega,k)=\frac{1}{D_0}\frac{1-\frac{J_0}{G_0}\omega^2+\frac{D_0}{G_0}k^2}{(k^2+a^2)(k^2+b^2)} \tag{B.3}$$

Here $a=ik_1, b=k_2$, and k_1 (pure real) and k_2 (pure real) satisfy the dispersion relation of Timoshenko beam for a given angular frequency ω

$$\det[\boldsymbol{\zeta}(\mathrm{k},\omega)]=0. \tag{B.4}$$

The inverse Fourier transform using MATLAB symbolic calculation is

$$w(\omega,x)=-\frac{1}{2D_0}\frac{1-\frac{J_0}{G_0}\omega^2-\frac{D_0}{G_0}a^2}{(a^2-b^2)a}e^{-a|x|}+\frac{1}{2D_0}\frac{1-\frac{J_0}{G_0}\omega^2-\frac{D_0}{G_0}b^2}{(a^2-b^2)b}e^{-b|x|} \tag{B.5}$$

or equivalently,

$$w(\omega,x)=\frac{1}{2D_0}\frac{1-\frac{J_0}{G_0}\omega^2+\frac{D_0}{G_0}k_1^2}{(k_1^2+k_2^2)ik_1}e^{-ik_1|x|}-\frac{1}{2D_0}\frac{1-\frac{J_0}{G_0}\omega^2-\frac{D_0}{G_0}k_2^2}{(k_1^2+k_2^2)k_2}e^{-k_2|x|} \tag{B.6}$$

Smilarily, for delta source q only, the displacement response is

$$w(\omega,x)=\frac{1}{2D_0(k_1^2+k_2^2)}e^{-ik_1|x|}\mathrm{sgn}(x)-\frac{1}{2D_0(k_1^2+k_2^2)}e^{-k_2|x|}\mathrm{sgn}(x), \tag{B.7}$$

for delta source p only, the displacement response is

$$w(\omega,x)=\frac{ik_1}{2(k_1^2+k_2^2)}e^{-ik_1|x|}-\frac{k_2}{2(k_1^2+k_2^2)}e^{-k_2|x|}, \tag{B.8}$$

and for delta source s only, the displacement response is

$$w(\omega,x)=-\frac{-D_0k_1^2+J_0\omega^2}{2D_0(k_1^2+k_2^2)}e^{-ik_1|x|}\mathrm{sgn}(x)+\frac{D_0k_2^2+J_0\omega^2}{2D_0(k_1^2+k_2^2)}e^{-k_2|x|}\mathrm{sgn}(x) \tag{B.9}$$

Appendix B.2. The Green's function

Because the system preserves the translational symmetry, applying the linear combination of the four type point load $f_0\delta(x-x')$, $q_0\delta(x-x')$, $p_0\delta(x-x')$, and $s_0\delta(x-x')$ at x' simultaneously, the displacement response function responded at x is

$$\begin{aligned} w(x',x) &= (p_0A_1+s_0\,\mathrm{sgn}(x-x')A_2+f_0A_3+q_0\,\mathrm{sgn}(x-x')A_4)\,e^{-ik_1|x-x'|}\\ &\quad+(p_0A_1a_1+s_0\,\mathrm{sgn}(x-x')A_2a_2+f_0A_3a_3+q_0\,\mathrm{sgn}(x-x')A_4a_4)\,e^{-k_2|x-x'|}\\ &=\mathbf{B}_1(x-x')^T\mathbf{Q}_0e^{-ik_1|x-x'|}+\mathbf{B}_2(x-x')^T\mathbf{Q}_0e^{-k_2|x-x'|} \end{aligned} \tag{B.10}$$

where

$$\mathbf{B}_1(x)=\begin{bmatrix} A_1\\ \mathrm{sgn}(x-x')A_2\\ A_3\\ \mathrm{sgn}(x-x')A_4\end{bmatrix},\quad \mathbf{B}_2(x)=\begin{bmatrix} A_1a_1\\ \mathrm{sign}(x-x')A_2a_2\\ A_3a_3\\ \mathrm{sign}(x)A_4a_4\end{bmatrix}\quad \mathbf{Q}_0=\begin{bmatrix} p_0\\ s_0\\ f_0\\ q_0\end{bmatrix}, \tag{B.11}$$

and

$$
\begin{aligned}
A_1 &= \frac{ik_1}{2(k_1^2+k_2^2)}, & a_1 &= -\frac{k_2}{ik_1}, \\
A_2 &= \frac{D_0k_1^2-J_0\omega^2}{2D_0(k_1^2+k_2^2)}, & a_2 &= \frac{D_0k_2^2+J_0\omega^2}{D_0k_1^2-J_0\omega^2}, \\
A_3 &= \frac{1}{2D_0}\frac{1-\frac{J_0}{G_0}\omega^2+\frac{D_0}{G_0}k_1^2}{(k_1^2+k_2^2)ik_1}, & a_3 &= -\frac{ik_1}{k_2}\frac{1-\frac{J_0}{G_0}\omega^2-\frac{D_0}{G_0}k_2^2}{1-\frac{J_0}{G_0}\omega^2+\frac{D_0}{G_0}k_1^2}, \\
A_4 &= \frac{1}{2D_0(k_1^2+k_2^2)}, & a_4 &= -1.
\end{aligned}
\tag{B.12}
$$

Meanwhile, the response functions $\psi(x',x)$, $F(x',x)$, and $M(x',x)$ can be assumed as

$$
\begin{aligned}
\psi(x',x) &= R_\psi^1(x-x')\mathbf{B}_1(x-x')^T\mathbf{Q}(x')e^{-ik_1|x-x'|}+R_\psi^2(x-x')\mathbf{B_2}(x-x')^T\mathbf{Q}(x')e^{-k_2|x-x'|} \\
F(x',x) &= R_F^1(x-x')\mathbf{B_1}(x-x')^{\mathbf{T}}\mathbf{Q}(x')e^{-ik_1|x-x'|}+R_F^2(x-x')\mathbf{B_2}(x-x')^{\mathbf{T}}\mathbf{Q}(x')e^{-k_2|x-x'|} \\
M(x',x) &= R_M^1(x-x')\mathbf{B_1}(x-x')^T\mathbf{Q}(x')e^{-ik_1|x-x'|}+R_M^2(x-x')\mathbf{B_2}(x-x')^T\mathbf{Q}(x')e^{-k_2|x-x'|}
\end{aligned}
\tag{B.13}
$$

Inserting them into the first three equations of Eq. (6) with the aid of Eq. (B.10), we obtain the following linear equations

$$
\begin{aligned}
&-\operatorname{sgn}(x-x')ik_1R_\psi^1(x-x')+\frac{R_M^1(x-x')}{D_0}=0 \\
&R_\psi^1(x-x')+\frac{R_F^1(x-x')}{G_0}=-\operatorname{sgn}(x-x')ik_1 \\
&-\operatorname{sgn}(x-x')ik_1R_F^1(x-x')=-\rho_0\omega^2
\end{aligned}
\tag{B.14}
$$

for $R_\psi^1(x-x'), R_F^1(x-x'), R_M^1(x-x')$, and the linear equations

$$
\begin{aligned}
&-\operatorname{sgn}(x-x')k_2R_\psi^2(x-x')+\frac{R_M^2(x-x')}{D_0}=0 \\
&R_\psi^2(x-x')+\frac{R_F^2(x-x')}{G_0}=-\operatorname{sgn}(x-x')k_2 \\
&-\operatorname{sgn}(x-x')k_2R_F^2(x-x')=-\rho_0\omega^2
\end{aligned}
\tag{B.15}
$$

for $R_\psi^2(x-x'), R_F^2(x-x'), R_M^2(x-x')$. Solving these equations yields $R_\psi^1(x-x')$, $R_F^1(x-x')$, $R_M^1(x-x')$, as well as $R_\psi^2(x-x')$, $R_F^2(x-x')$, and $R_M^2(x-x')$.

Therefore, the Green's function in the frequency domain is

$$
\mathbf{G}(\omega,x-x')=\mathbf{R}_1(x-x')\mathbf{B}_1(x-x')^Te^{-ik_1|x-x'|}+\mathbf{R}_2(x-x')\mathbf{B}_2(x-x')^Te^{-k_2|x-x'|}
\tag{B.16}
$$

and

$$
\mathbf{R}_1(x)=\begin{bmatrix} R_M^1(x) \\ R_F^1(x) \\ 1 \\ R_\psi^1(x) \end{bmatrix},\quad \mathbf{R}_2(x)=\begin{bmatrix} R_M^2(x) \\ R_F^2(x) \\ 1 \\ R_\psi^2(x) \end{bmatrix}.
\tag{B.17}
$$

And the state vector response $\mathbf{u}(x)$ at x, excited by a source vector $\mathbf{Q}(x')$ at x', is given by

$$\mathbf{u}(x) = \int \mathbf{G}(\omega, x - x')\mathbf{Q}(x')dx'. \tag{B.18}$$

Appendix C. Symmetry conditions of Green's function

As shown in the middle panel of Fig. 2(b), the periodic actuators can be regarded as periodic scatterers, inducing multiple scattering effects. To account for these effects, we construct the Green's function of the background beam and analyze its symmetry. The Green's function for Eq. (6) satisfies

$$\boldsymbol{\zeta}_1 \mathbf{G}(x - x') = \delta(x - x')\mathbf{I} \tag{C.1}$$

where the analytical expression of Green's function is presented in Appendix B. Using the Fourier transform

$$G_{ij}(\omega, k) = \frac{1}{\sqrt{2\pi}} \int_{-\infty}^{\infty} G_{ij}(\omega, x - x')e^{ik(x-x')}d(x - x'), \quad i, j = 1, 2, 3, 4. \tag{C.2}$$

We find the corresponding Green's function $\mathbf{G}(\omega, k)$ in the frequency-wavenumber domain satisfies

$$\boldsymbol{\zeta}(\omega, k)\mathbf{G}(\omega, k) = \mathbf{I}. \tag{C.3}$$

It is evident that $\boldsymbol{\zeta}(\omega, k)$ satisfies $\boldsymbol{\zeta}(\omega, k) = \boldsymbol{\zeta}^{\dagger}(\omega, k)$, $\boldsymbol{\zeta}(\omega, k) = \boldsymbol{\zeta}^{T}(\omega, -k)$, and $\boldsymbol{\zeta}(\omega, k) = \boldsymbol{\zeta}^{*}(-\omega, -k)$. Consequently, the Green's function $\mathbf{G}(\omega, k)$ also satisfies the Hermitian condition for given ω and k

$$\mathbf{G}(\omega, k) = \mathbf{G}^{\dagger}(\omega, k), \quad \mathbf{G}(\omega, k) = \mathbf{G}^{T}(\omega, -k), \quad \mathbf{G}(\omega, k) = \mathbf{G}^{*}(-\omega, -k) \tag{C.4}$$

Using the inverse Fourier transform

$$G_{ij}(\omega, x - x') = \frac{1}{\sqrt{2\pi}} \int_{-\infty}^{\infty} G_{ij}(\omega, k)e^{ik(x-x')}dk, \quad i, j = 1, 2, 3, 4, \tag{C.5}$$

the Green's function $\mathbf{G}(\omega, x - x')$ satisfies the following symmetry

$$\mathbf{G}(\omega, x - x') = \mathbf{G}^{\dagger}(\omega, x - x'), \quad \mathbf{G}(\omega, x - x') = \mathbf{G}^{T}(\omega, x' - x), \quad \mathbf{G}(\omega, x - x') = \mathbf{G}^{*}(-\omega, x' - x) \tag{C.6}$$

Appendix D. Derivation of effective constitutive relations

The $\boldsymbol{\zeta}$ is not a singular matrix in general, so Eq. (22) can be rewritten as

$$\mathbf{u}_{\text{ext}} = \mathbf{u}_{\text{eff}} + \boldsymbol{\zeta}^{-1}\mathbf{Q}_{\text{eff}}. \tag{D.1}$$

In addition, through the elimination of the local source vector $\mathbf{Q}_0$ in Eq. (23) and Eq. (24), we find

$$\boldsymbol{\beta}\mathbf{u}_{\text{ext}} = (\mathbf{I} - \boldsymbol{\beta}\mathbf{S})\,\mathbf{Q}_{\text{eff}} l. \tag{D.2}$$

Subtracting Eq. (D.2) by the product of $\boldsymbol{\beta}$ to Eq. (D.1) gives

$$\boldsymbol{\beta}\left(\mathbf{u}_{\text{eff}}+\boldsymbol{\zeta}^{-1}\mathbf{Q}_{\text{eff}}\right)=\left(\mathbf{I}-\boldsymbol{\beta}\mathbf{S}\right)\mathbf{Q}_{\text{eff}}l \tag{D.3}$$

Reorganizing yields the effective constitutive relations in Eq. (25)

$$\mathbf{Q}_{\text{eff}}=\left[\left(\mathbf{I}-\boldsymbol{\beta}\mathbf{S}\right)l-\boldsymbol{\beta}\boldsymbol{\zeta}^{-1}\right]^{-1}\boldsymbol{\beta}\mathbf{u}_{\text{eff}} \tag{D.4}$$

Appendix E. Retrieval of local polarizability tensor

Due to the complexity of the unit cell geometry, accurately relating the local polarizability tensor $\boldsymbol{\beta}$ to the transfer functions $H_1(\omega)$ and $H_2(\omega)$ analytically is challenging. In this section, we employ a retrieval method to numerically extract the local polarizability tensor, as illustrated in Fig. 3(a). The local state vector $\mathbf{u}_{\text{loc}}$ is directly obtained from COMSOL, while the local source vector $\mathbf{Q}$ is extracted using the scattering method. For each test, given the known $\mathbf{u}_{\text{loc}}$ and $\mathbf{Q}$, we obtain four equations from Eq. (11) with $\boldsymbol{\beta}$ as the unknown. Since the polarizability tensor contains 16 unknowns, four independent scattering tests are conducted to construct a system of 16 equations, enabling the unique determination of these unknowns.

Appendix E.1. Numerical extraction of the local source vector

Here, we utilize the extracted displacement field in the frequency domain to inversely determine the local source vector $\mathbf{Q}$. A unit cell is embedded in the middle of the background beam, with perfect matching layers on both sides (not shown). A unit transverse force is applied at a specified position in the background beam, as illustrated in Fig. 3(a). In this section, we use asymmetric constant transfer function with $H_1(\omega)=0.35$ and $H_2(\omega)=-0.25$. According to Eq. (B.10), the analytical displacement response function at position x for an excitation applied at the origin is given by

$$w(0,x)=\mathbf{B}_1(x)^T\mathbf{Q}_0e^{-ik_1|x|}+\mathbf{B}_2(x)^T\mathbf{Q}_0e^{-k_2|\mathbf{x}|}. \tag{E.1}$$

Meanwhile, the scattered displacement field is extracted from COMSOL. For each test, we perform two simulations: one with the transfer function set to zero and another with a nonzero transfer function. The scattered displacement field is then obtained by subtracting the displacement field of the zero-transfer-function case from that of the nonzero-transfer-function case. For the ith test, we acquire the scattered displacement vector $\mathbf{w}^i=[w^i(0,x_1),\ldots,w^i(0,x_N)]^T$ at positions $\mathbf{x}=[x_1,x_2,\ldots,x_N]^T$. At each position, Eq. (E.1) must be satisfied, leading to

$$\begin{aligned}\left[\mathbf{B}_1(x_1)^Te^{-ik_1|x_1|}+\mathbf{B}_2(x_1)^Te^{-k_2|x_1|}\right]\mathbf{Q}^i&=w^i(0,x_1)\\\left[\mathbf{B}_1(x_2)^Te^{-ik_1|x_2|}+\mathbf{B}_2(x_2)^Te^{-k_2|x_2|}\right]\mathbf{Q}^i&=w^i(0,x_2)\\&\cdots\\\left[\mathbf{B}_1(x_N)^Te^{-ik_1|x_N|}+\mathbf{B}_2(x_N)^Te^{-k_2|x_N|}\right]\mathbf{Q}^i&=w^i(0,x_N).\end{aligned} \tag{E.2}$$

Here, N is chosen to be greater than 4, and $\mathbf{Q}^i$ is determined using the least squares method. To achieve the desired precision, a large integer N (2000 in this study) is selected. By solving the overdetermined system using the least

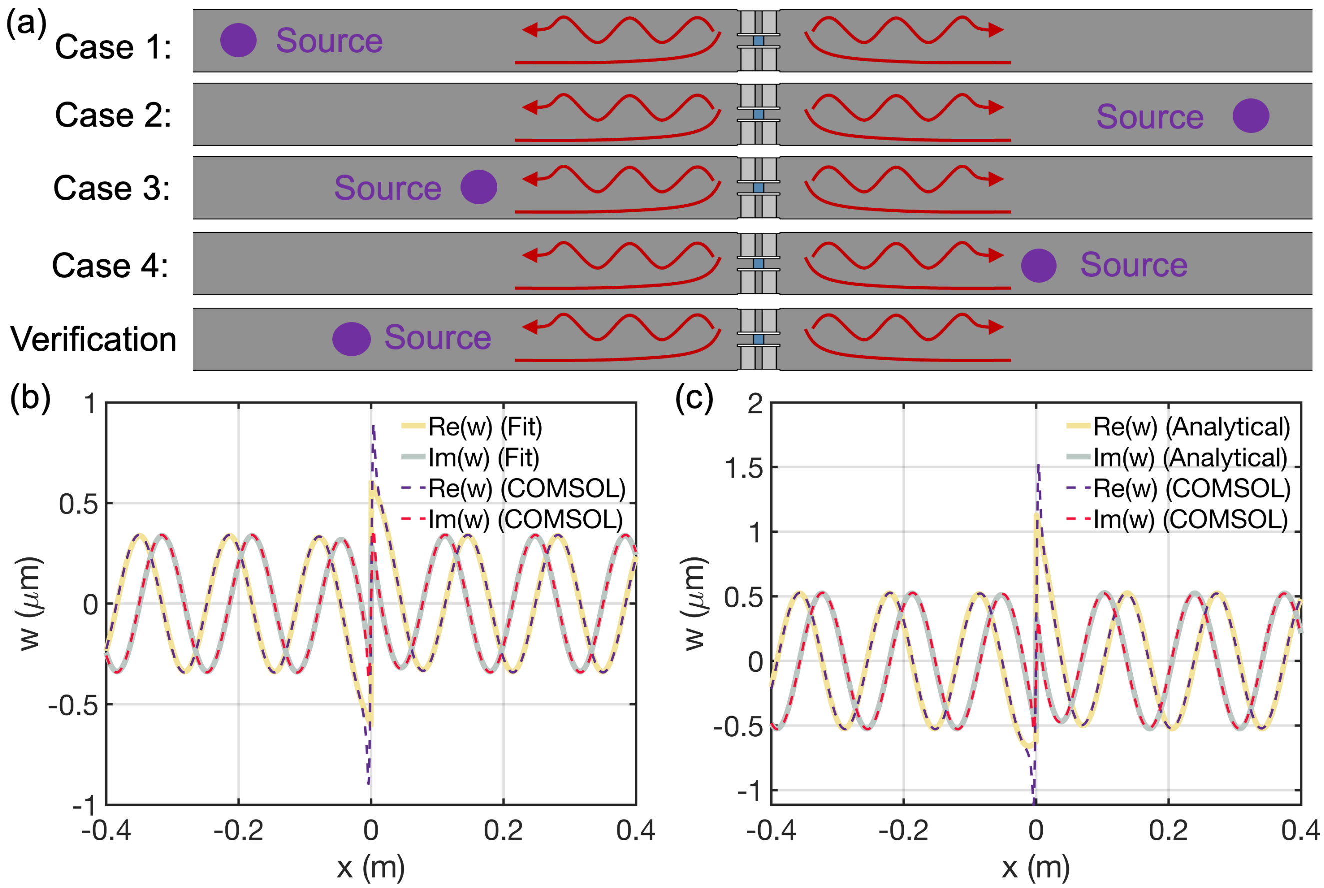

Figure E.13: Numerical extraction of the polarizability tensor. (a) Four numerical tests for extracting the polarizability tensor, along with an additional case for verification. (b) Real part (purple dashed line) and imaginary part (red dashed line) of the scattered displacement field from COMSOL simulations for the first case in (a), compared with the fitted response of a point source (yellow solid line for the real part and gray solid line for the imaginary part). (c) Real part (purple dashed line) and imaginary part (red dashed line) of the scattered displacement field from COMSOL simulations for the verification case in (a), compared with the analytical response of a point source derived from the four tests in (a) (yellow solid line for the real part and gray solid line for the imaginary part).

squares method, we obtain

$$\mathbf{Q}^i = \mathcal{G}^{-1}\mathbf{w}^i \tag{E.3}$$

where $(\cdot)^{-1}$ denotes the Moore–Penrose pseudoinverse, and the rectangular matrix $\mathcal{G}$ is defined as

$$\mathcal{G} = \begin{bmatrix} \mathbf{B}_1(x_1)^T e^{-ik_1|x_1|} + \mathbf{B}_2(x_1)^T e^{-k_2|x_1|} \\ \mathbf{B}_1(x_2)^T e^{-ik_1|x_2|} + \mathbf{B}_2(x_2)^T e^{-k_2|x_2|} \\ \dots \\ \mathbf{B}_1(x_N)^T e^{-ik_1|x_N|} + \mathbf{B}_2(x_N)^T e^{-k_2|x_N|} \end{bmatrix} \tag{E.4}$$

To assess the accuracy of the inverse extraction, we compare the analytical scattered displacement field, computed using Eq. (E.1) with the inversely obtained $\mathbf{Q}^i$, against the scattered displacement field extracted from the COMSOL simulation for the first case, as shown in Fig. 3(b). The real and imaginary parts of both results closely match, except in the region very close to the unit cell, where microstructural effects become significant. This confirms that the point source assumption is valid for our study and that the inverse extraction method is reliable.

Appendix E.2. Numerical extraction of the polarizability tensor

Now we have four local source vectors for four tests. The four local state vectors can be extracted in COMOSL directly. Therefore, for these four tests, the following condition is satisfied according to Eq. (11)

$$\mathbf{Q}^i = \boldsymbol{\beta}\mathbf{u}^i_{\mathrm{loc}}, \quad i = 1, 2, 3, 4, \tag{E.5}$$

These linear equations can also be expressed as:

$$\mathbf{Q}^i = u^i_{\mathrm{loc}}(1)\boldsymbol{\beta}_1 + u^i_{\mathrm{loc}}(2)\boldsymbol{\beta}_2 + u^i_{\mathrm{loc}}(3)\boldsymbol{\beta}_3 + u^i_{\mathrm{loc}}(4)\boldsymbol{\beta}_4, \quad i = 1, 2, 3, 4, \tag{E.6}$$

where $\boldsymbol{\beta}_j$ $(j = 1, 2, 3, 4)$ is the jth column vector of the matrix $\boldsymbol{\beta}$, and $u^i_{\mathrm{loc}}(j)$ $(j = 1, 2, 3, 4)$ is the jth element of the vector $\mathbf{u}^i_{\mathrm{loc}}$. Eq. (E.6) can be reformulated as:

$$\begin{bmatrix} \mathbf{Q}^1 \\ \mathbf{Q}^2 \\ \mathbf{Q}^3 \\ \mathbf{Q}^4 \end{bmatrix} = \begin{bmatrix} u^1_{\mathrm{loc}}(1)\mathbf{I} & u^1_{\mathrm{loc}}(2)\mathbf{I} & u^1_{\mathrm{loc}}(3)\mathbf{I} & u^1_{\mathrm{loc}}(4)\mathbf{I} \\ u^2_{\mathrm{loc}}(1)\mathbf{I} & u^2_{\mathrm{loc}}(2)\mathbf{I} & u^2_{\mathrm{loc}}(3)\mathbf{I} & u^2_{\mathrm{loc}}(4)\mathbf{I} \\ u^3_{\mathrm{loc}}(1)\mathbf{I} & u^3_{\mathrm{loc}}(2)\mathbf{I} & u^3_{\mathrm{loc}}(3)\mathbf{I} & u^3_{\mathrm{loc}}(4)\mathbf{I} \\ u^4_{\mathrm{loc}}(1)\mathbf{I} & u^4_{\mathrm{loc}}(2)\mathbf{I} & u^4_{\mathrm{loc}}(3)\mathbf{I} & u^4_{\mathrm{loc}}(4)\mathbf{I} \end{bmatrix} \begin{bmatrix} \boldsymbol{\beta}_1 \\ \boldsymbol{\beta}_2 \\ \boldsymbol{\beta}_3 \\ \boldsymbol{\beta}_4 \end{bmatrix}, \tag{E.7}$$

where $\mathbf{I}$ is the 4×4 identity matrix. We concatenate $\mathbf{Q}^i$ and $\boldsymbol{\beta}_i$ $(i = 1, 2, 3, 4)$ to form larger vectors and assemble $\mathbf{u}^i_{\mathrm{loc}}$ $(i = 1, 2, 3, 4)$ into a matrix

$$\mathfrak{Q} = \begin{bmatrix} \mathbf{Q}^1 \\ \mathbf{Q}^2 \\ \mathbf{Q}^3 \\ \mathbf{Q}^4 \end{bmatrix}, \quad \mathfrak{U}_{\mathrm{loc}} = \begin{bmatrix} \left(\mathbf{u}^1_{\mathrm{loc}}\right)^T \\ \left(\mathbf{u}^2_{\mathrm{loc}}\right)^T \\ \left(\mathbf{u}^3_{\mathrm{loc}}\right)^T \\ \left(\mathbf{u}^4_{\mathrm{loc}}\right)^T \end{bmatrix}, \quad \mathfrak{B} = \begin{bmatrix} \boldsymbol{\beta}_1 \\ \boldsymbol{\beta}_2 \\ \boldsymbol{\beta}_3 \\ \boldsymbol{\beta}_4 \end{bmatrix}. \tag{E.8}$$

Then Eq. (E.7) can be expressed as

$$\mathfrak{Q} = \mathfrak{U}_{\mathrm{loc}} \otimes \mathbf{I}\mathfrak{B}, \tag{E.9}$$

where $\otimes$ is the Kronecker product. Solving for $\mathfrak{B}$, we obtain

$$\mathfrak{B} = \left(\mathfrak{U}_{\mathrm{loc}} \otimes \mathbf{I}\right)^{-1} \mathfrak{Q} \tag{E.10}$$

Finally, the local polarizability matrix $\boldsymbol{\beta}$ is obtained by rearranging the elements of the vector $\mathfrak{B}$. Since the polarizability matrix is generally frequency-dependent, we conduct these four tests at different frequencies and derive the frequency-dependent polarizability matrix function through curve fitting.

Finally, we verify the local polarizability matrix $\boldsymbol{\beta}$ through a validation test, as shown in the bottom panel of Fig. 3(a). In this case, the source position differs from those in the four previous cases. First, the local state vector is extracted, and then the local source vector is determined by multiplying the local state vector by the local polarizability matrix. Using Eq. (E.1), the analytical scattered displacement field is then computed for the obtained local source vector. This analytical result is compared with the scattered displacement field extracted from the

COMSOL simulation in Fig. 3(c). The consistency between the two results confirms the validity of the point source assumption and the reliability of the retrieval method for determining the polarizability matrix.

Appendix F. Interpretation of nonlocal effective parameters

According to our effective medium theory, the effective parameters in Eq. (25) depend on both frequency and wavenumber. However, for freely propagating waves, frequency and wavenumber are not independent but must satisfy the dispersion relation given in Eq. (47). This implies that the effective parameters are physically meaningful only at frequencies and wavenumbers that lie on the dispersion curves corresponding to freely traveling waves. This raises an apparent paradox: whether the effective parameters remain meaningful for arbitrary frequency and wavenumber, or whether the assumption of independent frequency and wavenumber in the effective parameters requires further justification.

To treat frequency and wavenumber as independent variables, we must consider waves under external excitation. We begin by introducing a traveling wave excitation of the form

$$\mathbf{Q}_{\text{ext}}(x,t) = \mathbf{Q}_{\text{ext}}(\omega,k)e^{i(kx-\omega t)} \tag{F.1}$$

where $\mathbf{Q}_{\text{ext}}(\omega,k)$ represents the amplitude, which depends on both frequency and wavenumber. The solution to Eq. (43) can then be expressed as

$$\mathbf{u}_{\text{eff}}(x,t) = \mathbf{u}_{\text{eff}}(\omega,k)e^{i(kx-\omega t)} \tag{F.2}$$

where the amplitude vector satisfies

$$\mathbf{u}_{\text{eff}}(\omega,k) = \mathbf{H}(\omega,k)^{-1}\mathbf{Q}_{\text{ext}}(\omega,k). \tag{F.3}$$

If the frequency and wavenumber satisfy the dispersion relation, $\mathbf{H}(\omega,k)$ becomes singular, causing the amplitude vector to diverge, similar to resonance in vibrational systems. To eliminate this singularity, damping can be introduced into the system, ensuring that the amplitude vector remains finite. Conversely, if the frequency and wavenumber do not satisfy the dispersion relation, $\mathbf{H}(\omega,k)$ remains nonsingular, and the amplitude vector is naturally finite. In this case, the amplitude vector depends on $\mathbf{H}(\omega,k)$, which in turn is determined by the effective parameters, allowing frequency and wavenumber to be treated as independent variables.

Next, we consider a more realistic harmonic excitation of the form

$$\mathbf{Q}_{\text{ext}}(x,t) = \mathbf{Q}_{\text{ext}}(\omega,x)e^{-i\omega t}, \tag{F.4}$$

which can be expanded as

$$\mathbf{Q}_{\text{ext}}(x,t) = \frac{e^{-i\omega t}}{\sqrt{2\pi}}\int_{-\infty}^{\infty}\mathbf{Q}_{\text{ext}}(\omega,k)e^{ikx}dk. \tag{F.5}$$

For each Fourier component $\mathbf{Q}_{\text{ext}}(\omega,k)$, the corresponding response is given by $\mathbf{u}_{\text{eff}}(\omega,k)$. Using the principle of superposition, the total response can be written as

$$\mathbf{u}_{\text{eff}}(t,x) = \frac{e^{-i\omega t}}{\sqrt{2\pi}}\int_{-\infty}^{\infty}\mathbf{H}(\omega,k)^{-1}\mathbf{Q}_{\text{ext}}(\omega,k)e^{ikx}dk. \tag{F.6}$$

This result shows that the state vector response depends on the effective parameters for arbitrary frequency and wavenumber. Therefore, in the context of excitation problems, frequency and wavenumber can be treated as independent variables. Furthermore, this approach offers greater flexibility in modulating the effective parameters, as both frequency and wavenumber can be controlled. For example, a gradient medium with slowly varying properties can be designed using the WKB approximation to develop an elastic ray theory, enabling novel wave propagation phenomena (Wang et al., 2023).

References

Agranovich, V. M. and Ginzburg, V. (2013). *Crystal optics with spatial dispersion, and excitons*, volume 42. Springer Science & Business Media.

Altman, C. and Suchy, K. (2011). *Reciprocity, spatial mapping and time reversal in electromagnetics*. Springer Science & Business Media.

Alù, A. (2011). First-principles homogenization theory for periodic metamaterials. *Physical Review B—Condensed Matter and Materials Physics*, 84(7):075153.

Ashida, Y., Gong, Z., and Ueda, M. (2020). Non-hermitian physics. *Advances in Physics*, 69(3):249–435.

Baz, A. (2024). Why active willis metamaterials? a controllability and observability perspective. *The Journal of the Acoustical Society of America*, 156(5):3338–3352.

Bender, C. M. and Boettcher, S. (1998). Real spectra in non-hermitian hamiltonians having p t symmetry. *Physical review letters*, 80(24):5243.

Bender, C. M. and Hook, D. W. (2024). Pt-symmetric quantum mechanics. *Reviews of Modern Physics*, 96(4):045002.

Chen, Y. and Haberman, M. R. (2023). Controlling displacement fields in polar willis solids via gauge transformations. *Physical Review Letters*, 130(14):147201.

Chen, Y., Li, X., Hu, G., Haberman, M. R., and Huang, G. (2020). An active mechanical willis meta-layer with asymmetric polarizabilities. *Nature communications*, 11(1):3681.

Chen, Y., Li, X., Scheibner, C., Vitelli, V., and Huang, G. (2021). Realization of active metamaterials with odd micropolar elasticity. *Nature communications*, 12(1):5935.

Cheng, W. and Hu, G. (2022). Acoustic skin effect with non-reciprocal willis materials. *Applied Physics Letters*, 121(4).

Christensen, J., Haberman, M. R., Srivastava, A., Huang, G., and Shmuel, G. (2024). Perspective on non-hermitian elastodynamics. *Applied Physics Letters*, 125(23).

Galiffi, E., Tirole, R., Yin, S., Li, H., Vezzoli, S., Huidobro, P. A., Silveirinha, M. G., Sapienza, R., Alù, A., and Pendry, J. B. (2022). Photonics of time-varying media. *Advanced Photonics*, 4(1):014002–014002.

Goldstein, H., Poole, C., and Safko, J. (2002). *Classical Mechanics*. Addison Wesley.

Huang, H., Sun, C., and Huang, G. (2009). On the negative effective mass density in acoustic metamaterials. *International Journal of Engineering Science*, 47(4):610–617.

Jackson, J. (2012). *Classical Electrodynamics*. Wiley.

Landau, L., Landau, L., Lifshits, E., Kosevich, A., Lifshitz, E., and Pitaevskii, L. (1986). *Theory of Elasticity: Volume 7*. Course of theoretical physics. Butterworth-Heinemann.

Landau, L., Lifshitz, E., and Sykes, J. (1976). *Mechanics: Volume 1*. Course of theoretical physics. Butterworth-Heinemann.

Lee, J.-H., Zhang, Z., and Gu, G. X. (2023). Dynamic homogenization of heterogeneous piezoelectric media: a polarization approach using infinite-body green's function. *Journal of the Mechanics and Physics of Solids*, 181:105442.

Li, J., Shen, C., Díaz-Rubio, A., Tretyakov, S. A., and Cummer, S. A. (2018). Systematic design and experimental demonstration of bianisotropic metasurfaces for scattering-free manipulation of acoustic wavefronts. *Nature communications*, 9(1):1342.

Li, Z., Han, P., and Hu, G. (2024). Willis dynamic homogenization method for acoustic metamaterials based on multiple scattering theory. *Journal of the Mechanics and Physics of Solids*, 189:105692.

Li, Z., Qu, H., Zhang, H., Liu, X., and Hu, G. (2022). Interfacial wave between acoustic media with willis coupling. *Wave Motion*, 112:102922.

Liu, Y., Liang, Z., Zhu, J., Xia, L., Mondain-Monval, O., Brunet, T., Alù, A., and Li, J. (2019). Willis metamaterial on a structured beam. *Physical Review X*, 9(1):011040.

Milton, G. W. (2007). New metamaterials with macroscopic behavior outside that of continuum elastodynamics. *New Journal of Physics*, 9(10):359.

Milton, G. W., Briane, M., and Willis, J. R. (2006). On cloaking for elasticity and physical equations with a transformation invariant form. *New journal of physics*, 8(10):248.

Milton, G. W. and Willis, J. R. (2010). Minimum variational principles for time-harmonic waves in a dissipative medium and associated variational principles of hashin–shtrikman type. *Proceedings of the Royal Society A: Mathematical, Physical and Engineering Sciences*, 466(2122):3013–3032.

Miri, M.-A. and Alu, A. (2019). Exceptional points in optics and photonics. *Science*, 363(6422):eaar7709.

Muhafra, K., Haberman, M. R., and Shmuel, G. (2023). Discrete one-dimensional models for the electromomentum coupling. *Physical Review Applied*, 20(1):014042.

Muhlestein, M. B., Sieck, C. F., Wilson, P. S., and Haberman, M. R. (2017). Experimental evidence of willis coupling in a one-dimensional effective material element. *Nature communications*, 8(1):15625.

Nassar, H., He, Q.-C., and Auffray, N. (2015). Willis elastodynamic homogenization theory revisited for periodic media. *Journal of the Mechanics and Physics of Solids*, 77:158–178.

Nassar, H., He, Q.-C., and Auffray, N. (2016). On asymptotic elastodynamic homogenization approaches for periodic media. *Journal of the Mechanics and Physics of Solids*, 88:274–290.

Nassar, H., Yousefzadeh, B., Fleury, R., Ruzzene, M., Alù, A., Daraio, C., Norris, A. N., Huang, G., and Haberman, M. R. (2020). Nonreciprocity in acoustic and elastic materials. *Nature Reviews Materials*, 5(9):667–685.

Nemat-Nasser, S. and Srivastava, A. (2011). Overall dynamic constitutive relations of layered elastic composites. *Journal of the Mechanics and Physics of Solids*, 59(10):1953–1965.

Norris, A. N., Shuvalov, A., and Kutsenko, A. (2012). Analytical formulation of three-dimensional dynamic homogenization for periodic elastic systems. *Proceedings of the Royal Society A: Mathematical, Physical and Engineering Sciences*, 468(2142):1629–1651.

Okuma, N., Kawabata, K., Shiozaki, K., and Sato, M. (2020). Topological origin of non-hermitian skin effects. *Physical review letters*, 124(8):086801.

Pernas-Salomón, R., Haberman, M. R., Norris, A. N., and Shmuel, G. (2021). The electromomentum effect in piezoelectric willis scatterers. *Wave Motion*, 106:102797.

Pernas-Salomón, R. and Shmuel, G. (2018). Dynamic homogenization of composite and locally resonant flexural systems. *Journal of the Mechanics and Physics of Solids*, 119:43–59.

Pernas-Salomón, R. and Shmuel, G. (2020a). Fundamental principles for generalized willis metamaterials. *Physical Review Applied*, 14(6):064005.

Pernas-Salomón, R. and Shmuel, G. (2020b). Symmetry breaking creates electro-momentum coupling in piezoelectric metamaterials. *Journal of the Mechanics and Physics of Solids*, 134:103770.

Ponge, M.-F., Poncelet, O., and Torrent, D. (2017). Dynamic homogenization theory for nonlocal acoustic metamaterials. *Extreme Mechanics Letters*, 12:71–76.

Qu, H., Liu, X., and Hu, G. (2022). Mass-spring model of elastic media with customizable willis coupling. *International Journal of Mechanical Sciences*, 224:107325.

Rabczuk, T., Ren, H., and Zhuang, X. (2023). Computational methods based on peridynamics and nonlocal operators. In *Computational Methods in Engineering & the Sciences*. Springer.

Sakurai, J. and Napolitano, J. (2017). *Modern Quantum Mechanics*. Cambridge University Press.

Shokri, B. and Rukhadze, A. A. (2019). *Electrodynamics of Conducting Dispersive Media*. Springer.

Shore, R. A. and Yaghjian, A. D. (2007). Traveling waves on two-and three-dimensional periodic arrays of lossless scatterers. *Radio Science*, 42(06):1–40.

Shuvalov, A., Kutsenko, A., Norris, A., and Poncelet, O. (2011). Effective willis constitutive equations for periodically stratified anisotropic elastic media. *Proceedings of the Royal Society A: Mathematical, Physical and Engineering Sciences*, 467(2130):1749–1769.

Sieck, C. F., Alù, A., and Haberman, M. R. (2017). Origins of willis coupling and acoustic bianisotropy in acoustic metamaterials through source-driven homogenization. *Physical Review B*, 96(10):104303.

Srivastava, A. (2015). Elastic metamaterials and dynamic homogenization: a review. *International Journal of Smart and Nano Materials*, 6(1):41–60.

Wang, S., Hu, Z., Wu, Q., Chen, H., Prodan, E., Zhu, R., and Huang, G. (2023). Smart patterning for topological pumping of elastic surface waves. *Science Advances*, 9(30):eadh4310.

Wang, S., Shao, N., Chen, H., Chen, J., Qian, H., Wu, Q., Duan, H., Alu, A., and Huang, G. (2025). Temporal refraction and reflection in modulated mechanical metabeams: theory and physical observation. *arXiv preprint arXiv:2501.09989*.

Wang, Y., Wu, Q., Tian, Y., and Huang, G. (2024). Non-hermitian wave dynamics of odd plates: Microstructure design and theoretical modelling. *Journal of the Mechanics and Physics of Solids*, 182:105462.

Willis, J. R. (1981). Variational principles for dynamic problems for inhomogeneous elastic media. *Wave Motion*, 3(1):1–11.

Willis, J. R. (1997). Dynamics of composites. In *Continuum micromechanics*, pages 265–290. Springer.

Willis, J. R. (2009). Exact effective relations for dynamics of a laminated body. *Mechanics of Materials*, 41(4):385–393.

Willis, J. R. (2011). Effective constitutive relations for waves in composites and metamaterials. *Proceedings of the Royal Society A: Mathematical, Physical and Engineering Sciences*, 467(2131):1865–1879.

Willis, J. R. (2012). The construction of effective relations for waves in a composite. *Comptes rendus. Mécanique*, 340(4-5):181–192.

Wu, Q., Wang, S., Qian, H., Wang, Y., and Huang, G. (2024). Understanding of topological mode and skin mode morphing in 1d and 2d non-hermitian resonance-based meta-lattices. *Journal of the Mechanics and Physics of Solids*, 193:105907.

Wu, Q., Xu, X., Qian, H., Wang, S., Zhu, R., Yan, Z., Ma, H., Chen, Y., and Huang, G. (2023). Active metamaterials for realizing odd mass density. *Proceedings of the National Academy of Sciences*, 120(21):e2209829120.

Wu, Q., Zhang, X., Shivashankar, P., Chen, Y., and Huang, G. (2022). Independent flexural wave frequency conversion by a linear active metalayer. *Physical Review Letters*, 128(24):244301.

Xia, Y., Riva, E., Rosa, M. I., Cazzulani, G., Erturk, A., Braghin, F., and Ruzzene, M. (2021). Experimental observation of temporal pumping in electromechanical waveguides. *Physical Review Letters*, 126(9):095501.

Yang, Z., Zhang, K., Fang, C., and Hu, J. (2020). Non-hermitian bulk-boundary correspondence and auxiliary generalized brillouin zone theory. *Physical Review Letters*, 125(22):226402.

Yao, S. and Wang, Z. (2018). Edge states and topological invariants of non-hermitian systems. *Physical review letters*, 121(8):086803.

Yao, W., Zhong, W., and Lim, C. W. (2009). *Symplectic elasticity*. World Scientific.

Yokomizo, K. and Murakami, S. (2019). Non-bloch band theory of non-hermitian systems. *Physical review letters*, 123(6):066404.

Yves, S., Fleury, R., Shmuel, G., Fruchart, M., Vitelli, V., Haberman, M. R., and Alù, A. (2024). Symmetry-driven phononic metamaterials. *arXiv preprint arXiv:2411.18556*.

Zhai, Y., Kwon, H.-S., and Popa, B.-I. (2019). Active willis metamaterials for ultracompact nonreciprocal linear acoustic devices. *Physical Review B*, 99(22):220301.

Zhang, K., Yang, Z., and Fang, C. (2020). Correspondence between winding numbers and skin modes in non-hermitian systems. *Physical Review Letters*, 125(12):126402.

Zhu, R., Liu, X., Hu, G., Sun, C., and Huang, G. (2014). Negative refraction of elastic waves at the deep-subwavelength scale in a single-phase metamaterial. *Nature communications*, 5(1):5510.

Symmetry and Its Breaking in Nonlocal Non-Hermitian Willis Beams

Shaoyun Wang

Department of Mechanical and Aerospace Engineering, University of Missouri, Columbia, Missouri 65211, USA

Guoliang Huang*

Department of Mechanics and Engineering Science, College of Engineering, Peking University, Beijing 100871, PR China

Abstract

Keywords:

Nomenclature

M, m, M_{eff}	On-site outer and inner masses and effective mass

Contents

1. General properties of nonlocal odd Willis metabeam

Previous studies focus on the discussion of properties of local Willis media. But the Willis media from dynamic homogenization are nonlocal. Here we extend the study to properties of nonlocal odd Willis media. Pernas-Salomón and Shmuel (2020a) used nonlocal constitutive relations.

*Corresponding author

Email address: guohuang@pku.edu.cn (Guoliang Huang)

1.1. Broken parity symmetry, ***correct!***

1.1.1. Symmetry analysis of macroscopic media

In classical physics, a parity transformation refers to a spatial inversion that changes the sign of spatial coordinates. In one dimension, it is equivalent to the reflection or mirror transformation. Mathematically, it is expressed as

$$x \xrightarrow{\mathcal{P}} -x. \tag{1}$$

where $\mathcal{P}$ denotes the parity transformation. In the reciprocal space, it can be expressed as

$$k \xrightarrow{\mathcal{P}} -k. \tag{2}$$

Since $M_{\mathrm{eff}}(\omega,k)$, $\mu_{\mathrm{eff}}(\omega,k)$, $\kappa_{\mathrm{eff}}(\omega,k)$, and $\gamma_{\mathrm{eff}}(\omega,k)$ are symmetric with respect to $x=0$, while $F_{\mathrm{eff}}(\omega,k)$, $J_{\mathrm{eff}}(\omega,k)$, $\gamma_{\mathrm{eff}}(\omega,k)$, and $\varphi_{\mathrm{eff}}(\omega,k)$ are antisymmetric with respect to $x=0$, it follows that $M_{\mathrm{eff}}(\omega,k)$, $\mu_{\mathrm{eff}}(\omega,k)$, $\kappa_{\mathrm{eff}}(\omega,k)$, and $\gamma_{\mathrm{eff}}(\omega,k)$ have even parity, whereas $F_{\mathrm{eff}}(\omega,k)$, $J_{\mathrm{eff}}(\omega,k)$, $\gamma_{\mathrm{eff}}(\omega,k)$, and $\varphi_{\mathrm{eff}}(\omega,k)$ have odd parity. This can be expressed as

$$\begin{aligned}
M_{\mathrm{eff}}(\omega,k) &\xrightarrow{\mathcal{P}} M_{\mathrm{eff}}(\omega,-k), & \kappa_{\mathrm{eff}}(\omega,k) &\xrightarrow{\mathcal{P}} \kappa_{\mathrm{eff}}(\omega,-k),\\
F_{\mathrm{eff}}(\omega,k) &\xrightarrow{\mathcal{P}} -F_{\mathrm{eff}}(\omega,-k), & \gamma_{\mathrm{eff}}(\omega,k) &\xrightarrow{\mathcal{P}} -\gamma_{\mathrm{eff}}(\omega,-k),\\
\mu_{\mathrm{eff}}(\omega,k) &\xrightarrow{\mathcal{P}} \mu_{\mathrm{eff}}(\omega,-k), & \upsilon_{\mathrm{eff}}(\omega,k) &\xrightarrow{\mathcal{P}} \upsilon_{\mathrm{eff}}(\omega,-k),\\
J_{\mathrm{eff}}(\omega,k) &\xrightarrow{\mathcal{P}} -J_{\mathrm{eff}}(\omega,-k), & \varphi_{\mathrm{eff}}(\omega,k) &\xrightarrow{\mathcal{P}} -\varphi_{\mathrm{eff}}(\omega,-k).
\end{aligned} \tag{3}$$

We define $\boldsymbol{\mathcal{E}} = [\boldsymbol{\varepsilon}, \mathbf{p}]^T$, $\boldsymbol{\Sigma} = [\boldsymbol{\sigma}, \mathbf{v}]^T$ and constitutive relation in Eq. (**??**) as

$$\boldsymbol{\mathcal{E}} = \boldsymbol{\mathcal{S}}\boldsymbol{\Sigma}. \tag{4}$$

It can be rewritten as the matrix form

$$\boldsymbol{\Sigma}(\omega,-k) = \mathbf{P}\boldsymbol{\Sigma}(\omega,k), \quad \boldsymbol{\mathcal{E}}(\omega,-k) = \mathbf{P}\boldsymbol{\mathcal{E}}(\omega,k) \tag{5}$$

where κ is the complex conjugation operator and

$$\mathbf{P} = \begin{bmatrix} 1 & 0 & 0 & 0 \\ 0 & -1 & 0 & 0 \\ 0 & 0 & 1 & 0 \\ 0 & 0 & 0 & -1 \end{bmatrix} \tag{6}$$

For the system with parity symmetry, the governing equations of a system must remain form-invariant under parity symmetry. Therefore, we have the following equations after parity transformation

$$\boldsymbol{\mathcal{E}}(\omega,-k) = \boldsymbol{\mathcal{S}}(\omega,-k)\boldsymbol{\Sigma}(\omega,-k) \tag{7}$$

Therefore, we have

$$\boldsymbol{\mathcal{S}}(\omega,-k)=\mathbf{P}\boldsymbol{\mathcal{S}}(\omega,k)\mathbf{P}^{-1} \tag{8}$$

Substituting Eq. (18) into Eq. (20), we have

$$\boldsymbol{\mathcal{S}}(\omega,-k)=\begin{bmatrix} \mathcal{S}_{11}(\omega,k) & -\mathcal{S}_{12}(\omega,k) & \mathcal{S}_{13}(\omega,k) & -\mathcal{S}_{14}(\omega,k) \\ -\mathcal{S}_{21}(\omega,k) & \mathcal{S}_{22}(\omega,k) & -\mathcal{S}_{23}(\omega,k) & \mathcal{S}_{24}(\omega,k) \\ \mathcal{S}_{31}(\omega,k) & -\mathcal{S}_{32}(\omega,k) & \mathcal{S}_{33}(\omega,k) & -\mathcal{S}_{34}(\omega,k) \\ -\mathcal{S}_{41}(\omega,k) & \mathcal{S}_{42}(\omega,k) & -\mathcal{S}_{43}(\omega,k) & \mathcal{S}_{44}(\omega,k) \end{bmatrix} \tag{9}$$

If parity symmetry is preserved, $\boldsymbol{\mathcal{S}}(\omega,-k)$ must be equal to $\boldsymbol{\mathcal{S}}(\omega,k)$, leading to the result

$$\begin{aligned} &\mathcal{S}_{11}(\omega,-k)=\mathcal{S}_{11}(\omega,k), \quad \mathcal{S}_{12}(\omega,-k)=-\mathcal{S}_{12}(\omega,k), \quad \mathcal{S}_{13}(\omega,-k)=\mathcal{S}_{13}(\omega,k) \quad \mathcal{S}_{14}(\omega,-k)=-\mathcal{S}_{14}(\omega,k), \\ &\mathcal{S}_{21}(\omega,-k)=-\mathcal{S}_{21}(\omega,k), \quad \mathcal{S}_{22}(\omega,-k)=\mathcal{S}_{22}(\omega,k), \quad \mathcal{S}_{23}(\omega,-k)=-\mathcal{S}_{23}(\omega,k), \quad \mathcal{S}_{24}(\omega,-k)=\mathcal{S}_{24}(\omega,k), \\ &\mathcal{S}_{31}(\omega,-k)=\mathcal{S}_{31}(\omega,k), \quad \mathcal{S}_{32}(\omega,-k)=-\mathcal{S}_{32}(\omega,k), \quad \mathcal{S}_{33}(\omega,-k)=\mathcal{S}_{33}(\omega,k), \quad \mathcal{S}_{34}(\omega,-k)=-\mathcal{S}_{34}(\omega,k), \\ &\mathcal{S}_{41}(\omega,-k)=-\mathcal{S}_{41}(\omega,k), \quad \mathcal{S}_{42}(\omega,-k)=\mathcal{S}_{42}(\omega,k), \quad \mathcal{S}_{43}(\omega,-k)=-\mathcal{S}_{43}(\omega,k), \quad \mathcal{S}_{44}(\omega,-k)=\mathcal{S}_{44}(\omega,k). \end{aligned} \tag{10}$$

With parity symmetry, the nonlocal Willis couplings ($k \neq 0$) can still be nonzero but must satisfy the symmetry conditions given in Eq. (22). This contrasts with the case of a local Willis metabeam ($k=0$), where broken parity is necessary for the emergence of Willis couplings (Liu et al., 2019). Under long wave condition $k \to 0$, antisymmetric coefficients must vanish and we obtain

$$\mathcal{S}_{12}(\omega)=\mathcal{S}_{13}(\omega)=\mathcal{S}_{21}(\omega)=\mathcal{S}_{24}(\omega)=\mathcal{S}_{31}(\omega)=\mathcal{S}_{34}(\omega)=\mathcal{S}_{42}(\omega)=\mathcal{S}_{43}(\omega)=0 \tag{11}$$

For the conventional Willis media, the local Willis couplings ($k=0$) vanish when the system preserve the parity symmetry (Liu et al., 2019; Pernas-Salomón and Shmuel, 2020a,b; Li et al., 2022, 2024; Qu et al., 2022). However, the local Willis couplings $\mathcal{S}_{14}(\omega)$, $\mathcal{S}_{23}(\omega)$, $\mathcal{S}_{32}(\omega)$, and $\mathcal{S}_{41}(\omega)$ of our metabeam still exist when the system has the parity symmetry. Additionally, when our metabeam preserves parity symmetry, the off-diagonal local elastic and density constants are zero, while the diagonal local elastic and density constants remain nonzero.

1.1.2. Symmetry of analysis of microscopic media

Through sensor actuator system, it is possible to break the parity symmetry of the microscopic (local) constitutive relation. Now we prove the equalities of macroscopic constitutive coefficients can be broken from our microscopic constitutive relation. For the local constitutive matrix, if the system preserve parity symmetry, the elements in constitutive matrix must satisfy

$$\beta_{12}(\omega)=\beta_{13}(\omega)=\beta_{21}(\omega)=\beta_{24}(\omega)=\beta_{31}(\omega)=\beta_{34}(\omega)=\beta_{42}(\omega)=\beta_{43}(\omega)=0 \tag{12}$$

In homogenization, prove that parity symmetry should be broken for nonzero Willis couplings. As long as these equalities are broken, the parity symmetry is broken. But the broken of parity symmetry of macroscopic material constants are dependent on the local material constants.

1.2. *Time-reversal symmetry*

1.2.1. *Symmetry analysis of macroscopic media*

In classical physics, a parity transformation refers to a spatial inversion that changes the sign of spatial coordinates. In one dimension, it is equivalent to the reflection or mirror transformation. Mathematically, it is expressed as

$$t \xrightarrow{\mathcal{T}} -t. \tag{13}$$

where $\mathcal{P}$ denotes the parity transformation. In the reciprocal space, it can be expressed as

$$\omega \xrightarrow{\mathcal{T}} -\omega. \tag{14}$$

Since $M_{\text{eff}}(\omega, k)$, $\mu_{\text{eff}}(\omega, k)$, $\kappa_{\text{eff}}(\omega, k)$, and $\gamma_{\text{eff}}(\omega, k)$ are symmetric with respect to $x = 0$, while $F_{\text{eff}}(\omega, k)$, $J_{\text{eff}}(\omega, k)$, $\gamma_{\text{eff}}(\omega, k)$, and $\varphi_{\text{eff}}(\omega, k)$ are antisymmetric with respect to $x = 0$, it follows that $M_{\text{eff}}(\omega, k)$, $\mu_{\text{eff}}(\omega, k)$, $\kappa_{\text{eff}}(\omega, k)$, and $\gamma_{\text{eff}}(\omega, k)$ have even parity, whereas $F_{\text{eff}}(\omega, k)$, $J_{\text{eff}}(\omega, k)$, $\gamma_{\text{eff}}(\omega, k)$, and $\varphi_{\text{eff}}(\omega, k)$ have odd parity. This can be expressed as

$$\begin{aligned}
M_{\text{eff}}(\omega, k) &\xrightarrow{\mathcal{P}} M_{\text{eff}}(\omega, -k), \quad & \kappa_{\text{eff}}(\omega, k) &\xrightarrow{\mathcal{P}} \kappa_{\text{eff}}(\omega, -k), \\
F_{\text{eff}}(\omega, k) &\xrightarrow{\mathcal{P}} F_{\text{eff}}(\omega, -k), \quad & \gamma_{\text{eff}}(\omega, k) &\xrightarrow{\mathcal{P}} \gamma_{\text{eff}}(\omega, -k), \\
\mu_{\text{eff}}(\omega, k) &\xrightarrow{\mathcal{P}} -\mu_{\text{eff}}(\omega, -k), \quad & v_{\text{eff}}(\omega, k) &\xrightarrow{\mathcal{P}} -v_{\text{eff}}(\omega, -k), \\
J_{\text{eff}}(\omega, k) &\xrightarrow{\mathcal{P}} -J_{\text{eff}}(\omega, -k), \quad & \varphi_{\text{eff}}(\omega, k) &\xrightarrow{\mathcal{P}} -\varphi_{\text{eff}}(\omega, -k).
\end{aligned} \tag{15}$$

We define $\boldsymbol{\mathcal{E}} = [\boldsymbol{\varepsilon}, \mathbf{p}]^T$, $\boldsymbol{\Sigma} = [\boldsymbol{\sigma}, \mathbf{v}]^T$ and constitutive relation in Eq. (**??**) as

$$\boldsymbol{\mathcal{E}} = \boldsymbol{\mathcal{S}}\boldsymbol{\Sigma}. \tag{16}$$

It can be rewritten as the matrix form

$$\boldsymbol{\Sigma}(-\omega, k) = \mathbf{T}\boldsymbol{\Sigma}(\omega, k), \quad \boldsymbol{\mathcal{E}}(-\omega, k) = \mathbf{T}\boldsymbol{\mathcal{E}}(\omega, k) \tag{17}$$

where κ is the complex conjugation operator and

$$\mathbf{T} = \begin{bmatrix} 1 & 0 & 0 & 0 \\ 0 & 1 & 0 & 0 \\ 0 & 0 & -1 & 0 \\ 0 & 0 & 0 & -1 \end{bmatrix} \tag{18}$$

For the system with parity symmetry, the governing equations of a system must remain form-invariant under parity symmetry. Therefore, we have the following equations after parity transformation

$$\boldsymbol{\mathcal{E}}(-\omega, k) = \boldsymbol{\mathcal{S}}(-\omega, k)\boldsymbol{\Sigma}(-\omega, k) \tag{19}$$

Therefore, we have

$$\boldsymbol{\mathcal{S}}(-\omega,k)=\mathbf{T}\boldsymbol{\mathcal{S}}(\omega,k)\mathbf{T}^{-1} \tag{20}$$

Substituting Eq. (18) into Eq. (20), we have

$$\boldsymbol{\mathcal{S}}(\omega,-k)=\begin{bmatrix} \mathcal{S}_{11}(\omega,k) & \mathcal{S}_{12}(\omega,k) & -\mathcal{S}_{13}(\omega,k) & -\mathcal{S}_{14}(\omega,k) \\ \mathcal{S}_{21}(\omega,k) & \mathcal{S}_{22}(\omega,k) & -\mathcal{S}_{23}(\omega,k) & \mathcal{S}_{24}(\omega,k) \\ -\mathcal{S}_{31}(\omega,k) & -\mathcal{S}_{32}(\omega,k) & \mathcal{S}_{33}(\omega,k) & \mathcal{S}_{34}(\omega,k) \\ -\mathcal{S}_{41}(\omega,k) & -\mathcal{S}_{42}(\omega,k) & \mathcal{S}_{43}(\omega,k) & \mathcal{S}_{44}(\omega,k) \end{bmatrix} \tag{21}$$

If parity symmetry is preserved, $\boldsymbol{\mathcal{S}}(\omega,-k)$ must be equal to $\boldsymbol{\mathcal{S}}(\omega,k)$, leading to the result

$$\begin{aligned} &\mathcal{S}_{11}(\omega,-k)=\mathcal{S}_{11}(\omega,k), && \mathcal{S}_{12}(\omega,-k)=\mathcal{S}_{12}(\omega,k), && \mathcal{S}_{13}(\omega,-k)=-\mathcal{S}_{13}(\omega,k) && \mathcal{S}_{14}(\omega,-k)=-\mathcal{S}_{14}(\omega,k), \\ &\mathcal{S}_{21}(\omega,-k)=\mathcal{S}_{21}(\omega,k), && \mathcal{S}_{22}(\omega,-k)=\mathcal{S}_{22}(\omega,k), && \mathcal{S}_{23}(\omega,-k)=-\mathcal{S}_{23}(\omega,k), && \mathcal{S}_{24}(\omega,-k)=-\mathcal{S}_{24}(\omega,k), \\ &\mathcal{S}_{31}(\omega,-k)=-\mathcal{S}_{31}(\omega,k), && \mathcal{S}_{32}(\omega,-k)=-\mathcal{S}_{32}(\omega,k), && \mathcal{S}_{33}(\omega,-k)=\mathcal{S}_{33}(\omega,k), && \mathcal{S}_{34}(\omega,-k)=\mathcal{S}_{34}(\omega,k), \\ &\mathcal{S}_{41}(\omega,-k)=-\mathcal{S}_{41}(\omega,k), && \mathcal{S}_{42}(\omega,-k)=-\mathcal{S}_{42}(\omega,k), && \mathcal{S}_{43}(\omega,-k)=\mathcal{S}_{43}(\omega,k), && \mathcal{S}_{44}(\omega,-k)=\mathcal{S}_{44}(\omega,k). \end{aligned} \tag{22}$$

With parity symmetry, the nonlocal Willis couplings ($k \neq 0$) can still be nonzero but must satisfy the symmetry conditions given in Eq. (22). This contrasts with the case of a local Willis metabeam ($k = 0$), where broken parity is necessary for the emergence of Willis couplings (Liu et al., 2019). Under low frequency condition $\omega \to 0$, antisymmetric coefficients must vanish and we obtain

$$\mathcal{S}_{13}(k)=\mathcal{S}_{14}(k)=\mathcal{S}_{23}(k)=\mathcal{S}_{24}(k)=\mathcal{S}_{31}(k)=\mathcal{S}_{32}(k)=\mathcal{S}_{41}(k)=\mathcal{S}_{42}(k)=0 \tag{23}$$

For the conventional Willis media, the local Willis couplings ($k = 0$) vanish when the system preserve the parity symmetry (Liu et al., 2019; Pernas-Salomón and Shmuel, 2020a,b; Li et al., 2022, 2024; Qu et al., 2022). However, the local Willis couplings $\mathcal{S}_{14}(\omega)$, $\mathcal{S}_{23}(\omega)$, $\mathcal{S}_{32}(\omega)$, and $\mathcal{S}_{41}(\omega)$ of our metabeam still exist when the system has the parity symmetry. Additionally, when our metabeam preserves parity symmetry, the off-diagonal local elastic and density constants are zero, while the diagonal local elastic and density constants remain nonzero.

1.3. Broken Energy Conservation and Major Symmetry

In the spacetime domain, it is

$$\begin{aligned} \boldsymbol{\mathcal{S}}^{\mathrm{e}}(t-t',x-x') &= \frac{1}{2}\begin{bmatrix} \mathbf{C}(t-t',x-x')+\mathbf{C}^T(t'-t,x'-x) & \mathbf{B}(t-t',x-x')-\mathbf{D}^T(t'-t,x'-x) \\ \mathbf{D}(t-t',x-x')-\mathbf{B}^T(t'-t,x'-x) & \boldsymbol{\rho}(t-t',x-x')+\boldsymbol{\rho}^T(t'-t,x'-x) \end{bmatrix} \\ \boldsymbol{\mathcal{S}}^{\mathrm{o}}(t-t',x-x') &= \frac{1}{2}\begin{bmatrix} \mathbf{C}(t-t',x-x')-\mathbf{C}^T(t'-t,x'-x) & \mathbf{B}(t-t',x-x')+\mathbf{D}^T(t'-t,x'-x) \\ \mathbf{D}(t-t',x-x')+\mathbf{B}^T(t'-t,x'-x) & \boldsymbol{\rho}(t-t',x-x')-\boldsymbol{\rho}^T(t'-t,x'-x) \end{bmatrix} \end{aligned} \tag{24}$$

where

$$\begin{aligned}\mathcal{S}^{\mathrm{e}}(t-t',x-x') &= \begin{bmatrix}\mathbf{C}^{\mathrm{e}}(t-t',x-x') & \mathbf{B}^{\mathrm{e}}(t-t',x-x')\\ \mathbf{D}^{\mathrm{e}}(t-t',x-x') & \boldsymbol{\rho}^{\mathrm{e}}(t-t',x-x')\end{bmatrix}\\ \mathcal{S}^{\mathrm{o}}(t-t',x-x') &= \begin{bmatrix}\mathbf{C}^{\mathrm{o}}(t-t',x-x') & \mathbf{B}^{\mathrm{o}}(t-t',x-x')\\ \mathbf{D}^{\mathrm{o}}(t-t',x-x') & \boldsymbol{\rho}^{\mathrm{o}}(t-t',x-x')\end{bmatrix}\end{aligned} \tag{25}$$

For spatially and frequency dispersive media, the generalized force vector $\boldsymbol{\Sigma}(t,x)$ depends nonlocally on the strain field $\mathbf{E}(t',x')$ and may involve memory effects due to dispersion.

The instantaneous power density at $\mathbf{r}$ is:

$$P(t,x) = \boldsymbol{\sigma}^T(t,x)\frac{\partial \boldsymbol{\varepsilon}(t,x)}{\partial t} + \mathbf{p}^T(t,x)\frac{\partial \mathbf{v}(t,x)}{\partial t}. \tag{26}$$

The total work over the length L is:

$$W(t) = \int_x \left[\boldsymbol{\sigma}^T(t,x)\frac{\partial \boldsymbol{\varepsilon}(t,x)}{\partial t} + \mathbf{p}^T(t,x)\frac{\partial \mathbf{v}(t,x)}{\partial t}\right] dx. \tag{27}$$

The net work done over a complete cycle T is:

$$W_{\mathrm{cycle}} = \int_0^T W(t)dt = \int_0^T \int_x \left[\boldsymbol{\sigma}^T(t,x)\frac{\partial \boldsymbol{\varepsilon}(t,x)}{\partial t} + \mathbf{p}^T(t,x)\frac{\partial \mathbf{v}(t,x)}{\partial t}\right] dxdt. \tag{28}$$

Substitute the constitutive relationship:

$$\begin{aligned}\boldsymbol{\varepsilon}(t,x) &= \int_x\int_{-\infty}^t \mathbf{C}(t-t',x-x')\boldsymbol{\sigma}(t',x')dt'dx' + \int_x\int_{-\infty}^t \mathbf{B}(t-t',x-x')\mathbf{v}(t',x')dt'dx'.\\ \mathbf{p}^T(t,x) &= \int_x\int_{-\infty}^t \boldsymbol{\sigma}^T(t',x')\mathbf{D}^T(t-t',x-x')dt'dx' + \int_x\int_{-\infty}^t \mathbf{v}^T(t',x')\boldsymbol{\rho}^T(t-t',x-x')dt'dx'.\end{aligned} \tag{29}$$

Thus:

$$W_{\mathrm{cycle}} = W^C_{\mathrm{cycle}} + W^B_{\mathrm{cycle}} + W^D_{\mathrm{cycle}} + W^\sigma_{\mathrm{cycle}} \tag{30}$$

where

$$\begin{aligned}W^C_{\mathrm{cycle}} &= \int_0^T\int_x\int_x\int_{-\infty}^t \boldsymbol{\sigma}^T(t,x)\frac{\partial \mathbf{C}(t-t',x-x')}{\partial t}\boldsymbol{\sigma}(t',x')dt'dx'dxdt\\ W^B_{\mathrm{cycle}} &= \int_0^T\int_x\int_x\int_{-\infty}^t \boldsymbol{\sigma}^T(t,x)\frac{\partial \mathbf{B}(t-t',x-x')}{\partial t}\mathbf{v}(t',x')dt'dx'dxdt\\ W^D_{\mathrm{cycle}} &= \int_0^T\int_x\int_x\int_{-\infty}^t \boldsymbol{\sigma}^T(t',x')\mathbf{D}^T(t-t',x-x')\frac{\partial \mathbf{v}(t,x)}{\partial t}dt'dx'dxdt\\ W^\sigma_{\mathrm{cycle}} &= \int_0^T\int_x\int_x\int_{-\infty}^t \mathbf{v}^T(t',x')\frac{\partial \boldsymbol{\rho}(t-t',x-x')}{\partial t}\mathbf{v}(t',x')dt'dx'dxdt\end{aligned} \tag{31}$$

Now we integrate by parts in t, treating $\partial \boldsymbol{\mathcal{E}}_1(t,x)/\partial t$ as the derivative term, and we have:

$$
\begin{aligned}
W^C_{\text{cycle}} &= \int_0^T \int_x \int_x \int_{-\infty}^t \boldsymbol{\sigma}^T(t,x) \frac{\partial \mathbf{C}(t-t', x-x')}{\partial (t-t')} \boldsymbol{\sigma}(t',x') dt' dx' dx dt \\
&= \frac{1}{2} \int_0^T \int_x \int_x \int_{-\infty}^t \boldsymbol{\sigma}^T(t,x) \frac{\partial \mathbf{C}(t-t', x-x')}{\partial (t-t')} \boldsymbol{\sigma}(t',x') + \boldsymbol{\sigma}^T(t',x') \frac{\partial \mathbf{C}(t'-t, x'-x)}{\partial (t'-t)} \boldsymbol{\sigma}(t,x) dt' dx' dx dt \\
&= \frac{1}{2} \int_0^T \int_x \int_x \int_{-\infty}^t \boldsymbol{\sigma}^T(t,x) \left[\frac{\partial \left(\mathbf{C}(t-t', x-x') - \mathbf{C}^T(t'-t, x'-x) \right)}{\partial (t-t')} \right] \boldsymbol{\sigma}(t',x') dt' dx' dx dt \\
&= \frac{1}{2} \int_0^T \int_x \int_x \int_{-\infty}^t \boldsymbol{\sigma}^T(t,x) \frac{\partial \mathbf{C}^{\text{o}}(t'-t, x'-x)}{\partial (t-t')} \boldsymbol{\sigma}(t',x') dt' dx' dx dt
\end{aligned}
\tag{32}
$$

For a cyclic process, $\boldsymbol{\mathcal{E}}_1(t,x)$ returns to its initial state after one cycle, so the first term on the right-hand side vanishes. If $\mathbf{C}^{\text{odd}}(t'-t, x'-x)$ is not equal to 0, then there is always some cyclic deformation such that $W^C_{\text{cycle}} \neq 0$. Similarly, if $\boldsymbol{\sigma}^{\text{odd}}(t'-t, x'-x)$ is not equal to 0, then there is always some cyclic deformation such that $W^{\sigma}_{\text{cycle}} \neq 0$.

Now we integrate by parts in t, treating $\partial \boldsymbol{\mathcal{E}}_2(t,x)/\partial t$ as the derivative term in W^D_{cycle}, and we have:

$$
\begin{aligned}
W^D_{\text{cycle}} = & \left[\int_x \int_x \int_{-\infty}^t \boldsymbol{\sigma}^T(t',x') \mathbf{D}^T(t-t', x-x') \mathbf{v}(t,x) dt' dx' dx \right]_0^T \\
& - \int_0^T \int_x \int_x \int_{-\infty}^t \boldsymbol{\sigma}^T(t',x') \frac{\partial \mathbf{D}^T(t-t', x-x')}{\partial t} \mathbf{v}(t,x) dt' dx' dx dt
\end{aligned}
\tag{33}
$$

$$
\begin{aligned}
& W^B_{\text{cycle}} + W^D_{\text{cycle}} \\
&= \int_0^T \int_x \int_x \int_{-\infty}^t \boldsymbol{\sigma}^T(t,x) \frac{\partial \mathbf{B}(t-t', x-x')}{\partial (t-t')} \mathbf{v}(t',x') - \boldsymbol{\sigma}^T(t',x') \frac{\partial \mathbf{D}^T(t-t', x-x')}{\partial (t-t')} \mathbf{v}(t,x) dt' dx' dx dt \\
&= \int_0^T \int_x \int_x \int_{-\infty}^t \boldsymbol{\sigma}^T(t,x) \frac{\partial \left(\mathbf{B}(t-t', x-x') + \mathbf{D}^T(t-t', x-x') \right)}{\partial (t-t')} \mathbf{v}(t',x') dt' dx' dx dt \\
&= \int_0^T \int_x \int_x \int_{-\infty}^t \boldsymbol{\mathcal{E}}_2^T(t',x') \mathbf{B}^{\text{odd}}(t-t', x-x') \boldsymbol{\mathcal{E}}_1(t,x) dt' dx' dx dt
\end{aligned}
\tag{34}
$$

If $\mathbf{B}^{\text{odd}}(t'-t, x'-x)$ is not equal to 0, then there is always some cyclic deformation such that $W^C_{\text{cycle}} \neq 0$. Finally, we find that the odd constitutive matrix induces the nonzero cyclic work and breaks the major symmetry of the constitutive matrix.

In the reciprocal space, the even and odd constitutive matrices can be obtained from Fourier's transform and they are given as

$$
\begin{aligned}
\begin{bmatrix} \mathbf{C}^{\text{e}}(\omega,k) & \mathbf{B}^{\text{e}}(\omega,k) \\ \mathbf{D}^{\text{e}}(\omega,k) & \boldsymbol{\rho}^{\text{e}}(\omega,k) \end{bmatrix} &= \frac{1}{2} \begin{bmatrix} \mathbf{C}(\omega,k) + \mathbf{C}^T(-\omega,-k) & \mathbf{B}(\omega,k) - \mathbf{D}^T(-\omega,-k) \\ \mathbf{D}(\omega,k) - \mathbf{B}^T(-\omega,-k) & \boldsymbol{\rho}(\omega,k) + \boldsymbol{\rho}^T(-\omega,-k) \end{bmatrix} \\
\begin{bmatrix} \mathbf{C}^{\text{o}}(\omega,k) & \mathbf{B}^{\text{o}}(\omega,k) \\ \mathbf{D}^{\text{o}}(\omega,k) & \boldsymbol{\rho}^{\text{o}}(\omega,k) \end{bmatrix} &= \frac{1}{2} \begin{bmatrix} \mathbf{C}(\omega,k) - \mathbf{C}^T(-\omega,-k) & \mathbf{B}(\omega,k) + \mathbf{D}^T(-\omega,-k) \\ \mathbf{D}(\omega,k) + \mathbf{B}^T(-\omega,-k) & \boldsymbol{\rho}(\omega,k) - \boldsymbol{\rho}^T(-\omega,-k) \end{bmatrix}
\end{aligned}
\tag{35}
$$

If odd couplings do not exist, the odd constitutive matrix vanishes

$$
\mathbf{C}(\omega,k) = \mathbf{C}^T(-\omega,-k),\ \mathbf{B}(\omega,k) = \mathbf{D}^T(-\omega,-k),\ \boldsymbol{\rho}(\omega,k) = \boldsymbol{\rho}^T(-\omega,-k),
\tag{36}
$$

Using Eq. (??), we have

$$\mathbf{C}(\omega,k)=\mathbf{C}^{\dagger}(\omega,k),\quad \mathbf{B}(\omega,k)=-\mathbf{D}^{\dagger}(\omega,k),\quad \boldsymbol{\rho}(\omega,k)=\boldsymbol{\rho}^{\dagger}(\omega,k), \tag{37}$$

which is consistent with the symmetry condition from the microscopic analysis in Eq. (??).

1.4. Broken Maxwell–Betti reciprocity

In the media without frequency dispersion and spatial dispersion, the Maxwell–Betti reciprocity is equivalent to the zero cyclic work. However, with frequency dispersion and spatial dispersion, the Maxwell–Betti reciprocity is not equivalent to the zero cyclic work. Here we derive the equivalent condition for Maxwell–Betti reciprocity. And then introduce how to break Maxwell–Betti reciprocity using our sensor-actuator system.

Next, we prove that the asymmetric constitutive relation implies the breakdown of Maxwell-Betti reciprocity.

In the frequency domain, the governing equations in Eq. (??) can be rewritten as

$$\begin{bmatrix} 0 & 0 & 0 & -\partial_x \\ 0 & 0 & -\partial_x & 1 \\ 0 & \partial_x & 0 & 0 \\ \partial_x & 1 & 0 & 0 \end{bmatrix} \begin{bmatrix} \boldsymbol{\sigma}(\omega,x) \\ \mathbf{w}(\omega,x) \end{bmatrix} + \int_{-\infty}^{\infty} \begin{bmatrix} \mathbf{C}(\omega,x-x') & -i\omega\mathbf{B}(\omega,x-x') \\ -i\omega\mathbf{D}(\omega,x-x') & -\omega^2\boldsymbol{\rho}(\omega,x-x') \end{bmatrix} \begin{bmatrix} \boldsymbol{\sigma}(\omega,x-x') \\ \mathbf{w}(\omega,x-x') \end{bmatrix} dx' = \mathbf{Q}, \tag{38}$$

The Maxwell–Betti reciprocity theorem states that for a linear elastic system, the work done by one set of forces acting through the displacements caused by a second set of forces is equal to the work done by the second set of forces acting through the displacements caused by the first set. Mathematically:

$$\int_L \mathbf{u}_2^T(\omega,x)\mathbf{Q}_1(\omega,x)\,dx = \int_L \mathbf{u}_1^T(\omega,x)\mathbf{Q}_2(\omega,x)\,dx, \tag{39}$$

where: $\mathbf{Q}_1$ and $\mathbf{Q}_2$ are two different distributions of body forces. $\mathbf{u}_1$ and $\mathbf{u}_2$ are the corresponding displacement fields caused by $\mathbf{Q}_1$ and $\mathbf{Q}_2$, respectively. L is the length of the metabeam. The left hand side is

$$\begin{aligned} &\mathbf{u}_2^T(\omega,x)\mathbf{Q}_1(\omega,x) \\ &= -\partial_x\left(F_2(\omega,x)w_1(\omega,x)\right) - \partial_x\left(M_2(\omega,x)\psi_1(\omega,x)\right) + \partial_x F_2(\omega,x)w_1(\omega,x) + \partial_x M_2(\omega,x)\psi_1(\omega,x) \\ &+ w_2(\omega,x)\partial_x F_1(\omega,x) + \psi_2(\omega,x)\partial_x M_1(\omega,x) + F_2(\omega,x)\psi_1(\omega,x) + F_1(\omega,x)\psi_2(\omega,x) \\ &+ \int_{-\infty}^{\infty} \begin{bmatrix} \boldsymbol{\sigma}_2(\omega,x) & \mathbf{w}_2(\omega,x) \end{bmatrix} \begin{bmatrix} \mathbf{C}(\omega,x-x') & -i\omega\mathbf{B}(\omega,x-x') \\ -i\omega\mathbf{D}(\omega,x-x') & -\omega^2\boldsymbol{\rho}(\omega,x-x') \end{bmatrix} \begin{bmatrix} \boldsymbol{\sigma}_1(\omega,x') \\ \mathbf{w}_1(\omega,x') \end{bmatrix} dx' \end{aligned} \tag{40}$$

while

$$\begin{aligned} &\mathbf{u}_1^T(\omega,x)\mathbf{Q}_2(\omega,x) \\ &= -\partial_x\left(F_1(\omega,x)w_2(\omega,x)\right) - \partial_x\left(M_1(\omega,x)\psi_2(\omega,x)\right) + \partial_x F_1(\omega,x)w_2(\omega,x) + \partial_x M_1(\omega,x)\psi_2(\omega,x) \\ &+ w_1(\omega,x)\partial_x F_2(\omega,x) + \psi_1(\omega,x)\partial_x M_2(\omega,x) + F_1(\omega,x)\psi_2(\omega,x) + F_2(\omega,x)\psi_1(\omega,x) \\ &+ \int_{-\infty}^{\infty} \begin{bmatrix} \boldsymbol{\sigma}_1(\omega,x) & \mathbf{w}_1(\omega,x) \end{bmatrix} \begin{bmatrix} \mathbf{C}(\omega,x-x') & -i\omega\mathbf{B}(\omega,x-x') \\ -i\omega\mathbf{D}(\omega,x-x') & -\omega^2\boldsymbol{\rho}(\omega,x-x') \end{bmatrix} \begin{bmatrix} \boldsymbol{\sigma}_2(\omega,x') \\ \mathbf{w}_2(\omega,x') \end{bmatrix} dx' \end{aligned} \tag{41}$$

For the reciprocal media, we have

$$\mathbf{C}(\omega, k) = \mathbf{C}^T(\omega, -k), \quad \mathbf{B}(\omega, k) = \mathbf{D}^T(\omega, -k), \quad \boldsymbol{\rho}(\omega, k) = \boldsymbol{\rho}^T(\omega, -k). \tag{42}$$

For nonlocal elasticity, $\mathbf{u}_i(\mathbf{r})$ at a point $\mathbf{r}$ depends not just on $\mathbf{u}_i(\mathbf{r})$ at the same point, but also on forces at all other points $\mathbf{r}'$, via a nonlocal elastic tensor kernel.

This generalization means that stress at $\mathbf{r}$ is influenced by strains over the entire body, mediated by the kernel $C_{ijkl}(\mathbf{r}, \mathbf{r}')$. 3. Symmetry from Maxwell–Betti Reciprocity

To derive the symmetry condition for $C_{ijkl}(\mathbf{r}, \mathbf{r}')$, we use the Maxwell–Betti reciprocity theorem applied to work contributions:

The Maxwell–Betti reciprocity theorem can be derived from major symmetry and time-reversal symmetry Altman and Suchy (2011).

1.5. Causality and Kramers–Kronig relations

Here we merely refer to the principle of causality owing to which the induction at the instant I is determined only by the present field and the field at previous times $t' \leq t$

The constitutive relation in reciprocal space depends on both frequency and wavenumber, indicating nonlocality in both spatial and temporal domains.

$$\mathbf{\mathcal{S}}(x, t) = \begin{cases} \mathbf{\mathcal{S}}(x, t), & \text{if } |x| < ct, \\ 0, & \text{otherwise }, \end{cases} \tag{43}$$

In the space-time domain, the nonlocal constitutive relations for spatially and temporally homogeneous media can be written as (Leontovich, 1961; Sun and Puri, 1989; Shokri and Rukhadze, 2019)

$$\mathbf{\mathcal{E}}(t, x) = \int_0^t dt' \int_{-ct'}^{ct'} dx' \mathbf{\mathcal{S}}(x - x', t - t') \mathbf{\Sigma}(t', x'), \tag{44}$$

where c represents the maximum group velocity of a Timoshenko beam. The group velocity of a Timoshenko beam converges to $c = 1$ as $k \to \infty$; therefore, the maximum group velocity can be considered $c = 1$. The limits of integration for τ are restricted to $[0, \infty)$, and for ξ, they range from $-c\tau$ to $c\tau$, as dictated by the causality condition. This condition ensures that the response signal at x occurs only after the time required for the signal, excited at $x - \xi$, to travel the distance to x. Considering the plane wave propagation in the media, the above equation can be written as

$$\mathbf{\mathcal{E}}(k, \omega) = \mathbf{\mathcal{S}}(k, \omega) \mathbf{\Sigma}(k, \omega) \tag{45}$$

where

$$\mathbf{\mathcal{S}}(\omega, k) = \int_0^\infty e^{i\omega t} \mathrm{d}t \int_{-ct}^{ct} \mathbf{\mathcal{S}}(x, t) e^{ikx} \mathrm{d}x. \tag{46}$$

and

$$\mathbf{\mathcal{S}}(t, x) = \int_{-\infty}^\infty \int_{-\infty}^\infty \mathbf{\mathcal{S}}(\omega, k) e^{-ikx - i\omega t} \mathrm{d}\omega \mathrm{d}k. \tag{47}$$

Therefore, we have

$$\begin{aligned}
\boldsymbol{\mathcal{S}}(\omega,k) &= \frac{1}{4\pi^2}\int_0^\infty e^{i\omega t}\mathrm{d}t\int_{-ct}^{ct}\int_{-\infty}^{\infty}\int_{-\infty}^{\infty}\boldsymbol{\mathcal{S}}\left(\omega',k'\right)e^{-i\omega' t-ik'x+ikx}\mathrm{d}\omega'\mathrm{d}k'\mathrm{d}x \\
&= \frac{1}{4\pi^2}\int_{-\infty}^{\infty}\int_{-\infty}^{\infty}\boldsymbol{\mathcal{S}}\left(\omega',k'\right)\mathrm{d}\omega'\mathrm{d}k'\int_0^\infty e^{i\left(\omega-\omega'\right)t}\mathrm{d}t\int_{-ct}^{ct}e^{i\left(k-k'\right)x}\mathrm{d}x \\
&= \frac{1}{4\pi^2}\int_{-\infty}^{\infty}\int_{-\infty}^{\infty}\boldsymbol{\mathcal{S}}\left(\omega',k'\right)\mathrm{d}\omega'\mathrm{d}k'\int_0^\infty \frac{1}{i\left(k-k'\right)}\left[e^{i\left(\omega-\omega'+ck-ck'\right)t}-e^{i\left(\omega-\omega'-ck'-ck\right)t}\right]\mathrm{d}t
\end{aligned} \tag{48}$$

We add a small imaginary part $i\delta$, where $\delta>0$, in order for the integration to converge over time:

$$\begin{aligned}
\boldsymbol{\mathcal{S}}(\omega,k) &= \frac{1}{4\pi^2}\int_{-\infty}^{\infty}\int_{-\infty}^{\infty}\frac{\boldsymbol{\mathcal{S}}\left(\omega',k'\right)}{i\left(k-k'\right)}\left(\frac{-1}{i\left(\omega-\omega'+c(k-k')+i\delta\right)}+\frac{1}{i\left(\omega-\omega'+c(k'-k)+i\delta\right)}\right)\mathrm{d}\omega'\mathrm{d}k' \\
&= \frac{1}{4\pi^2}\int_{-\infty}^{\infty}\int_{-\infty}^{\infty}\frac{-2\boldsymbol{\mathcal{S}}\left(\omega',k'\right)\mathrm{d}\omega'\mathrm{d}k'}{\left(\omega-\omega'+c(k'-k)+i\delta\right)\left(\omega-\omega'+c(k-k')+i\delta\right)} \\
&= -\frac{1}{2\pi^2}\int_{-\infty}^{\infty}\int_{-\infty}^{\infty}\frac{\boldsymbol{\mathcal{S}}\left(\omega',k'\right)}{\left(\omega-\omega'+c(k'-k)+i\delta\right)\left(\omega-\omega'+c(k-k')+i\delta\right)}\mathrm{d}\omega'\mathrm{d}k'
\end{aligned} \tag{49}$$

Considering that $\sigma(\omega,k)$ is analytic in the upper half of the ω-plane for a fixed k, the result of the integration should be of the form

$$\boldsymbol{\mathcal{S}}(\omega,k) = \frac{1}{2\pi i}\int_{-\infty}^{\infty}\frac{\boldsymbol{\mathcal{S}}\left(\omega',k+(\omega'-\omega)/c\right)}{\left(\omega'-\omega-i\delta\right)}\mathrm{d}\omega' \tag{50}$$

Using Plemelj formula, the wavenumber-dependent Kramers-Kronig relations are

$$\begin{aligned}
\mathrm{Re}[\boldsymbol{\mathcal{S}}(\omega,k)] &= \frac{1}{\pi}\mathcal{P}\int_{-\infty}^{\infty}\frac{\mathrm{Im}\left[\boldsymbol{\mathcal{S}}\left(\omega',k+(\omega'-\omega)/c\right)\right]}{\omega'-\omega}d\omega' \\
\mathrm{Im}[\boldsymbol{\mathcal{S}}(\omega,k)] &= -\frac{1}{\pi}\mathcal{P}\int_{-\infty}^{\infty}\frac{\mathrm{Re}\left[\boldsymbol{\mathcal{S}}\left(\omega',k+(\omega'-\omega)/c\right)\right]}{\omega'-\omega}d\omega'
\end{aligned} \tag{51}$$

If signal propagating velocity $c\to\infty$, the Kramers-Kronig relations are reduced into

$$\begin{aligned}
\mathrm{Re}[\boldsymbol{\mathcal{S}}(\omega,k)] &= \frac{1}{\pi}\mathcal{P}\int_{-\infty}^{\infty}\frac{\mathrm{Im}\left[\boldsymbol{\mathcal{S}}\left(\omega',k\right)\right]}{\omega'-\omega}d\omega' \\
\mathrm{Im}[\boldsymbol{\mathcal{S}}(\omega,k)] &= -\frac{1}{\pi}\mathcal{P}\int_{-\infty}^{\infty}\frac{\mathrm{Re}\left[\boldsymbol{\mathcal{S}}\left(\omega',k\right)\right]}{\omega'-\omega}d\omega'
\end{aligned} \tag{52}$$

References

Altman, C. and Suchy, K. (2011). *Reciprocity, spatial mapping and time reversal in electromagnetics*. Springer Science & Business Media.

Leontovich, M. (1961). Generalization of the kramers-kronig formulas to media with spatial dispersion. *SOVIET PHYSICS JETP-USSR*, 13(3):634–637.

Li, Z., Han, P., and Hu, G. (2024). Willis dynamic homogenization method for acoustic metamaterials based on multiple scattering theory. *Journal of the Mechanics and Physics of Solids*, 189:105692.

Li, Z., Qu, H., Zhang, H., Liu, X., and Hu, G. (2022). Interfacial wave between acoustic media with willis coupling. *Wave Motion*, 112:102922.

Liu, Y., Liang, Z., Zhu, J., Xia, L., Mondain-Monval, O., Brunet, T., Alù, A., and Li, J. (2019). Willis metamaterial on a structured beam. *Physical Review X*, 9(1):011040.

Pernas-Salomón, R. and Shmuel, G. (2020a). Fundamental principles for generalized willis metamaterials. *Physical Review Applied*, 14(6):064005.

Pernas-Salomón, R. and Shmuel, G. (2020b). Symmetry breaking creates electro-momentum coupling in piezoelectric metamaterials. *Journal of the Mechanics and Physics of Solids*, 134:103770.

Qu, H., Liu, X., and Hu, G. (2022). Mass-spring model of elastic media with customizable willis coupling. *International Journal of Mechanical Sciences*, 224:107325.

Shokri, B. and Rukhadze, A. A. (2019). *Electrodynamics of Conducting Dispersive Media*. Springer.

Sun, J. G. and Puri, A. (1989). Kramers-kronig relations in media with spatial dispersion. *Optics communications*, 70(1):33–37.